



The SOFIA Massive (SOMA) Star Formation Survey. IV. Isolated Protostars

Downloaded from: <https://research.chalmers.se>, 2025-12-05 00:12 UTC

Citation for the original published paper (version of record):

Fedriani, R., Tan, J., Telkamp, Z. et al (2023). The SOFIA Massive (SOMA) Star Formation Survey. IV. Isolated Protostars. *Astrophysical Journal*, 942(1). <http://dx.doi.org/10.3847/1538-4357/aca4cf>

N.B. When citing this work, cite the original published paper.



The SOFIA Massive (SOMA) Star Formation Survey. IV. Isolated Protostars

Rubén Fedriani¹, Jonathan C. Tan^{1,2}, Zoie Telkamp², Yichen Zhang^{2,3}, Yao-Lun Yang^{2,3}, Mengyao Liu², James M. De Buizer⁴, Chi-Yan Law¹, Maria T. Beltrán⁵, Viviana Rosero⁶, Kei E. I. Tanaka^{7,8}, Giuliana Cosentino¹, Prasanta Gorai¹, Juan Farias¹, Jan E. Staff⁹, and Barbara Whitney¹⁰

¹ Department of Space, Earth & Environment, Chalmers University of Technology, SE-412 93 Gothenburg, Sweden; ruben.fedriani@chalmers.se

² Department of Astronomy, University of Virginia, Charlottesville, Virginia 22904, USA

³ RIKEN Cluster for Pioneering Research, Wako-shi, Saitama, 351-0198, Japan

⁴ SOFIA-USRA, NASA Ames Research Center, MS 232-12, Moffett Field, CA 94035, USA

⁵ INAF-Osservatorio Astrofisico di Arcetri, Largo E. Fermi 5, I-50125 Firenze, Italy

⁶ National Radio Astronomy Observatory, 1003 Lópezville Road, Socorro, NM 87801, USA

⁷ Center for Astrophysics and Space Astronomy, University of Colorado Boulder, Boulder, CO 80309, USA

⁸ National Astronomical Observatory of Japan, National Institutes of Natural Sciences, 2-21-1 Osawa, Mitaka, Tokyo 181-8588, Japan

⁹ College of Science and Math University of the Virgin Islands St Thomas, VI 00802 USA

¹⁰ Space Science Institute, 4765 Walnut Street, Suite B, Boulder, CO 80301, USA

Received 2022 May 18; revised 2022 November 4; accepted 2022 November 7; published 2022 December 28

Abstract

We present $\sim 10\text{--}40\ \mu\text{m}$ SOFIA-FORCAST images of 11 *isolated* protostars as part of the SOFIA Massive (SOMA) Star Formation Survey, with this morphological classification based on $37\ \mu\text{m}$ imaging. We develop an automated method to define source aperture size using the gradient of its background-subtracted enclosed flux and apply this to build spectral energy distributions (SEDs). We fit the SEDs with radiative transfer models, developed within the framework of turbulent core accretion (TCA) theory, to estimate key protostellar properties. Here, we release the *sedcreator* python package that carries out these methods. The SEDs are generally well fitted by the TCA models, from which we infer initial core masses M_c ranging from $20\text{--}430\ M_\odot$, clump mass surface densities $\Sigma_{cl} \sim 0.3\text{--}1.7\ \text{g cm}^{-2}$, and current protostellar masses $m_* \sim 3\text{--}50\ M_\odot$. From a uniform analysis of the 40 sources in the full SOMA survey to date, we find that massive protostars form across a wide range of clump mass surface density environments, placing constraints on theories that predict a minimum threshold Σ_{cl} for massive star formation. However, the upper end of the $m_*\text{--}\Sigma_{cl}$ distribution follows trends predicted by models of internal protostellar feedback that find greater star formation efficiency in higher Σ_{cl} conditions. We also investigate protostellar far-IR variability by comparison with IRAS data, finding no significant variation over an ~ 40 yr baseline.

Unified Astronomy Thesaurus concepts: Massive stars (732); Star formation (1569); Interstellar medium (847); Jets (870); Infrared sources (793); Protostars (1302); Spectral energy distribution (2129)

Supporting material: data behind figures, machine-readable tables

1. Introduction

Massive stars are the engines that drive the evolution of galaxies. Their energetic radiation, winds, and supernovae also impact their surrounding environments, including protoplanetary disks around lower-mass stars that are forming in the same protocluster. In spite of their importance, many fundamental questions remain unanswered about the origins of massive stars, including the basic nature of their formation mechanism, e.g., whether it is via an extension of standard core accretion theory (e.g., McKee & Tan 2003) or whether it requires chaotic, competitive accretion in the center of a dense protocluster of low-mass protostars (e.g., Bonnell et al. 1998; Wang et al. 2010; Grudić et al. 2022).

The SOFIA Massive (SOMA) Star Formation Survey (PI: Tan) aims to characterize a sample of $\gtrsim 50$ high- and intermediate-mass protostars over a range of evolutionary stages and environments with their $\sim 10\text{--}40\ \mu\text{m}$ emission observed with the SOFIA-Faint Object infraRed CAmera for the SOFIA Telescope (FORCAST) instrument (Herter et al. 2018). In

Paper I of the survey (De Buizer et al. 2017), the first eight sources were presented, which were mostly massive protostars. In Paper II (Liu et al. 2019b), seven additional high-luminous sources were presented, corresponding to some of the most massive protostars in the survey. In Paper III (Liu et al. 2020), 14 intermediate-mass sources were presented and analyzed. Here, in Paper IV in the series, we present 10 regions that harbor a total of 11 sources, selected based on the nature of their environment, i.e., appearing to be relatively *isolated* in $37\ \mu\text{m}$ imaging. We note that another set of eight regions that are relatively crowded in their $37\ \mu\text{m}$ morphology, i.e., *clustered* sources, will be presented in Paper V in this series (Z. Telkamp et al. 2022, in preparation). Thus, we consider these samples will help to probe the environmental dependence of star formation, e.g., being of particular interest for testing the prediction of competitive accretion models that massive protostars should be surrounded by clusters of lower-mass protostars.

Our approach follows the same general methods developed in Papers I–III to build the spectral energy distributions (SEDs) of the protostars, measuring fluxes from infrared (IR) images, especially from the Spitzer, SOFIA, and Herschel facilities. We then fit these SEDs with the Zhang & Tan (2018, hereafter ZT18) protostellar radiative transfer (RT) models to estimate



Original content from this work may be used under the terms of the [Creative Commons Attribution 4.0 licence](https://creativecommons.org/licenses/by/4.0/). Any further distribution of this work must maintain attribution to the author(s) and the title of the work, journal citation and DOI.

Table 1
SOFIA-FORCAST Observations: Observation Dates and Exposure Times (seconds)

Source	R.A. (J2000)	Decl. (J2000)	d (kpc)	Obs. Date	7.7 μm	19.7 μm	31.5 μm	37.1 μm
AFGL 2591	20 ^h 29 ^m 24 ^s .8916	+40°11'19" 388	3.3	2016 Sep 20	404	779	642	1504
G25.40-0.14	18 ^h 38 ^m 08 ^s .2700	−06°45'57" 820	5.7	2015 Jun 5	278	701	482	743
G30.59-0.04	18 ^h 47 ^m 18 ^s .9000	−02°06'17" 600	11.8	2018 Sep 8	492	1319	825	2020
G32.03+0.05	18 ^h 49 ^m 37 ^s .0520	−00°46'50" 150	5.5	2015 Nov 4	281	899	818	281
G33.92+0.11	18 ^h 52 ^m 50 ^s .2730	+00°55'29" 594	7.1	2015 Nov 20	116	308	162	630
G40.62-0.14	19 ^h 06 ^m 01 ^s .6000	+06°46'36" 200	2.2	2015 Jun 3	337	664	386	466
IRAS 00259+5625	00 ^h 28 ^m 42 ^s .6000	+56°42'01" 110	2.5	2015 Nov 20	116	308	162	630
IRAS 00420+5530	00 ^h 44 ^m 58 ^s .5842	+55°46'45" 675	2.2	2015 Jun 3	337	664	386	466
IRAS 23385+6053	23 ^h 40 ^m 54 ^s .5171	+61°10'27" 768	4.9	2015 Jun 3	337	664	386	466
HH 288	00 ^h 37 ^m 13 ^s .2580	+64°04'15" 020	2.0	2015 Nov 6	334	806	488	1512

Note. The source positions listed here are the same as the positions of the black crosses denoting the radio continuum peak for each of the sources shown in Figures 2–11. Source distances are from the literature are discussed below (see Section 4.1).

intrinsic source properties. However, here we introduce a number of new improvements to the SOMA analysis methodology, including an algorithmic way of choosing the aperture size and a new python module that updates the SED-fitting tool, including a revised method of assessing uncertainties in background-subtracted fluxes. We measure fluxes and fit SEDs for all the SOMA Papers I–IV sources with the new methods to produce a sample of 40 massive protostars that have been analyzed in a uniform way. We are thus able to more reliably examine trends in source properties among these sources.

Similar studies based on the SED fitting with the ZT18 models have been carried out by Towner et al. (2019) on 12 extended green objects (Lim & De Buizer 2019) on 41 massive protostar candidates in W51A (Moser et al. 2020) on about 30 sources in the Infrared Dark Cloud (IRDC) G28.37+00.07. Furthermore, the methods developed here have also been applied by Costa Silva et al. (2022) in IRAS 18264-1152, Law et al. (2022) in G28.20-0.05, and Taniguchi et al. (2022) in G24.78+0.08.

The relatively isolated nature of the sources of this paper also enables a search for mid-IR (MIR) to far-IR (FIR) variability by comparing our SOFIA and Herschel-fitted SEDs with the flux measurements of IRAS made ~ 40 yr earlier. Variability at MIR to FIR wavelengths has been reported in a few massive protostars (e.g., Caratti o Garatti et al. 2017; Hunter et al. 2017; Chen et al. 2021; Stecklum et al. 2021) and interpreted as being caused by accretion bursts. However, it is very uncertain what fraction of massive protostars undergo such bursts and what fraction of mass is accreted in such events.

The observations and data utilized in this paper are described in Section 2. The analysis methods are summarized in Section 3. We present the MIR to FIR imaging and SED-fitting results in Section 4. We discuss our results in Section 5 and give a summary in Section 6.

2. Observations

We used the Stratospheric Observatory for Infrared Astronomy (SOFIA¹¹) together with FORCAST (Herter et al. 2018) instrument to observe 10 regions of massive star formation that harbor 11 protostars. Four filters were used that are centered at 7.7, 19.7, 31.5, and 37.1 μm (see Table 1 for details). Source selection for the SOMA survey mainly utilized the CORNISH

survey (Hoare et al. 2012), complemented by radio-quiet MIR sources in IRDCs (Butler & Tan 2012).

The photometric and astrometric calibration methods are the same as those used in Papers I–III. For SOFIA observations the photometric calibration error is estimated to be in the range of $\sim 3\%$ – 7% . The astrometric precision is about $0''.1$ for the SOFIA 7.7 μm image, and $0''.4$ for longer wavelength in SOFIA images. See Paper I for further details. Pipeline-reduced and calibrated data from the SOFIA archive were used.

In addition to SOFIA observations, when available, we also retrieved publicly available images of Spitzer/IRAC (Fazio et al. 2004; Werner et al. 2004) at 3.6, 4.5, 5.8, and 8.0 μm from the Spitzer Heritage Archive and Herschel/PACS and SPIRE (Griffin et al. 2010) at 70, 160, 250, 350, and 500 μm from the ESA Herschel Science Archive, and IRAS (Neugebauer et al. 1984) at 12, 25, 60, and 100 μm from the NASA/IPAC Infrared Science Archive. We use the HIRES results of the IRAS data to achieve a resolution of $\sim 1'$. The astrometric precision is about $20''$ – $30''$. Flux measured from HIRES agrees with those of the IRAS Point Source Catalog (PSC2) to within 20% and a ring of low flux that may appear around a point source can contain up to another 10% uncertainty of the flux of the point source.

3. Methods

In this paper, we introduce a number of new and updated analysis methods. The main update is the release of `sedcreator`, which is an open-source python package hosted in both GitHub¹² and PyPi¹³ (the documentation can be accessed at this URL <https://sedcreator.readthedocs.io/>). The main two sets of tools of `sedcreator` are encapsulated into `SedFluxer` and `SedFitter`. `SedFluxer` helps one construct an SED by providing tools to measure fluxes on a given image. `SedFitter` fits an SED with massive star formation radiation transfer model grid by ZT18. It updates and replaces the earlier version of the fitting tool written in IDL (Zhang 2018).

3.1. SedFluxer

We follow methods similar to those of Papers I–III to construct SEDs. In brief, this involves defining an aperture for each source that is based on consideration of the Herschel 70 μm or SOFIA 37 μm (when Herschel 70 μm is not available) images

¹¹ SOFIA is jointly operated by the Universities Space Research Association, Inc. (USRA), under NASA contract NAS2-97001, and the Deutsches SOFIA Institute under DLR contract 50 OK 0901 to the University of Stuttgart.

¹² <https://github.com/fedriani/sedcreator>

¹³ <https://pypi.org/project/sedcreator/>

with the goal to include most of the source flux within a relatively compact scale. Conceptually, we need to define an aperture to measure fluxes within the core scale, which is embedded inside the larger clump. The preferred method is to use a fixed aperture size at all wavelengths, i.e., the one defined by the $70\ \mu\text{m}$ and/or $37\ \mu\text{m}$ images (see Section 3.1.1). Background subtraction is carried out by estimating the average background intensity in an adjacent annulus, i.e., from one to two aperture radii, but excluding any regions that are within the aperture of another defined source (this is especially relevant for the *clustered* sources to be studied in Paper V, but also for some sources previously studied in Papers I–III). The estimator used is the median value in the annulus. Then this value is multiplied by the area of the main aperture to account for the background in the entire aperture.

SedFluxer uses a number of functions from the Photutils (Bradley et al. 2020) and astropy (Astropy Collaboration et al. 2013, 2018) python packages to measure fluxes on any image, including unit transformation (provided correct units are present in the header). These tools set the workflow for the parameters of SOMA studies as described above, but complete freedom is given to the user to change the inputs to their needs. SedFluxer can be used either with or without the use of SedFitter (see Section 3.2).

3.1.1. Optimal Aperture Algorithm

With the release of *sedcreator*, we have also developed a new algorithm to choose the aperture size in an unbiased and reproducible way for extended sources. The algorithm selects the optimal aperture radius for a given source through the following process. First, it samples a range of aperture radii within a user-defined lower and upper boundary and with a given step size. Next, it calculates the background-subtracted flux enclosed by each sampled aperture. Starting from the innermost scale, the algorithm searches for the condition when a 30% increase in the radius results in a smaller than 10% increase in the background-subtracted flux. The first time this condition is met defines the radius of the optimal aperture. However, if the condition is not met in the search range, then the radius is set to the location where the smallest fractional increase in background-subtracted enclosed flux occurs. To assess the performance of this algorithm, we made an experiment retrieving the optimal aperture for an artificial 2D Gaussian profile with an idealized background set at zero counts. For this case, an aperture is set at a radius of $\sim 2.2 \times \text{FWHM}$, which retrieves $\sim 90\%$ of the total flux.

Figure 1 shows an example for the source AFGL 2591. The top panel shows the $70\ \mu\text{m}$ image with the optimal aperture represented by the inner circle and the annular region used for background estimation for this aperture being from the inner to outer circles. The bottom panel shows the dependence of background-subtracted flux on the aperture radius, with the vertical black line indicating the radius of the optimal aperture. For all the sources analyzed in this paper, we have used the optimal aperture calculated using the Herschel $70\ \mu\text{m}$ image, or if this was not available, then the SOFIA $37\ \mu\text{m}$ image.

3.1.2. Error Estimation

In previous SOMA papers, we have assumed as the error estimator for the fluxes, the background measured in the annulus region (see Section 3.1). In this paper, we revise the

method for estimating the errors for those wavelengths that are not affected (or negligibly affected) by cold clump contamination, i.e., $\lambda < 100\ \mu\text{m}$. For longer wavelengths ($\lambda \geq 100\ \mu\text{m}$), we still use the background error as the emission at Herschel bands, especially those at 160, 250, 350, and $500\ \mu\text{m}$ are contaminated by the emission of the cold clump.

For the new error estimator, the fluctuations on the flux in a region from the annulus equivalent to the main aperture is evaluated. Therefore, the annulus region is divided into three sectors with areas equal to the circle of the main aperture with radius r . Recall that the fiducial case for the annulus definition is to take $r_{\text{inner}} = r$ and $r_{\text{outer}} = 2r$. Therefore, the area of each of the three sectors ($\pi(r_{\text{outer}}^2 - r_{\text{inner}}^2)/3 = \pi r^2$) is equal to the area of the main aperture (πr^2). To simplify, each sector is approximated by four circles with radius $r/2$ (which sum an area of $4\pi(r/2)^2 = \pi r^2$). We then estimate the fluctuation of the three sectors by calculating the standard deviation in their measurements. In order to avoid bias and missing regions within the annulus, the three sectors are aliased 6 times, from 0° – 75° in steps of 15° , to cover the full annulus. For each aliased position, the standard deviation of the measurement of the three sectors is calculated. Finally, the mean value of the six standard deviations is calculated and considered as the fluctuation error.

For the final error considered in the fits, a systematic error of 10% of the background-subtracted flux is added in quadrature to each error estimator, i.e., fluctuation error for $\lambda < 100\ \mu\text{m}$ and background error for $\lambda \geq 100\ \mu\text{m}$.

3.2. SedFitter

SedFitter is an update of the IDL code that fits a given SED with the RT model grid of ZT18, see Section 3.2.1 for more details about the model grid. The main changes in the code include: (i) the method of convolution of instrument filter profiles and foreground extinction and (ii) the methods of fitting models to data. Regarding (i), in the IDL code unextincted model SEDs were convolved by the filter responses to obtain model fluxes of each band, which were then extinguished with a given level of foreground extinction evaluated at a reference wavelength for each filter. We have updated this aspect to first apply foreground extinction to the models, i.e., with a finite grid of foreground extinction values, and then convolve these SEDs with the filter response functions. It is worth noting that the model flux computed with these two methods does not change dramatically, but this still can introduce modest differences in the properties of the best-fitted physical model results.

Regarding (ii), the previous IDL version did a grid search for every physical model (i.e., 8640 models including different inclinations of viewing angle). For every value of the visual extinction that was considered in the array, the χ^2 was calculated and the best one kept. Finally, all models were ordered based on this χ^2 value to yield a final result of 8640 models, each with their best visual extinction. To improve efficiency, for each of the 8640 models, we now minimize the χ^2 function (see Equation (1) in De Buizer et al. 2017) over A_V using the python package *scipy.optimize* (in particular, the routine *minimize*). We now calculate the χ^2 function with fluxes and errors in linear space. This allows us to better constrain the model grid as the bad models will have a very large χ^2 value. The new version includes an “idl” method for backward

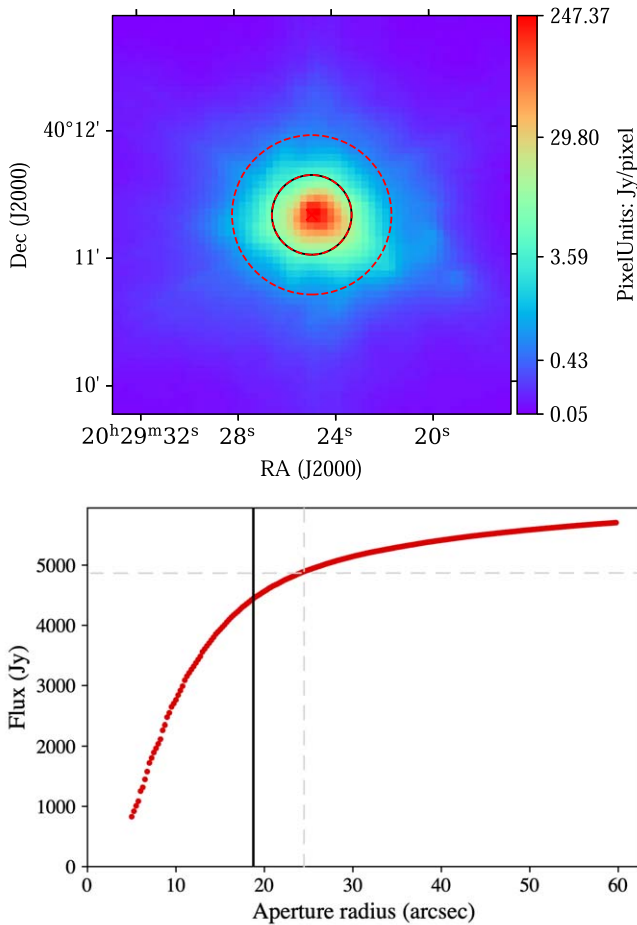


Figure 1. Demonstration of the optimal aperture algorithm for the AFGL 2591 source. Top panel: Herschel 70 μm image of AFGL 2591 with logarithmic intensity stretch. The inner circle is the optimal aperture chosen by the algorithm and the region from the inner to outer circle defines the annulus over which the background emission is estimated. Bottom panel: background-subtracted flux vs. aperture radius. The vertical black line shows the radius of the optimal aperture, while the horizontal and vertical gray dashed lines indicate the 10% increase in flux and 30% increase in radius, respectively, with respect to the optimal aperture for reference (see the text).

compatibility and to be able to reproduce the results of Papers I–III using the exact method of the older IDL code.

3.2.1. Zhang and Tan Model Grid

Here, we provide basic information on the RT model from the Zhang and Tan (ZT) series, but more details can be found in Section 2.2 in De Buizer et al. (2017), Liu et al. (2019b), and ZT18.

Based on the turbulent core model from McKee & Tan (2003), the evolution of high- and intermediate-mass protostars has been developed in a series of papers (Zhang & Tan 2011; Zhang et al. 2013a, 2014b; ZT18). For massive star formation, the initial conditions are pressurized, dense, massive cores embedded in high-mass surface density clump environments. Massive stars are assumed to form from preassembled massive prestellar cores supported by internal pressure from a combination of magnetic fields and turbulence. In these models, there are two main parameters that set the initial conditions: the initial mass of the core (M_c) and the mean mass surface density of the clump environment (Σ_{cl}). A third parameter is the protostellar mass (m_*), which defines the location along an

evolutionary track from a given initial condition. The properties of protostellar cores, including the protostar, disk, infall envelope, outflow, and their evolution, are calculated self-consistently from the given initial conditions. There are also two secondary parameters, which are the inclination angle of the line of sight to the outflow axis (θ_{view}), and the level of foreground extinction (A_V). Thus, there are five parameters ($M_c - \Sigma_{cl} - m_* - \theta_{\text{view}} - A_V$) that determine a protostellar SED, i.e., which are constrained by fitting the model grid to a given observed SED. We note that other properties, such as accretion rate, infall envelope mass, outflow cavity opening angle, and disk size, are prescribed for a given set of values of $M_c - \Sigma_{cl} - m_*$.

In the current model grid (ZT18) the main parameters are sampled as follows: M_c is sampled at 10, 20, 30, 40, 50, 60, 80, 100, 120, 160, 200, 240, 320, 400, and $480 M_\odot$ and Σ_{cl} is sampled at 0.10, 0.316, 1.0, and 3.16 g cm^{-2} , which makes a total of 60 evolutionary tracks. For each track, m_* is sampled at 0.5, 1, 2, 4, 8, 12, 16, 24, 32, 48, 64, 96, 128, and $160 M_\odot$ (although not all these masses are feasible from a given initial core, which typically has a formation efficiency of about 50%). In the end, this yields a total of 432 physical models that have different combinations of $M_c - \Sigma_{cl} - m_*$. Then, for each physical model, there are 20 viewing angles sampled uniformly at $\cos \theta_{\text{view}} = 0.975, 0.925, \dots, 0.025$, i.e., equally distributed from 1 (face-on) to 0 (edge-on). Therefore, we have $432 \times 20 = 8640$ model SEDs. Finally, the visual extinction is constrained from $A_{V,\text{min}}$ to $A_{V,\text{max}}$, which are user-defined values (with the default set to 0–1000 mag).

3.2.2. Average “Good” Models

It is known that SED fitting is subject to degeneracies, i.e., a range of protostellar properties can yield SEDs that are consistent with a given observed SED. Thus, rather than only consider the best-fitting model, we also evaluate an average of good models, with these defined via set criteria on the reduced χ^2 of the fit. We adopt the following method for this averaging. We consider all physical models, including different viewing angles, i.e., 8640 models, and evaluate the value of χ^2 of the best model, i.e., χ^2_{min} . If $\chi^2_{\text{min}} < 1$, then we average over all models that satisfy $\chi^2 < 2$. If $\chi^2_{\text{min}} > 1$, then we average over all models that satisfy $\chi^2 < 2\chi^2_{\text{min}}$. As our fiducial method, we also require models to satisfy the condition that $R_{\text{core}} < 2R_{\text{ap}}$, i.e., we only consider models where the radius of the core is within the chosen aperture radius (within a factor of 2). Note, we first apply the cut in aperture radius to define the best-allowed model and then apply the χ^2 cut. Model properties are averaged in log space, i.e., geometric means, except for A_V , θ_{view} , and $\theta_{\text{w,esc}}$, which are averaged in linear space, i.e., arithmetic means.

3.3. 2D Gaussian Fitting on IRAS-HIRES Images

Since our sources are not resolved in IRAS-HIRES images, we perform two-dimensional Gaussian fitting to derive the source flux, in order to reduce potential contamination from nearby sources. We extract a square area containing the source on the HIRES image for the 2D Gaussian fitting and explore how the choice of fitting area affects the result, i.e., by varying the size of the side of the square from 1.5–2.0 times the IRAS beam major axis.

The resolution in the HIRES image is not the same across an entire image.¹⁴ HIRES provides beam sample maps, which consist of a field of point-source spikes superimposed on a highly smoothed version of the image, as well as the corresponding beam FWHM and position angle (P.A.) at each location. We tried two ways to perform the 2D Gaussian fitting: (1) treating all the parameters as free parameters and (2) deriving the major and minor FWHM and the P.A. from the beam profiles provided by HIRES and keeping them fixed, and then fitting for the other parameters of the 2D Gaussian. Most of the time we used the beam profile located at the center of the map, where the source is located. But occasionally the beam profiles are significantly impacted by source strength, and in these cases, we find the nearest beam profile that is not contaminated to make sure the beam profile is consistent with the appearance of the unresolved source in the image. We note that this method of Gaussian fitting also includes a constant background term, so the derived flux can be considered to be background subtracted.

4. Results

4.1. Individual Sources

Below we describe the main properties of each source, along with a description of the new SOFIA-FORCAST images and relevant ancillary data.

4.1.1. AFGL 2591

AFGL 2591, also known as IRAS 20275+4001, was first reported in the literature by Rieke et al. (1973), although they stated that it was discovered in a survey by Walker & Prince in 1972. It was then observed in the IR from 2.8–14 μm by Merrill & Soifer (1974), where they discussed the remarkable similarity of AFGL 2591 with the BN object in Orion. Wynn-Williams et al. (1977) reported radio and IR observations to confirm that the IR source and the ultracompact (UC) H II region, initially thought to coincide, are separated by 7". They also observed an H₂O maser coinciding with the IR source. This maser was later used to determine a distance of 3.33 ± 0.11 kpc from its trigonometric parallax with the Very Long Baseline Array (VLA; Rygl et al. 2012). Simon et al. (1981) observed this region with the VLA at 6 and 2 cm. They confirmed the findings of Wynn-Williams et al. (1977) and tentatively associated a weak radio source with the IR source. Subsequently, many radio sources have been detected in this star-forming region. VLA 1, 2, 4, and 5 have been classified as H II regions (Trinidad et al. 2003; Johnston et al. 2013), whereas VLA 3 has been identified as the main high-mass protostar (Trinidad et al. 2003; Gieser et al. 2019). Indriolo et al. (2015) used SOFIA/EXES to observe the ν_2 rovibrational band of water in the MIR 6.086–6.135 μm range and suggested that the background source is only partially covered by the absorbing gas or that the absorption arises within the 6 μm emitting photosphere. AFGL 2591 was also observed as part of the CORE survey at 1.37 mm with NOEMA where the authors concluded that this source contains three cores that have a mean separation of about 15,000 au (Beuther et al. 2018a).

AFGL 2591 drives a powerful molecular outflow as revealed by CO and HCO⁺ observations (Bally & Lada 1983; Lada et al. 1984; Hasegawa & Mitchell 1995). This outflow is oriented toward the east–west direction with an approximate

P.A. of 260°, an extent of ~ 1.5 pc, and a dynamical age of $\sim 2 \times 10^4$ yr (Poetzel et al. 1992; Preibisch et al. 2003). The presence of the outflow is hinted at in Figure 2 as all SOFIA images show some extension in the east–west direction. The NIR *K* band image at $\sim 2 \mu\text{m}$ shows a well-defined conical structure delineating the outflow cavity walls (e.g., Hodapp 1994). Poetzel et al. (1992) found several Herbig–Haro (HH) objects toward the main IR source. They found [N II] and [S II] emission in the optical and H₂ in the NIR and measured radial velocities in the range of 200–500 km s^{−1}. The blueshifted lobe of the outflow is located toward the west and the redshifted lobe is toward the east (e.g., Poetzel et al. 1992; Preibisch et al. 2003; Olguin et al. 2020). Hasegawa & Mitchell (1995) estimated an opening angle of $< 90^\circ$ and an inclination angle to the line of sight of $< 45^\circ$ from CO emission. The inclination angle was later constrained to a range between 26° and 38° (van der Tak et al. 2006), although other values have been found by fitting the SED (e.g., Johnston et al. 2013; Simpson et al. 2013). See Olguin et al. (2020) for a comprehensive and extensive review of this object. On the large scale, multiple studies have argued that the H II region is part of a larger star cluster that is revealed in NIR imaging, but in the MIR images, this source appears to be isolated.

Figure 2 shows the multiwavelength images of AFGL 2591. The peak emission at IR wavelengths coincides with the position of the VLA 3 source at 3.6 cm (Trinidad et al. 2003). In the SOFIA images, there is an elongation in the SW–NE direction, which suggests the presence of an outflow consistent with previous studies (Poetzel et al. 1992; Preibisch et al. 2003). In fact, this elongation is brighter to the west of the centimeter peak, further suggesting that the blueshifted outflow is located toward this direction and the redshifted outflow toward the east (see also Figure 5 of Preibisch et al. 2003).

4.1.2. G25.40-0.14

Located at 5.7 kpc (Zhu et al. 2011; Ai et al. 2013), G25.40-0.14 is a UC H II region with a core halo structure (Garay et al. 1993), also referred to as G25.4NW in Dewangan et al. (2015). Even though G25.40-0.14 lies in the direction of W42, it is not thought to be associated with the W42 complex due to its very different ¹³CO velocity components (58–69 km s^{−1} for W42 and 88–109 km s^{−1} for G25.40-0.14) as discussed by Ai et al. (2013) and Dewangan et al. (2015). Ai et al. (2013) estimated a bolometric luminosity of $10^{5.6} L_\odot$ for this region, which corresponds to a 06 zero-age main-sequence star (ZAMS). The source also sits in the direction of the bipolar nebula N39 (Churchwell et al. 2006; Beaumont & Williams 2010; Deharveng et al. 2010). Deharveng et al. (2010) found a filament or sheet-like structure along the bipolar nebula, which is also seen in the 8 μm image.

The SOFIA images show clearly the core halo structure (Figure 3). The brightest IR emission is located at the centimeter peak (Givon et al. 2005) and an arc-like structure is seen toward the south. An extension to the NW is also seen, as well as a potential secondary source to the NE.

4.1.3. G30.59-0.04

G30.59-0.04 was first identified in a VLA survey by Fish et al. (2003). Some studies (e.g., Hill et al. 2009) adopt a near 3 kpc distance, while others (e.g., Fish et al. 2003) adopt a far distance of 11.8 kpc. The studies using the near distance

¹⁴ <https://irsa.ipac.caltech.edu/applications/Hires/docs/instructions.html>

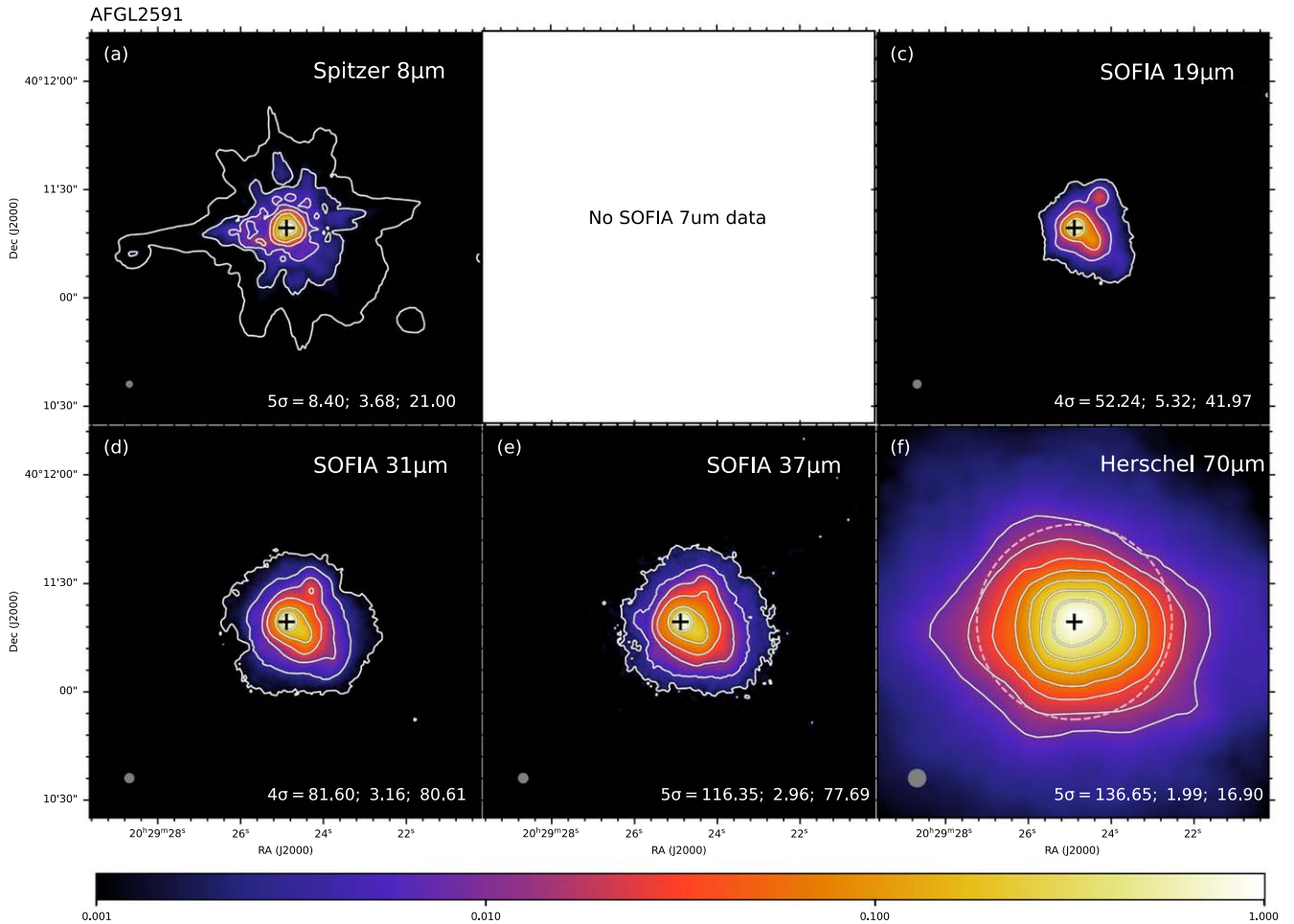


Figure 2. Multiwavelength images of AFGL 2591 with the facility and wavelength given in the upper right of each panel. Contour level information is given in lower right: lowest contour level in the number of sigma above the background noise and corresponding value in millijansky per square arcsec; then the step size between each contour in \log_{10} millijansky per square arcsec, then peak flux in jansky per square arcsec. The color map indicates the relative flux intensity compared to that of the peak flux in each image panel. The pink dashed circle shown in (f) denotes the aperture used for the fiducial photometry. Gray circles in the lower left show the resolution of each image. The black cross in all panels denotes the position of the 3.6 cm radio source VLA 3 in Trinidad et al. (2003) at R.A. (J2000) = $20^{\text{h}}29^{\text{m}}24^{\text{s}}.8916$, decl. (J2000) = $+40^{\circ}11'19''.388$. The data used to create this figure and the SED are available.

(The data used to create this figure are available.)

adopted such a distance for consistency among samples (e.g., Hill et al. 2009). In the same study, the authors checked and argued that the near-distance assumption has no strong influence on the conclusion in their study. On the other hand, studies such as that of Purcell et al. (2006), which attempted to resolve the ambiguity, favor the far distance of 11.8 kpc using the technique presented in Solomon et al. (1987), see also Table 2 in Purcell et al. (2006) assuming the Galactic rotation curve of Brand & Blitz (1993). Recently, the source distance was reevaluated by Mège et al. (2021) as part of the Hi-GAL survey. They found a distance of 11.7 kpc, consistent with that found by Urquhart et al. (2018) in the ATLASGAL survey (11.5 kpc). Hence, we also adopt the far distance in this work. Hill et al. (2009) performed SED analysis and estimated that the clump has upper limits of mass and luminosity of $1200 M_{\odot}$ and $2.4 \times 10^4 L_{\odot}$, respectively. We recomputed the luminosity given by Hill et al. (2009) using the far distance as assumed in our work and obtained a value of $3.5 \times 10^5 L_{\odot}$.

Figure 4 shows multiwavelength images of G30.59-0.04, where one main source is identified. In the SOFIA 7 μm image

there are two tentative detections of secondary sources toward the south and SW of the centimeter peak, which are also seen in the Spitzer 8 μm image. There is a hint of elongation in the NE to the SW direction, especially clear in the SOFIA 19 and 37 μm images.

4.1.4. G32.03+0.05

G32.03+0.05 was first reported as part of the 5 GHz VLA Survey of the Galactic plane carried out by Becker et al. (1994). The authors associated the source at 6 cm with IRAS 18470-0050 as their radio and the IR coordinates differed by less than $2''$. Later, this source was also part of the deeper VLA survey by White et al. (2005), where they confirmed the detection at 6 cm of Becker et al. (1994), but reported non-detection at 20 cm. The coordinates reported in Figure 5 are the ones from White et al. (2005). The near (5.5 kpc) and far (8.7 kpc) kinematic distances were reported for this region by Anderson et al. (2012). In this work, we assume the near distance, following Battersby et al. (2014).

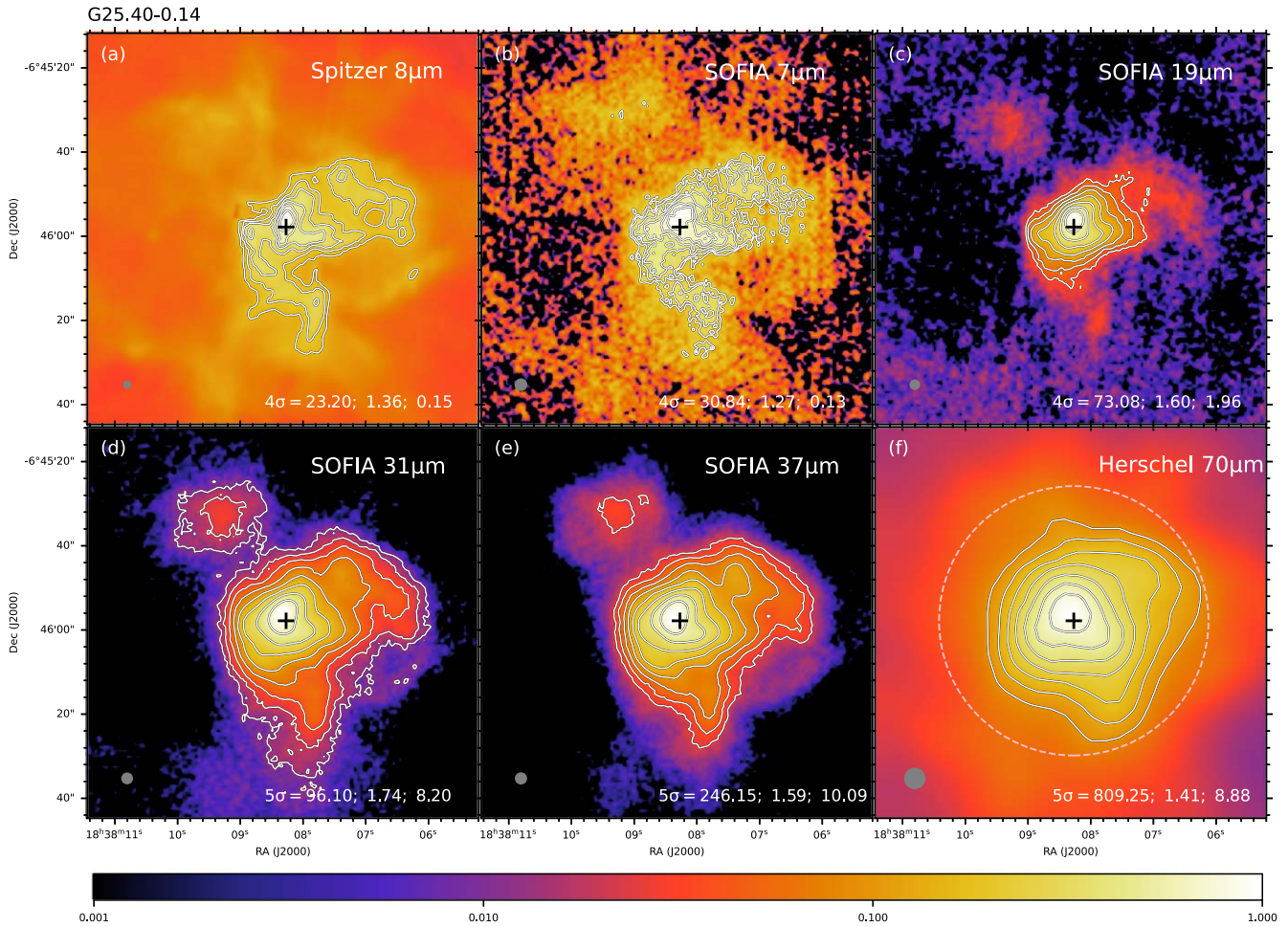


Figure 3. Multiwavelength images of G25.40-0.14, following the format of Figure 2. The black cross in all panels denotes the peak position of the 6 cm continuum emission from Givoe et al. (2005) at R.A. (J2000) = $18^{\text{h}}38^{\text{m}}08^{\text{s}}.270$, decl. (J2000) = $-06^{\circ}45'57''.82$. The data used to create this figure and the SED are available. (The data used to create this figure are available.)

Battersby et al. (2014) observed the IRDC G32.02+0.06 region in $\text{NH}_3(1, 1)$, $(2, 2)$, and $(4, 4)$ with VLA. They identified two main clumps, which they denoted active and quiescent. Our source is located within the active clump, which they find has a mass of $\sim 5000\text{--}10,000 M_{\odot}$ and displays clear signs of star formation. This includes the presence of a 6.7 GHz methanol maser (Pestalozzi et al. 2005), emission at 8 and $24 \mu\text{m}$, and radio continuum emission (White et al. 2005). Battersby et al. (2014) identified our main source (which corresponds to the bright source toward the south in Figure 5) as a young UC H II region and no NH_3 cores were observed here.

The source toward the north shown in our Figure 5, is identified in Battersby et al. (2014) as a warm core complex and includes three NH_3 cores (cores 2, 6, and 8), which all show clear signatures of $\text{NH}_3(1,1)$, $(2,2)$ and $(4,4)$ emission. From these data, core masses of $\sim 100 M_{\odot}$ and temperatures of 25 K were estimated (see Table 2 of Battersby et al. 2014, for the properties derived).

Figure 5 shows the multiwavelength images of G32.03+0.05. In the IR images, two sources are clearly visible, consistent with previous studies. We treat the southern source that coincides with the centimeter peak as the primary. We carried out an SED analysis for both sources. So this region yields two protostars for our sample.

4.1.5. G33.92+0.11

G33.92+0.11 has been classified as a cometary UC H II region, with an estimated distance of 7.1 ± 1.3 kpc and a systemic velocity of 107.6 km s^{-1} (Fish et al. 2003; Liu et al. 2015). Liu et al. (2012) described the dense gas in the region as having a hub-filament structure, with multiple parsec-long and spiral-like filaments converging to the central massive ($\sim 3 \times 10^3 M_{\odot}$) hub (Liu et al. 2015). Atacama Large Millimeter/submillimeter Array observations were performed toward the inner region of the filaments (Liu et al. 2019a). The authors argued that the filaments are feeding a massive OB protocluster by gravitationally driven inflow and resolved the inner structures down to 1000 au scales. Five outflow sources were identified in the study by Liu et al. (2012) with $^{12}\text{CO}(2\text{--}1)$ and shock tracers such as $\text{SiO}(5\text{--}4)$, SO, and OCS. The authors identified high-velocity molecular gas toward the five regions as high as 31.4 km s^{-1} . Assuming an excitation temperature of 50 K and $X(\text{CO}) = 10^{-4}$, the authors estimated the outflow mass, momentum, and energy of the outflows. The upper limits are $2.3 M_{\odot}$, $12 M_{\odot} \text{ km s}^{-1}$, and $20 \times 10^{44} \text{ erg}$, respectively. The source also presented high chemical complexity with the detection of various hot core lines (Minh et al. 2016, 2018).

The multiwavelength images of G33.92+0.11 are shown in Figure 6. The SOFIA $7 \mu\text{m}$ morphology resembles that seen in

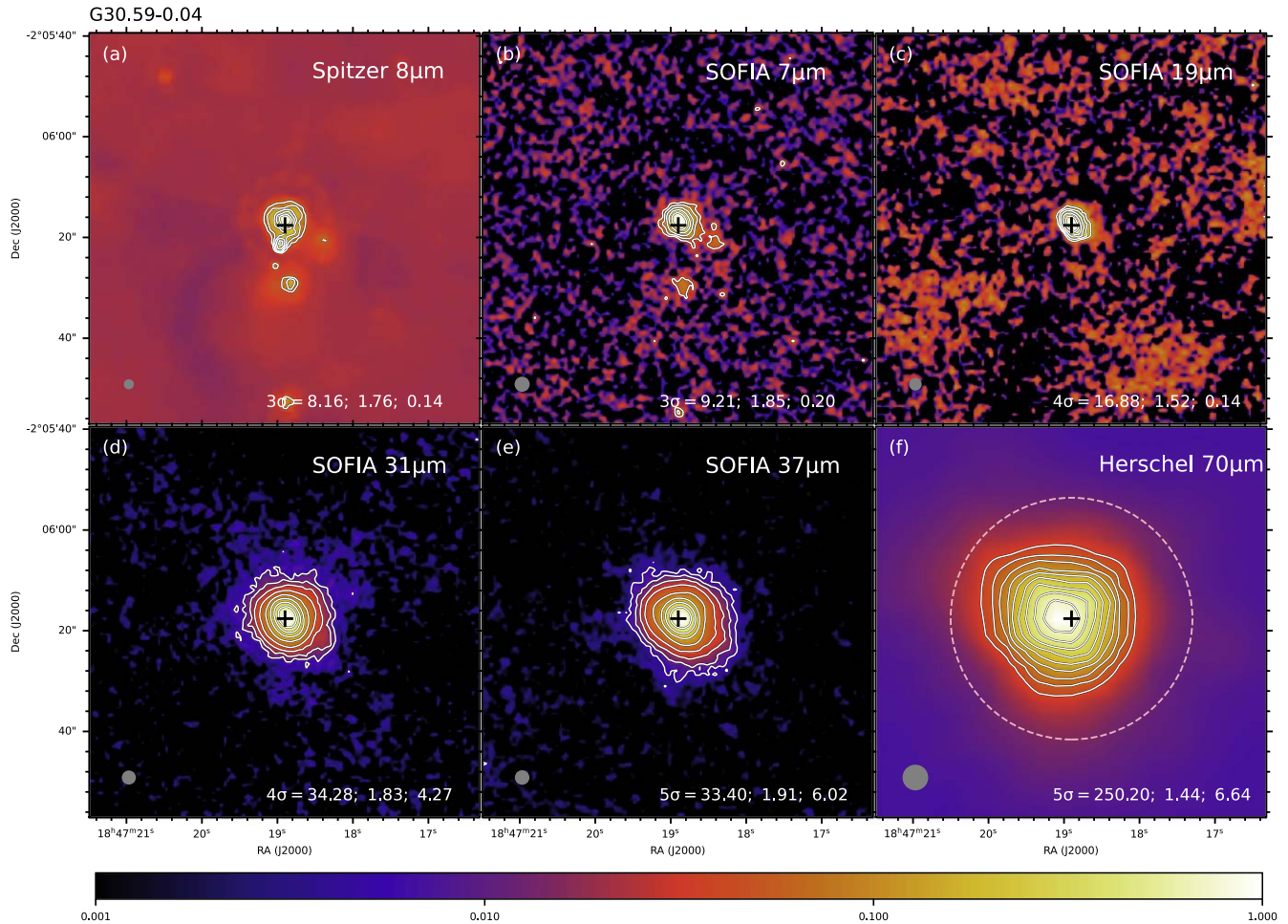


Figure 4. Multiwavelength images of G30.59-0.04, following the format of Figure 2. The black cross in all panels denotes the peak position of the 6 cm continuum emission from Givoeon et al. (2008) at R.A. (J2000) = $18^{\text{h}}47^{\text{m}}18^{\text{s}}.9$, decl. (J2000) = $-02^{\circ}06'17''.6$. The data used to create this figure and the SED are available. (The data used to create this figure are available.)

the Spitzer $8\ \mu\text{m}$ image and shows the arc-like structure toward the east of the centimeter peak. Longer wavelengths also show stronger emission to the east, including the Herschel $70\ \mu\text{m}$ image. There is a source to the west of the main protostar that is detected in the Spitzer $8\ \mu\text{m}$, but which is not seen in the SOFIA $7\ \mu\text{m}$ or other images. This may indicate that this source is variable, potentially being a protostar that has evolved from an outbursting active state to a quiescent one during the last ~ 10 yr. However, the observations for this source were also affected by the so-called *window contamination* problem, which can prevent the observation of faint sources in the field.

4.1.6. G40.62-0.14

G40.62-0.14, also known as IRAS 19035+0641, is a massive star formation region located at 2.2 kpc and with a bolometric luminosity of $\sim 8 \times 10^3 L_{\odot}$ (Sridharan et al. 2002). Single-dish data toward G40.62-0.14 shows the presence of CO and HCO^+ molecular outflows (Beuther et al. 2002a; López-Sepulcre et al. 2010) oriented in the NW–SE direction. Sánchez-Monge (2011) reported two radio continuum emission sources in this region: I19035-VLA1, a small cometary UC H II region and I19035-VLA2, a very faint (4σ) detection. Furthermore, Rosero et al. (2016) confirmed the detection of I19035-VLA2 (their source 19035+0641 A) and reported that

the source has a jet-like morphology oriented in the NE–SW direction. Based on the spectral index, the centimeter emission morphology and associations with outflow tracers (e.g., maser emission and molecular emission), Rosero et al. (2019b) concluded that I19035-VLA2 is an ionized jet. Also, they show that this source is associated with NIR emission seen by UKIDSS, which is elongated in the same direction as the ionized jet and is most likely tracing scattered light from the central young stellar object (YSO) that is escaping through an outflow cavity. I19035-VLA2 is reported to have very weak or no H_2 emission (Rosero et al. 2019b). I19035-VLA2 is located at the peak of the main ammonia clump detected toward this region and the ammonia emission has a velocity gradient in the same direction as the molecular outflow detected in the region (Sánchez-Monge et al. 2011). I19035-VLA2 is associated with 6.7 GHz CH_3OH , H_2O (Beuther et al. 2002b; Rosero et al. 2019b), and OH maser emission, with the latter two distributed linearly in the same direction as the ionized jet and interpreted by De Buizer et al. (2005) as tracing the outflow into the cavity. I19035-VLA2 is spatially associated with MIR emission seen by Spitzer/IRAC (Sánchez-Monge et al. 2011), likely tracing dust emission from a deeply embedded YSO. I19035-VLA2 is the source that coincides with our MIR peak at $39\ \mu\text{m}$. I19035-VLA1 is offset from the peak of the MIR and NIR emission

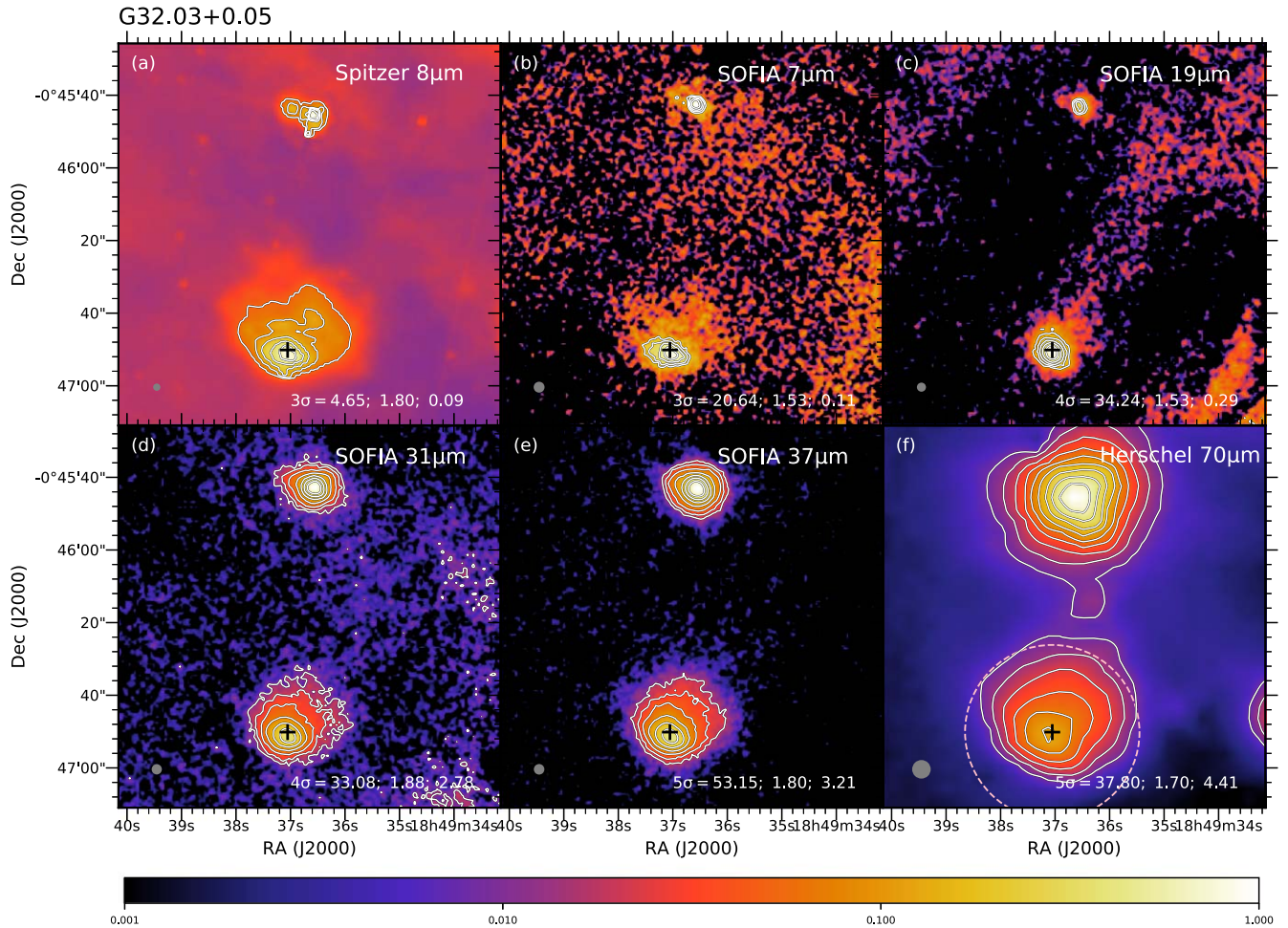


Figure 5. Multiwavelength images of G32.03+0.05, following the format of Figure 2. The black cross in all panels denotes the peak position of the 6 cm continuum emission from White et al. (2005) at R.A. (J2000) = $18^{\text{h}}49^{\text{m}}37^{\text{s}}.052$, decl. (J2000) = $-00^{\circ}46'50''.15$. The secondary source toward the north, denoted G32.03+0.05N, has central coordinates R.A. (J2000) = $18^{\text{h}}49^{\text{m}}36^{\text{s}}.55$, decl. (J2000) = $-00^{\circ}45'42''.40$. The data used to create this figure and the SED are available.

(The data used to create this figure are available.)

and the millimeter clump. Rosero et al. (2019b) suggest that based on its low emission measure and electron density, I19035-VLA1 is a UC H II region ionized by a B1 ZAMS star that has formed near the edge of the dust clump where the density of the surrounding medium is much lower than in the center. With this picture, G40.62-0.14 is composed of I19035-VLA2, a YSO that is deeply embedded in dust and it is the driving source of at least one of the molecular outflows detected in the region, and I19035-VLA1, which is a slightly more evolved stellar source. Rosero et al. (2019b) suggest that the observed misalignment between the centimeter continuum emission and the dominating molecular outflow in the region could be explained either by the existence of multiple overlapping outflows or by precession, where the outflow axis changes from the small to the large scale.

Figure 7 presents the multiwavelength images of G40.62-0.14. At wavelengths shorter than $19 \mu\text{m}$, the MIR data shows a weak source located slightly NE of the central emission. This source is not associated with any ionized emission or millimeter dust clump. Also, our SOFIA data at 31 and $37 \mu\text{m}$ and the Herschel $70 \mu\text{m}$ show a slight NE–SW elongation, which is in the same direction as the NIR emission and the ionized jet associated with I19035-VLA2. This suggests that the MIR/FIR

data is also tracing the outflow cavity driven by the YSO in I19035-VLA2.

4.1.7. IRAS 00259+5625

IRAS 00259+5625, also known as CB3 (Clemens & Barvainis 1988), is identified as a Bok globule. The large distance (2.5 kpc) and high luminosity make CB3 stand out from typical Bok globules, which are usually low-mass star-forming cores, suggesting that CB3 is an intermediate-mass star-forming region (Launhardt et al. 1997). Launhardt & Henning (1997) estimated a kinematic distance of 2.4 kpc (which is the one adopted in this work), while Yun & Clemens (1994) obtained a CO velocity distance of 2.1 kpc using the rotation curve in Clemens (1985). The water maser’s proper motion suggests a distance of $2.6^{+1.0}_{-0.6}$ kpc, consistent with previous estimates (Sakai et al. 2014). Launhardt & Henning (1997) compiled the 12–1300 μm flux of the continuum source, CB3-mm, and derived a luminosity of $930 L_{\odot}$ and a gas mass of $72 M_{\odot}$. Using PdBI, Fuente et al. (2007) resolved the continuum source into a binary source at 1.3 and 3 mm, CB3-1 ($00^{\text{h}}28^{\text{m}}42^{\text{s}}.6/56^{\circ}42'01''.11$) and CB3-2 ($00^{\text{h}}28^{\text{m}}42^{\text{s}}.2/56^{\circ}42'05''.11$), separated by 0.06 pc ($\sim 5''$ at a distance of 2.5 kpc). The mass of CB3-1 and CB3-2 derived from the 1.3 mm emission is 0.62 and $0.24 M_{\odot}$,

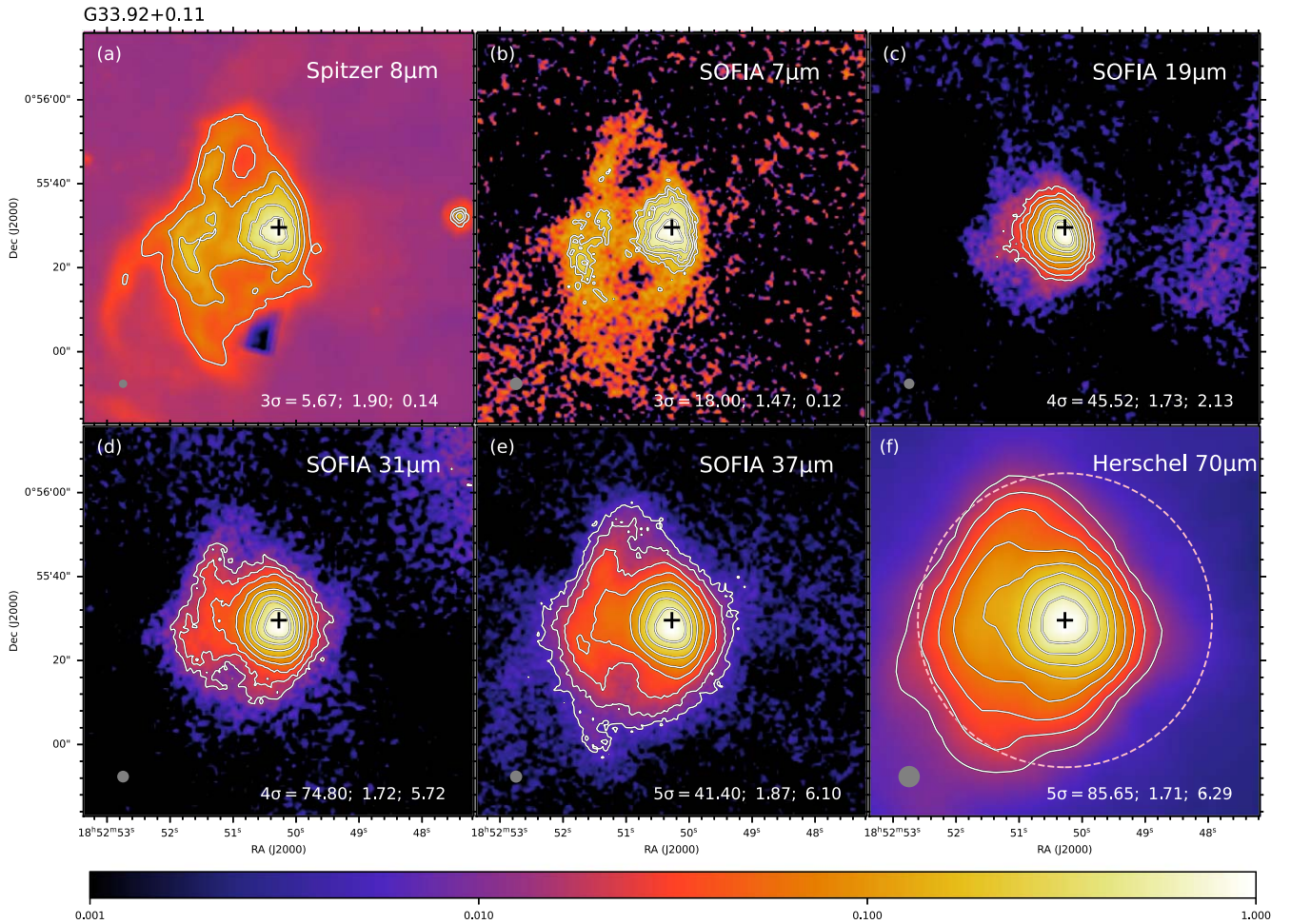


Figure 6. Multiwavelength images of G33.92+0.11, following the format of Figure 2. The black cross in all panels denotes the peak position of the 2.7 mm, 2 cm, and 3.6 cm continuum emission from Watt & Mundy (1999) at R.A. (J2000) = $18^{\text{h}}52^{\text{m}}50^{\text{s}}.273$, decl. (J2000) = $+00^{\circ}55'29''.594$. The data used to create this figure and the SED are available.

(The data used to create this figure are available.)

respectively. Yun & Clemens (1995) identified a source in *J*, *H*, and *K* bands at $\sim 32''$ ($00^{\text{h}}28^{\text{m}}46^{\text{s}}.3/56^{\circ}41'38''$) to the east of the millimeter source; however, no corresponding continuum source has been found in submillimeter and millimeter wavelengths. Clear outflow signatures in the north–south direction have been detected in CO, CS, SO, SO_2 , SiO, and CH_3OH , where the SiO and CH_3OH show collimated jet-like morphology (Yun & Clemens 1994; Launhardt et al. 1998; Codella & Bachiller 1999). In particular, the SiO emission is directly associated with the binary source, showing two episodes of mass loss corresponding to a timescale of 10^4 and 10^5 yr (Codella & Bachiller 1999). At a scale of $\sim 5' \times 5'$, Lundquist et al. (2014) identified four candidate YSOs using Wide-field Infrared Survey Explorer (WISE) and Two Micron All Sky Survey (2MASS) photometry, including three intermediate-mass YSOs (4.0 , 2.8 , and $3.0 M_{\odot}$) and a low-mass YSO ($0.8 M_{\odot}$). All of this evidence suggests that the IRAS 00259+5625 is a Class 0 intermediate-mass star-forming cluster.

Figure 8 shows the SOFIA images of IRAS 00259+5625. Neither Spitzer nor Herschel data are available for this region. The SOFIA image at $19 \mu\text{m}$ does not show any clear emission for this source, in part because of extended diffuse emission, which is attributed to a window contamination problem

affecting this particular FORCAST observation. The source is detected in the longer-wavelength SOFIA images, which allow a flux measurement for the SED.

4.1.8. IRAS 00420+5530

IRAS 00420+5530, also known as Mol 3, is a high-mass protostellar candidate first identified by Molinari et al. (1996, 1998a). The distance to IRAS 00420+5530 is 2.17 ± 0.05 kpc, measured from the parallax of water masers (Moellenbrock et al. 2009; while Molinari et al. 2002 and Zhang et al. 2005 derived kinematic distances of 5.0 and 7.72 kpc, respectively). In this work, we adopt a distance of 2.17 kpc. Kumar et al. (2006) suggested the presence of a cluster of $380 M_{\odot}$ associated with IRAS 00420+5530. Using high-resolution interferometry, Molinari et al. (2002) detected two 3.4 mm continuum sources, MM1 ($00^{\text{h}}44^{\text{m}}58^{\text{s}}.2/55^{\circ}46'46''$) and MM2 ($00^{\text{h}}44^{\text{m}}57^{\text{s}}.3/55^{\circ}46'57''$), with an equal flux of ~ 0.5 mJy along with $\text{HCO}^+ J=1-0$ emission coincided with MM1. The separation between MM1 and MM2 is $\sim 10''$ with MM2 located to the NW. These authors also found two 3.6 cm sources, i.e., VLA 3, which is centered on MM1, and VLA 5, which is located $\sim 20''$ toward the NE. IRAS 00420+5530 also shows high-velocity CO emission with a complex morphology consisting of multiple

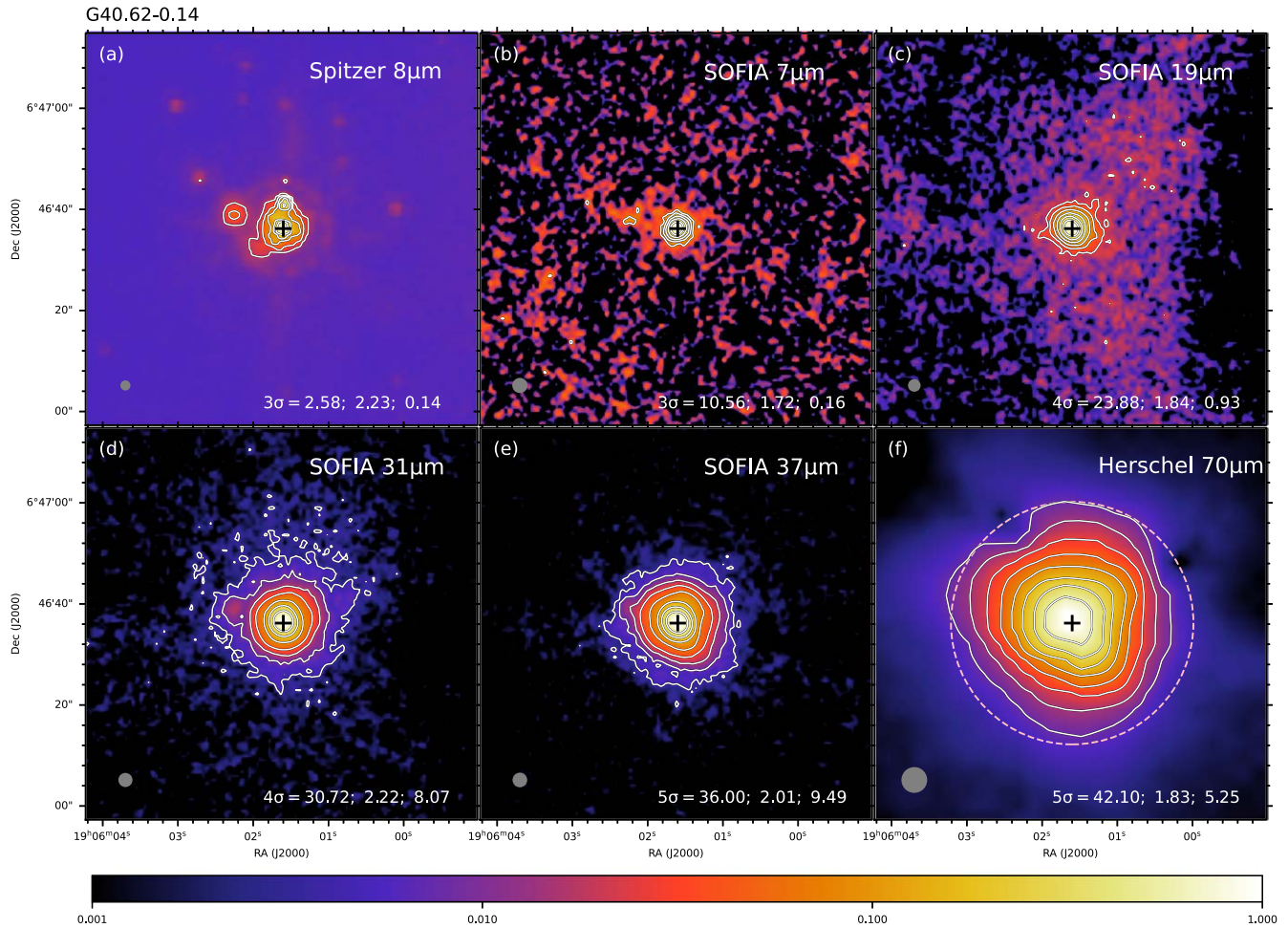


Figure 7. Multiwavelength images of G40.62-0.14, following the format of Figure 2. The black cross in all panels denotes the peak position of the 1.3 cm and 6 cm continuum emission of I19035-VLA2 in Rosero et al. (2016) at R.A. (J2000) = 19^h06^m01^s.60, decl.(J2000) = +06°46′36″.2. The data used to create this figure and the SED are available.

(The data used to create this figure are available.)

peaks (Zhang et al. 2005). The redshifted CO emission extends toward the south, while the blueshifted emission concentrates on the millimeter sources. Using WISE photometry and H₂ 2.12 μ m emission, Wolf-Chase et al. (2017) identified three Class I candidates and one Class 0 candidate in $\sim 2' \times 2'$ field around IRAS 00420+5530. The binaries MM1 and MM2 are classified as Class I candidates, and they are associated with a chain of H₂ knots. Most notably, they discovered an arc-like structure of strong H₂ emission to the north of the millimeter sources. A Class I candidate (00^h44^m57^s.3/55°47′18″.1) is identified at the apex of the arc. The other two sources are more than 30'' away from the millimeter sources. At a larger $\sim 12' \times 12'$ scale, Lundquist et al. (2014) identified nine YSOs using WISE and 2MASS photometry, including eight intermediate-mass YSOs and a low-mass YSO. Most of the YSOs are located at least $\sim 5'$ away to the west of the millimeter sources, while two YSOs are located at a separation of $\sim 0'.5-1'$.

Figure 9 shows the multiwavelength images for IRAS 00420+5530. Neither Spitzer nor Herschel data are available for this region. The shorter wavelength SOFIA images show high noise levels and extended emission that is expected to be caused by window contamination and no emission could be retrieved from these images. Longer-wavelength SOFIA images show

concentrated emission around the centimeter peak as well as extended emission toward the NW.

4.1.9. IRAS 23385+6053

IRAS 23385+6053, also known as Mol 160, was identified as a possible precursor of a UC H II region, located at 4.9 kpc (Molinari et al. 1996, 1998a, 1998b). Further observations from NIR to centimeter wavelengths revealed an embedded massive protostellar cluster, along with two H II regions at $\sim 30''$ to the east and $\sim 20''$ to the west (Molinari et al. 2002; Cesaroni et al. 2019). The powering sources of the two H II regions remain unclear. Molinari et al. (2008a) found bright 24 μ m emission surrounding the dominant continuum source. The 24 μ m emission shows an arc-like structure to the east of the dominant continuum source and another extended structure peaks at $\sim 30''$ to the west, which has been suggested as having originated from a photodissociation region due to the two H II regions. A massive core with a luminosity of $\sim 3000 L_{\odot}$ dominates the cluster, which is the point-like source detected by SOFIA-FORCAST (Fontani et al. 2004; Wolf-Chase et al. 2012). Observations of molecular emission, such as SiO and HCO⁺, show broad line widths, suggesting the presence of outflows. The HCO⁺ emission extends in the NE–SW direction

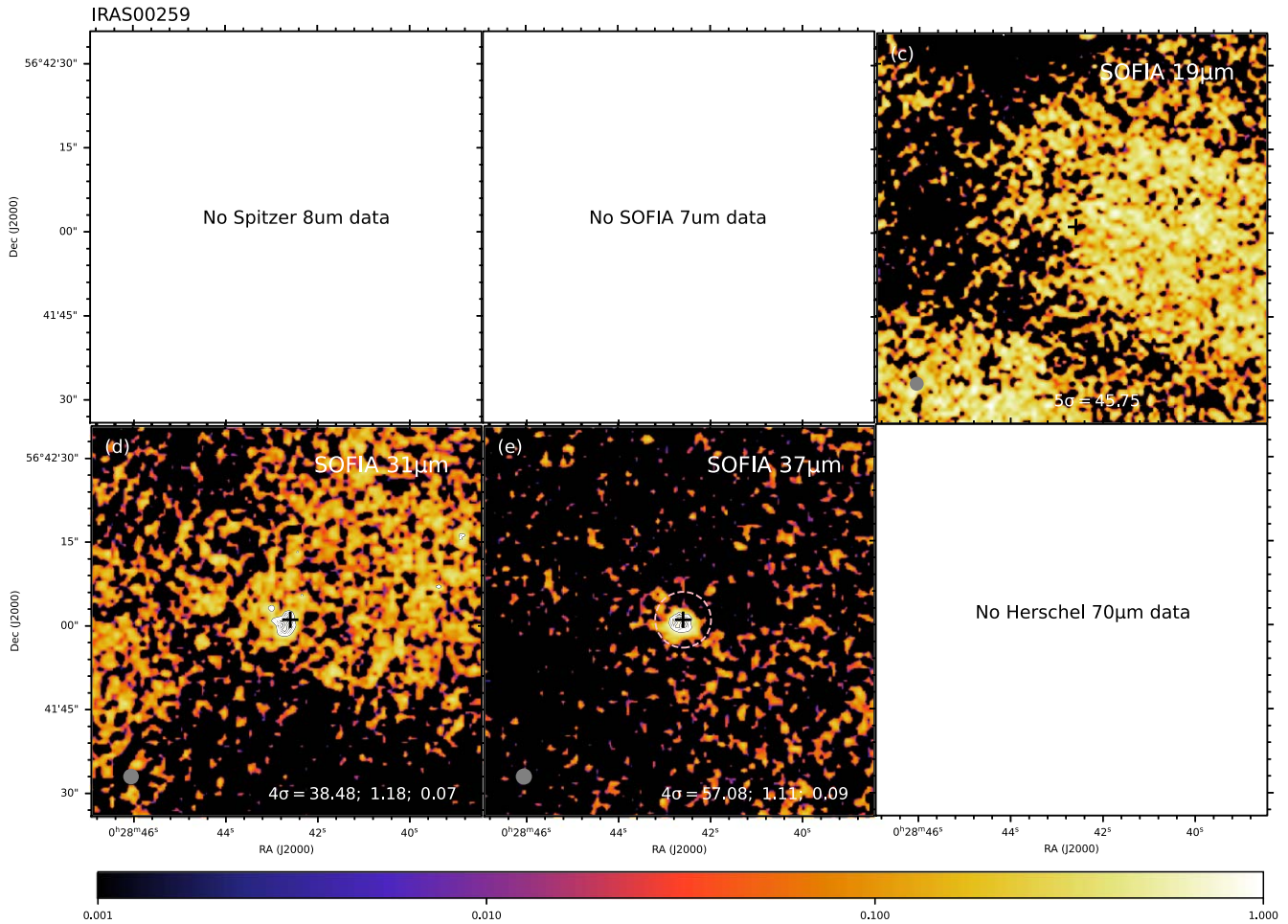


Figure 8. Multiwavelength images of IRAS 00259+5625, following the format of Figure 2. The black cross in all panels denotes the position of the 1.3 and 3.3 mm source CB3-1 from Fuente et al. (2007) at R.A. (J2000) = $0^{\text{h}}28^{\text{m}}42^{\text{s}}.60$, decl. (J2000) = $+56^{\circ}42'01''.11$. The data used to create this figure and the SED are available. (The data used to create this figure are available.)

with a velocity gradient, indicating a NE–SW outflow (Wolf-Chase et al. 2012). Similar outflow signatures are detected in H_2 $2.12\ \mu\text{m}$ emission (Wolf-Chase et al. 2012, 2017). Cesaroni et al. (2019) identified six cores in the cluster. The previously known massive core becomes a binary source, A1 and A2, each moving at a different velocity. The A2 source is half as massive as the A1 source and/or in an earlier evolutionary phase. Other cores are less massive and colder, appearing to be on the verge of collapse. By fitting a Keplerian rotating disk to the emission of CH_3CN , they further estimate a stellar mass of $\sim 9\ M_{\odot}$ in the A1 source. Molinari et al. (2008b) constructed a SED model grid assuming either an embedded ZAMS or a graybody envelope if the embedded ZAMS model fails. In the end, IRAS 23385+6053 was fitted with a graybody envelope model that has a L_{bol} of $1.75 \times 10^4 L_{\odot}$ and M_{env} of $222\ M_{\odot}$.

Figure 10 shows the IR images for IRAS 23385+6053. No Spitzer data are available for this source. The SOFIA images are relatively noisy and emission from the main source is only discernible at 31 and $37\ \mu\text{m}$. However, extended emission from an eastern arc, which is visible in the Herschel $70\ \mu\text{m}$ image, is also visible at 31 and $37\ \mu\text{m}$.

4.1.10. HH 288

The HH object HH 288 is located in the Cepheus region and it is associated with the exciting source IRAS 00342+6347

(Dent et al. 1998; Gueth et al. 2001). Wouterloot et al. (1993) reported H_2O masers in the surroundings of this source. Two bipolar outflows have been observed in molecular tracers, including $\text{CO}\ J=1-0$, $J=2-1$ in the millimeter regime and H_2 in the NIR (Gueth et al. 2001). The systemic velocity of the associated molecular emission is $-29\ \text{km s}^{-1}$, which implies a kinematic distance of $\sim 2.0\ \text{kpc}$ (Gueth et al. 2001). The large molecular outflow extends $\sim 2\ \text{pc}$ in the north–south direction with the CO blueshifted emission located toward the south and the redshifted toward the north, whereas the other smaller outflow is aligned toward the east–west direction with the CO blueshifted emission being more prominent toward the east and the redshifted toward the west. The P.A.’s of these two outflows differ by $\sim 65^{\circ}$ as estimated from Figure 3 of Gueth et al. (2001). Even though these authors do not explicitly give the P.A.’s of the two outflows, we have estimated a P.A. of $\sim 145^{\circ}$ and $\sim 80^{\circ}$ for the north–south and the east–west flows, respectively, from their Figure 3.

The confirmation of HH 288 having two independent outflows was later given by Franco-Hernández & Rodríguez (2003) as they revealed two centimeter sources associated with IRAS 00342+6347, called VLA 2a and VLA 2b. While they confirmed the association of VLA 2a with the north–south outflow, they could not unambiguously associate VLA 2b with the east–west outflow as this source was unresolved in their high-resolution ($\sim 0''.3$) VLA observations.

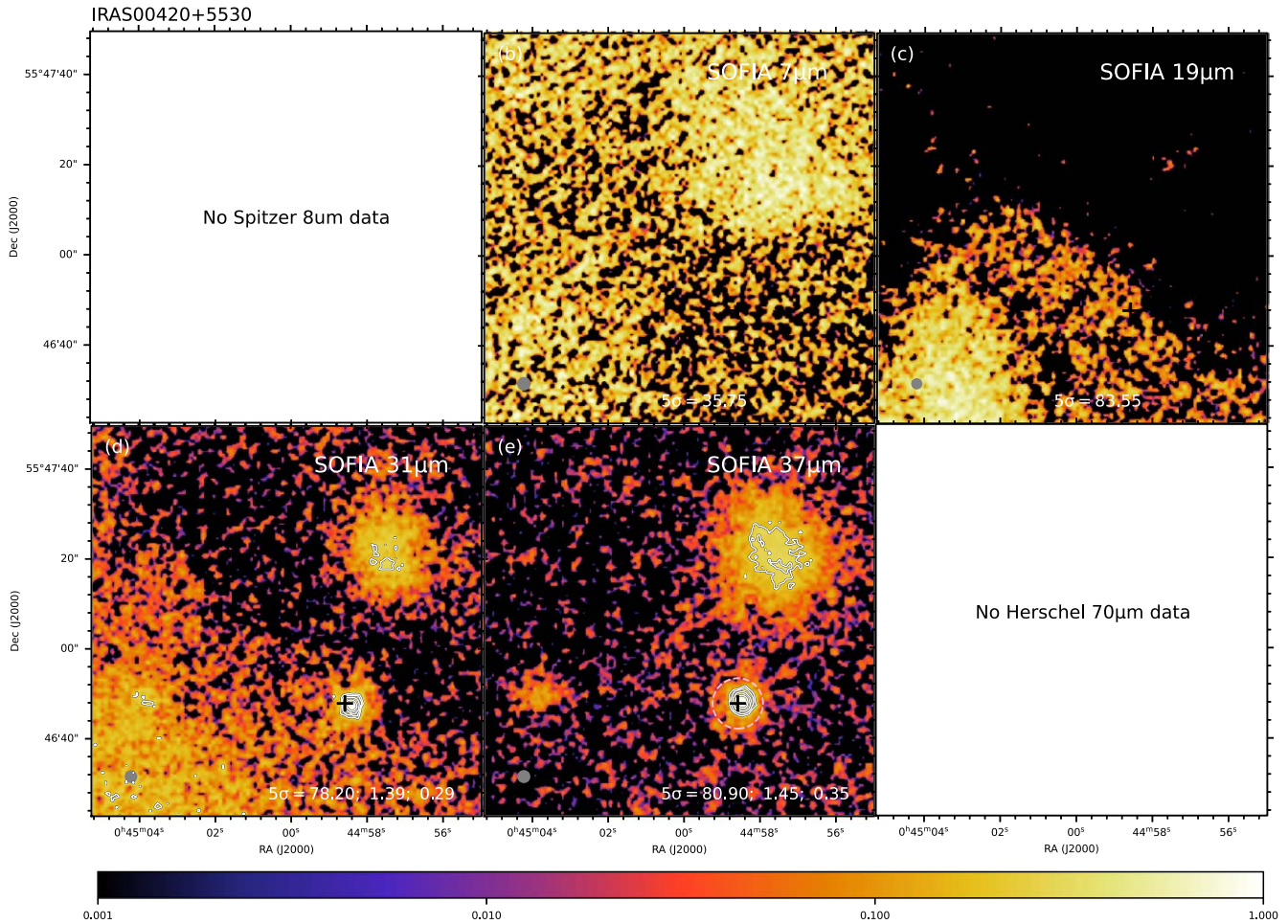


Figure 9. Multiwavelength images of IRAS 00420+5530, following the format of Figure 2. The black cross in all panels denotes the position of the 3.6 cm source VLA 3 from Molinari et al. (2002) at R.A. (J2000) = $0^{\text{h}}44^{\text{m}}58^{\text{s}}.5842$, decl. (J2000) = $+55^{\circ}46'45''.675$. The data used to create this figure and the SED are available. (The data used to create this figure are available.)

Figure 11 shows the multiwavelength images for HH 288. No Spitzer images are available for this region and SOFIA shorter wavelengths do not show significant emission. At 31 and 37 μm the central region shows some emission. We note that the extended 19 μm emission is likely due to the known window contamination problem that affected this observational data set.

4.2. Three-color Images

Figure 12 shows “RGB” images (i.e., based on 8, 19, and 37 μm MIR to FIR images) for the six regions analyzed in this paper that have the highest quality FORCAST imaging, i.e., AFGL 2591, G25.40-0.14, G30.59-0.04, G32.03+0.05, G33.92+0.11, and G40.62-0.14. These images allow for the inspection of color gradients in the regions. In particular, one prediction of TCA models is that near-facing outflow cavities will appear relatively brighter at shorter wavelengths. More generally, sources and regions of greater extinction will appear redder in these images. This is exactly what we see in the RGB images shown in Figure 12, redder colors toward the massive protostars with greater extinction and bluer color in the surroundings probably cleared by the outflow activity. In the case of AFGL 2591, the SW elongation is evident, suggesting the location of the near-facing outflow. More diffuse blue emission

is present in the G25.40-0.14 region with concentrated redder emission toward the center, whereas in the regions G30.59-0.04 and G40.62-0.14, less extended emission is revealed. It is interesting to note that in the case of the G32.03+0.05 region, the northern source appears redder than the southern one. This may indicate that the northern source is younger as it is more extincted and has not had enough time to clear the surroundings. Finally, G33.92+0.11 shows the arc-like shape at shorter wavelengths and more concentrated and redder emission toward the location of the massive protostar.

4.3. Results of SED Model Fitting

Here, we present the results of the measured fluxes and constructed SEDs of the 11 new sources analyzed in this paper, and their fits using the ZT18 model grid. In the Appendix, all SOMA sources published so far, i.e., from Papers I–III, are revisited with the new fitting pipeline.

4.3.1. Measured SEDs

For SOMA IV sources, we measure fluxes at 3.6, 4.5, 5.8, and 8.0 μm from Spitzer-IRAC images; 7.7, 19.1, 31.5, and 37.1 μm from SOFIA-FORCAST; and 70, 160, 250, 350, and 500 μm from Herschel-PACS/SPIRE. Not all fluxes were

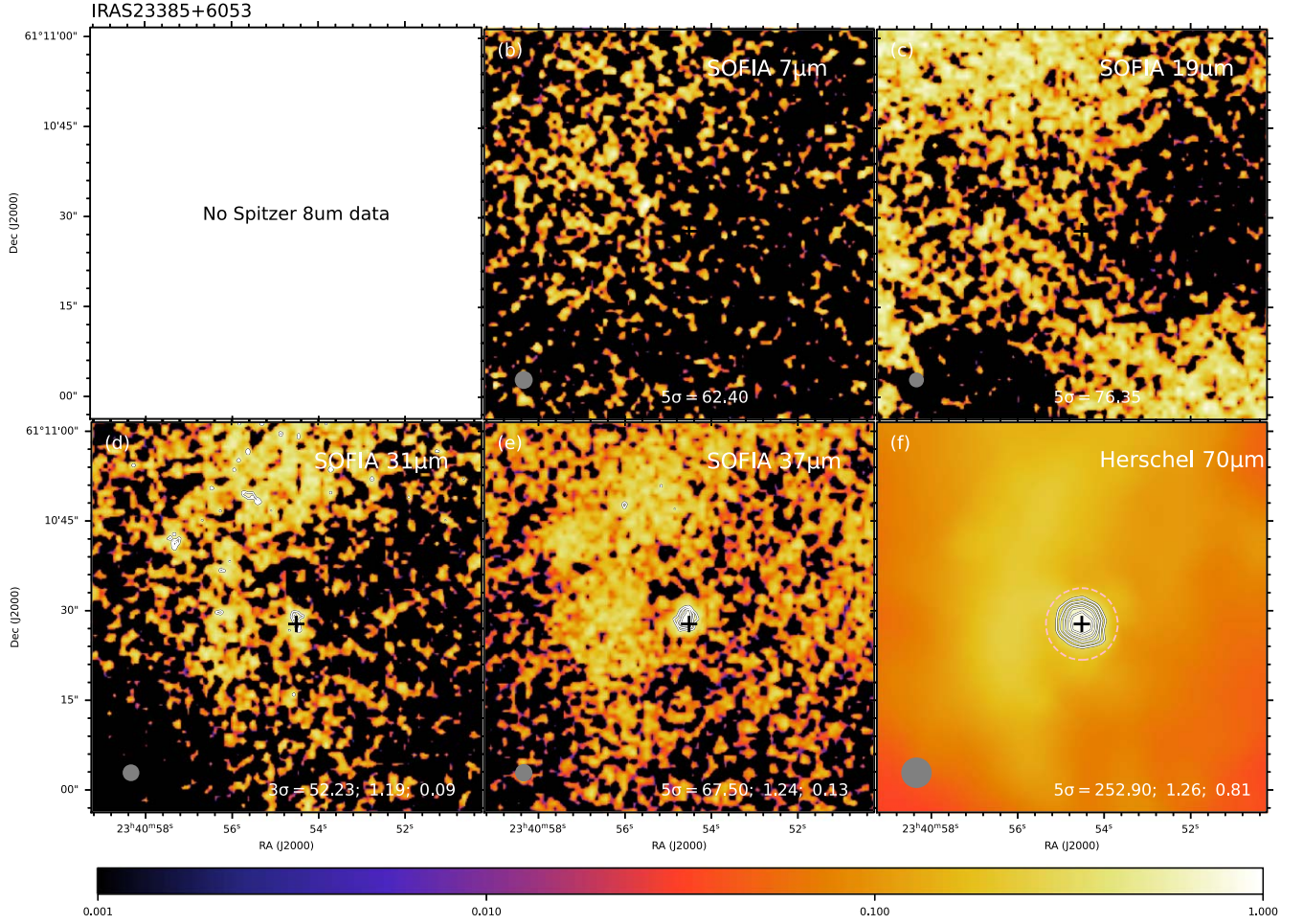


Figure 10. Multiwavelength images of IRAS 23385+6053, following the format of Figure 2. The black cross in all panels denotes the position of the 3.4 mm source Mol 160 from Molinari et al. (2002) at R.A. (J2000) = $23^{\text{h}}40^{\text{m}}54^{\text{s}}.5171$, decl. (J2000) = $+61^{\circ}10'27''.768$. The data used to create this figure and the SED are available.

(The data used to create this figure are available.)

measured for all sources due to either missing data or because the source was saturated at that wavelength. Additionally, when available, we measure the fluxes from IRAS-HIRES data to check for variability (Section 3.3). Note, these fluxes were not used to fit the SED model grid, partly because the sources are poorly resolved in the IRAS images, but also because the fitted SED is used to make a prediction of the IRAS flux for the variability analysis. Table 2 summarizes the measured fluxes in this study using the aperture radius indicated in the second column. As in the SOMA I–III, the fiducial method for measuring fluxes across all wavelengths is to set a fixed aperture for all images and perform background subtraction (this is what is reported throughout the paper). This aperture was chosen based on the Herschel 70 μm image or the SOFIA 37 μm when the former was not available (Section 3.1.1).

In Figure 13 we show the measured fluxes as red squares with their error bars. The error bars are set to be the larger of either 10% of the background-subtracted flux density or the value of the estimated background flux density. It should be recalled that everything at 8 μm and shorter wavelengths is treated as upper limits due to the RT models not including PAH emission and single photon transient heating effects on small dust grains (see De Buizer et al. 2017; ZT18). Most of the

sources show the complete set of Spitzer and Herschel data, with the latter constraining very well, together with SOFIA data, the peak of the SED. However, for sources IRAS 00420+5530 and IRAS 00259+5625, only 19.1, 31.5, and 37.1 μm images could be used to build their SEDs.

4.3.2. SED Model Fitting

Figure 13 shows all good (see Section 3.2.2) SED models with distinct values of M_c , Σ_{cl} , m_* , and θ_{view} that fit the SED data of each of the SOMA IV massive protostars. The properties of the best five of these models, along with the average and dispersion of all the good models, are shown in Table 3 (note, these averages are equally weighted over all good models, including with different viewing angles for the same physical model, but only counting one best value of A_V in each case). It should be noted that the errors used as weights in the evaluation of χ^2 may not have Gaussian distributions, so care should be taken in the interpretation of these numerical values.

Figure 14 presents the 2D distribution of the three main physical parameters of the model grid, i.e., in $\Sigma_{\text{cl}}-M_c$ space (left), m_*-M_c space (center) and $m_*-\Sigma_{\text{cl}}$ space (right), color coded by χ^2 (that of the best model at each location in the 2D

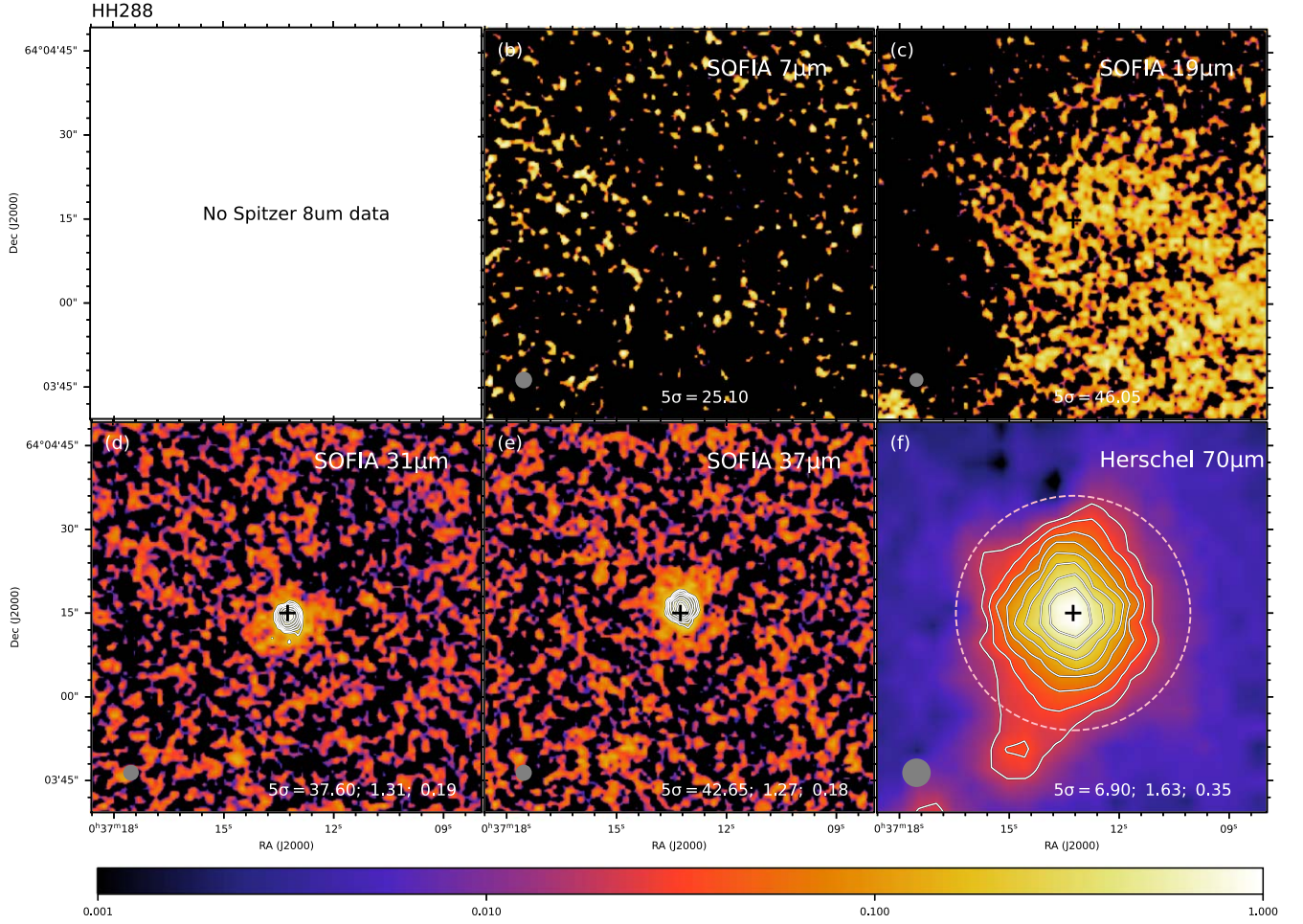


Figure 11. Multiwavelength images of HH 288, following the format of Figure 2. The black cross in all panels denotes the position of the 3.5 cm source 2a from Franco-Hernández & Rodríguez (2003) at R.A. (J2000) = $0^{\text{h}}37^{\text{m}}13^{\text{s}}.258$, decl. (J2000) = $+64^{\circ}04'15''.02$. The data used to create this figure and the SED are available. (The data used to create this figure are available.)

parameter space is shown). These plots help illustrate the extent of degeneracies that are present in the SED fitting.

In general, the observed SEDs are reasonably well fitted by the models and thus consistent with being massive protostars forming via TCA. In most cases, the best model for each source has $\chi^2_{\text{min}} \lesssim 1$, with the exceptions being AFGL 2591 (with $\chi^2_{\text{min}} = 1.7$), G25.40-0.14 (with $\chi^2_{\text{min}} = 3.2$), G32.03+0.05N (with $\chi^2_{\text{min}} = 1.6$), and G33.92+0.11 (with $\chi^2_{\text{min}} = 4.7$). These relatively poor fits are typically caused by discrepancies at the longest wavelengths indicating that there is additional relatively cold dusty material present around the protostar. This may result from imperfect clump background subtraction, especially if the adopted aperture radius is significantly larger than that of the model core. It should also be noted that values $\chi^2 < 1$ are either due to the small number of data points being fitted, and therefore the small degree of freedom, or the relatively large errors in the fluxes greater than $100 \mu\text{m}$.

Considering the average properties of the protostellar models, we see that initial core masses range from $M_c \sim 20$ to $\sim 400 M_{\odot}$, while clump mass surface densities range from $\Sigma_{\text{cl}} \sim 0.2\text{--}2 \text{ g cm}^{-2}$. The values of current protostellar mass range from $m_* \sim 2\text{--}40 M_{\odot}$.

We now describe the results of the SED fitting for each source in the following:

AFGL 2591: This source is the most massive protostar in SOMA IV with $m_* = 51^{+23}_{-16} M_{\odot}$ accreting at $6.9^{+9.3}_{-4.0} \times 10^{-4} M_{\odot} \text{ yr}^{-1}$ from a $313^{+159}_{-105} M_{\odot}$ core in a $\Sigma_{\text{cl}} = 0.699^{+1.879}_{-0.509} \text{ g cm}^{-2}$. This source has an average bolometric luminosity of $5.6^{+4.3}_{-2.4} \times 10^5 L_{\odot}$ being one of the most luminous sources in the SOMA survey to date. The SED fitting for this source predicts a highly extinguished region of $67 \pm 42 \text{ mag}$. This case has a viewing angle ($38^{\circ} \pm 16^{\circ}$) close to the cavity opening angle ($37^{\circ} \pm 8^{\circ}$), so that there are high levels of shorter wavelength emission as can be seen in both the observed and modeled SEDs.

G25.40-0.14: The predicted protostellar mass for this source is $42^{+30}_{-18} M_{\odot}$ making it the second most massive protostar in SOMA IV. It is forming in a core with mass $436^{+70}_{-61} M_{\odot}$ with a surface density $\Sigma_{\text{cl}} = 1.678^{+1.318}_{-0.738} \text{ g cm}^{-2}$, viewed at an angle $44^{\circ} \pm 13^{\circ}$. This source is also at the upper end of bolometric luminosity in our survey with $5.4^{+4.6}_{-2.5} \times 10^5 L_{\odot}$ and it is accreting material at high rates $1.5^{+0.4}_{-0.3} \times 10^{-3} M_{\odot} \text{ yr}^{-1}$. In this case, the predicted visual extinction is low and on average is 7 mag.

G30.59-0.04: This source is also among the most massive protostars in the SOMA sample with $m_* = 31^{+13}_{-9} M_{\odot}$ forming in a massive core of $M_c = 409^{+96}_{-78} M_{\odot}$ in a high-mass surface

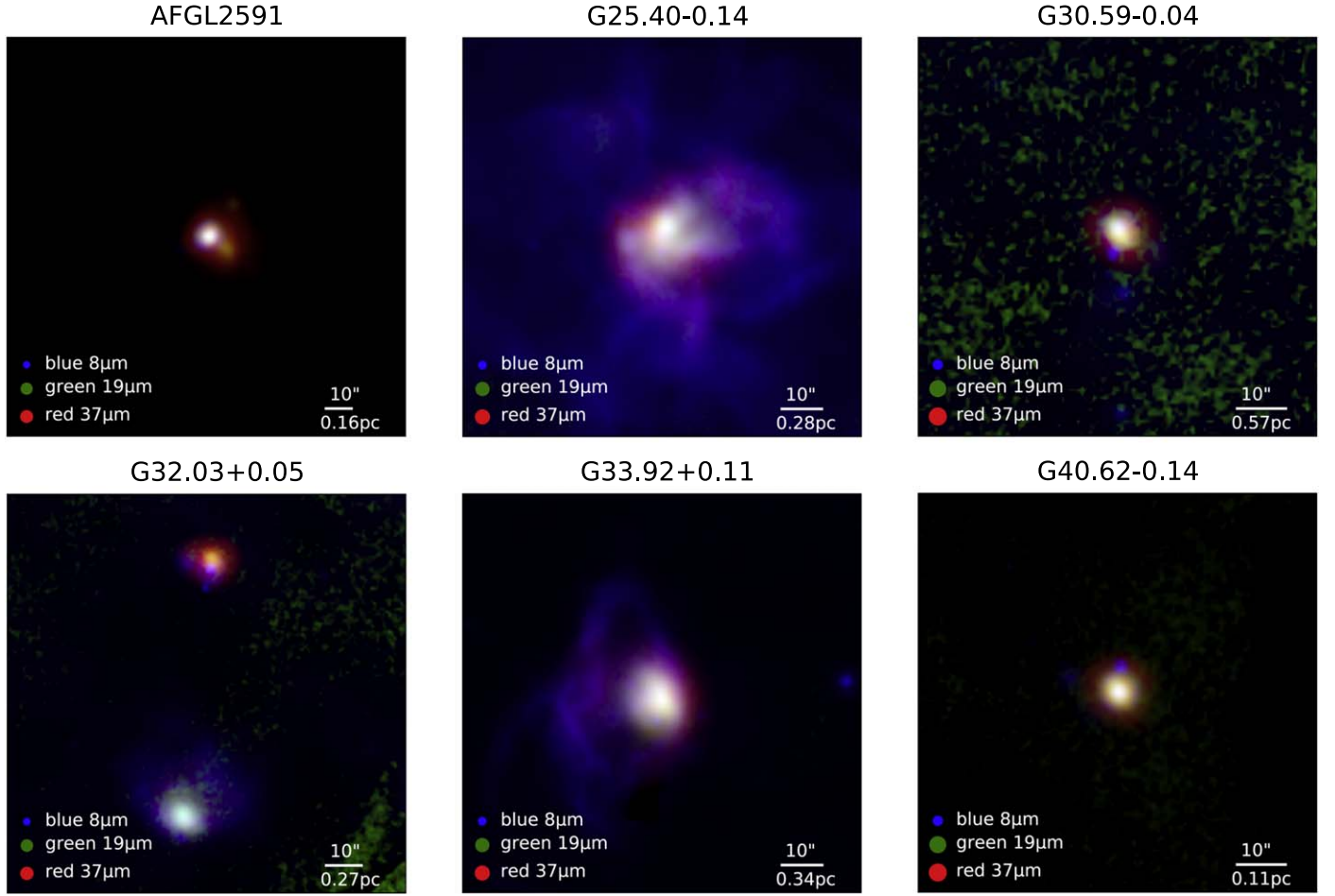


Figure 12. Gallery of RGB images of the six protostellar sources, as labeled. Red denotes SOFIA-FORCAST 37 μm , green denotes SOFIA-FORCAST 19 μm , and blue is Spitzer-IRAC 8 μm . The color intensity scales are stretched as arcsinh and show a dynamic range of 100 from the peak emission at each wavelength. The bottom-left corner shows the wavelengths used and the beam sizes. The rest of the sources, i.e., IRAS 00259+5625, IRAS 00420+5530, IRAS 23385+6053, and HH 288 are not shown due to the lack of Spitzer-IRAC 8 μm images and relatively poor signal-to-noise ratio (S/N) in the SOFIA images.

density clump of $\Sigma_{\text{cl}} = 1.584^{+1.204}_{-0.684} \text{ g cm}^{-2}$ accreting at high rates $1.2^{+0.5}_{-0.4} \times 10^{-3} M_{\odot} \text{ yr}^{-1}$. The SED fitting predicts a viewing angle of $63^{\circ} \pm 18^{\circ}$ and a narrow cavity opening angle of $19^{\circ} \pm 6^{\circ}$. This source also sits among the most luminous sources in our sample with $L_{\text{bol}} = 3.5^{+1.7}_{-1.1} \times 10^5 L_{\odot}$.

G32.03+0.05: This source continues with the trend of high-mass protostars with a predicted current mass of $m_{*} = 20^{+15}_{-8} M_{\odot}$ forming in a relatively high-mass core of $M_{\text{c}} = 148^{+139}_{-72} M_{\odot}$ but relatively low- Σ clump with $0.222^{+0.475}_{-0.151} \text{ g cm}^{-2}$, which implies it is accreting material at a relatively low rate of $1.4^{+1.3}_{-0.7} \times 10^{-4} M_{\odot} \text{ yr}^{-1}$. Its bolometric luminosity is $6.7^{+13.2}_{-4.4} \times 10^4 L_{\odot}$. The low value of Σ_{cl} implies it takes a relatively long time to form the protostar, i.e., the current stellar age (not shown in the main tables) for this source is $\sim 2 \times 10^5 \text{ yr}$, which is older than G32.03+0.05N (see below). The low value of Σ_{cl} also implies a low level of internal extinction, which is also reflected in its bluer IR colors.

G32.03+0.05N: This is the second source found in the G32.03+0.05 region and it is somewhat more massive ($31^{+36}_{-17} M_{\odot}$) forming in a higher mass core ($245^{+187}_{-106} M_{\odot}$) with a high-mass surface density clump ($0.465^{+1.063}_{-0.324} \text{ g cm}^{-2}$) and accreting material at a higher rate ($3.7^{+4.1}_{-1.9} \times 10^{-4} M_{\odot} \text{ yr}^{-1}$). This source is also more luminous ($2.1^{+5.2}_{-1.5} \times 10^5 L_{\odot}$) than the southern source present in the region. The SED-fitting outputs a current stellar age of $\sim 1.4 \times 10^5 \text{ yr}$, which is younger than

G32.03+0.05 (see above). Its higher Σ_{cl} implies higher internal extinction, which is reflected in its redder IR colors.

G33.92+0.11: The SED-fitting results of this source also involve a relatively massive core of $339^{+155}_{-106} M_{\odot}$ in density environment with $\Sigma_{\text{cl}} = 0.934^{+1.639}_{-0.595} \text{ g cm}^{-2}$ that harbors a current protostellar mass of $52^{+32}_{-20} M_{\odot}$. The protostar is accreting at high rates $9.0^{+7.6}_{-4.1} \times 10^{-3} M_{\odot} \text{ yr}^{-1}$ with a narrow cavity opening angle of $35^{\circ} \pm 11^{\circ}$ and viewed at $54^{\circ} \pm 17^{\circ}$. This source also is among the most luminous sources with $L_{\text{bol}} = 6.3^{+5.2}_{-2.8} \times 10^5 L_{\odot}$.

G40.62-0.14: This source is still in the high-mass regime with $m_{*} = 15^{+8}_{-5} M_{\odot}$, but forming in a relatively low-mass core of $64^{+34}_{-22} M_{\odot}$ and also low-mass surface density clump of $\Sigma_{\text{cl}} = 0.615^{+1.011}_{-0.382} \text{ g cm}^{-2}$. It is accreting material at rates of $2.1^{+1.9}_{-1.0} \times 10^{-4} M_{\odot} \text{ yr}^{-1}$ and has a bolometric luminosity of $4.9^{+7.0}_{-2.9} \times 10^4 L_{\odot}$.

IRAS 00259+5625: Note that for this source, which lacks Spitzer and Herschel data, there are only three effective data points constraining the models. The values of χ^2 are small, i.e., about 0.01, for the best-fit case. When considering the good models, they indicate $3^{+6}_{-2} M_{\odot}$ protostars in relatively low- Σ cores $0.517^{+1.012}_{-0.342} \text{ g cm}^{-2}$ with low masses of $45^{+57}_{-25} M_{\odot}$ viewed at $55^{\circ} \pm 22^{\circ}$. It is accreting at low rates of $8.6^{+15.0}_{-5.4} \times 10^{-5} M_{\odot} \text{ yr}^{-1}$. This source represents one of smaller

Table 2
Integrated Flux Densities

Source	radius (''/pc)	$F_{3.6}$ (Jy)	$F_{4.5}$ (Jy)	$F_{5.8}$ (Jy)	$F_{7.7}$ (Jy)	$F_{8.0}$ (Jy)	F_{12} (Jy)	$F_{19.1}$ (Jy)	F_{25} (Jy)	$F_{31.5}$ (Jy)	$F_{37.1}$ (Jy)	F_{60} (Jy)	F_{70} (Jy)	F_{100} (Jy)	F_{160} (Jy)	F_{250} (Jy)	F_{350} (Jy)	F_{500} (Jy)
AFGL 2591	18.75	74.45	173.42	342.88	...	308.61	522.29	681.70	1486.42	2437.74	3196.32	6988.93	4445.46	7132.77	2172.18	535.94	151.56	25.50
	0.30	(74.83)	(174.28)	(348.25)	...	(313.06)	...	(679.86)	...	(2463.83)	(3223.91)	...	(4618.42)	...	(2416.41)	(660.42)	(201.93)	(45.07)
		[10.53]	[24.53]	[48.50]	...	[43.65]	...	[96.43]	...	[344.94]	[452.75]	...	[632.37]	...	[392.45]	[145.74]	[54.74]	[19.90]
G25.40-0.14	48.5	87.83	...	58.36	155.98	618.83	1641.73	2513.93	5244.28	5549.39	10150.80	3535.18	1146.80	405.21	115.15
	1.34	(84.73)	(202.50)	...	(1447.83)	(2000.58)	...	(6383.78)	...	(4498.69)	(1739.51)	(650.73)	(206.07)
		[20.41]	[50.81]	...	[289.94]	[380.30]	...	[834.98]	...	[1085.50]	[614.49]	[252.12]	[92.37]
G30.59-0.04	13.5	1.68	3.39	2.13	1.12	3.57	16.02	113.51	182.21	631.11	875.04	863.71	616.98	170.58	43.76	3.32
	0.77	(2.28)	(2.87)	(4.22)	...	(5.46)	...	(114.10)	(182.64)	...	(932.24)	...	(798.99)	(277.49)	(93.98)	(23.59)
		[0.24]	[0.78]	[0.30]	...	[1.30]	...	[16.10]	[25.77]	...	[124.64]	...	[201.84]	[109.60]	[50.60]	[20.28]
G32.03+0.05	22.75	0.32	...	2.43	8.10	12.38	...	69.87	114.25	...	171.12	...	129.50	62.29	23.75	8.91
	0.61	(0.42)	...	(3.04)	(4.89)	(5.43)	...	(79.01)	(103.49)	...	(184.66)	...	(203.10)	(145.75)	(73.65)	(28.54)
		[0.06]	...	[0.36]	[2.35]	[4.55]	...	[11.50]	[16.44]	...	[26.46]	...	[75.84]	[83.93]	[50.01]	[19.66]
G32.03+0.05N	13.5	0.09	...	1.31	2.23	1.76	...	65.35	105.86	...	543.84	...	600.94	...	61.97	11.06
	0.36	(0.13)	...	(1.60)	(1.92)	(67.69)	(103.36)	...	(567.51)	...	(716.45)	...	(107.73)	(26.67)
		[0.02]	...	[0.19]	[0.90]	[0.92]	...	[9.93]	[15.65]	...	[77.79]	...	[143.41]	...	[46.60]	[15.70]
G33.92+0.11	25.25	0.78	22.56	17.71	35.29	138.75	340.07	542.56	699.50	2089.71	1723.21	2612.35	1612.85	...	217.43	51.50
	0.87	(0.90)	(17.00)	(21.33)	...	(128.00)	...	(535.73)	(709.91)	...	(1784.91)	...	(1862.11)	...	(301.87)	(85.89)
		[0.40]	[4.39]	[2.65]	...	[20.78]	...	[76.91]	[99.33]	...	[249.72]	...	[337.87]	...	[89.87]	[35.15]
G40.62-0.14	13.5	0.09	2.47	1.81	1.69	15.81	84.14	182.25	269.50	800.55	694.32	1110.80	417.82	125.57	26.85	4.20
	0.14	(0.12)	(1.97)	(2.32)	...	(19.42)	...	(189.54)	(273.43)	...	(716.24)	...	(487.06)	(171.61)	(56.62)	(13.59)
		[0.03]	[0.38]	[0.26]	...	[2.51]	...	[25.82]	[38.11]	...	[98.60]	...	[91.02]	[49.35]	[30.01]	[9.41]
IRAS 00259	7.0	0.33	0.18	0.57	1.51	2.21	25.34	...	100.53
	0.08	(0.92)	...	(1.77)	(0.85)
		[0.51]	...	[0.45]	[0.45]
IRAS 00420	7.0	5.23	0.45	11.43	5.81	8.09	188.40	...	218.18
	0.07	(0.20)	...	(6.69)	(8.01)
		[0.61]	...	[1.02]	[1.28]
IRAS 23385	5.75	0.10	0.96	1.78	...	22.38	...	37.96	22.82	2.89	0.75
	0.14	(0.80)	(2.57)	...	(34.68)	...	(57.99)	(42.11)	(14.31)	(5.17)
		[0.34]	[0.44]	[0.55]	...	[4.17]	...	[20.73]	[19.56]	[11.43]	[4.43]
HH 288	7.5	0.02	0.23	0.89	3.84	4.33	30.41	27.20	104.26	37.57	6.88	1.52	0.05
	0.07	(0.38)	...	(5.84)	(4.63)	...	(30.40)	...	(48.53)	(17.45)	(6.32)	(1.50)
		[0.18]	...	[0.58]	[0.64]	...	[3.90]	...	[12.18]	[10.61]	[4.80]	[1.44]

Note. $F_{3.6}$, $F_{4.5}$, $F_{5.8}$, and $F_{8.0}$ refer to fluxes from Spitzer-IRAC at 3.6, 4.5, 5.8, and 8.0 μm , respectively. $F_{7.7}$, $F_{19.1}$, $F_{31.5}$, and $F_{37.1}$ refer to fluxes from SOFIA-FORCAST at 7.7, 19.1, 31.5, and 37.5 μm , respectively. F_{70} , F_{160} , F_{250} , F_{350} , and F_{500} refer to fluxes from Herschel-PACS/SPIRE at 70, 160, 250, 350, and 500 μm , respectively. $F_{12.0}$, $F_{25.0}$, $F_{60.0}$, and $F_{100.0}$ refer to fluxes from IRAS-HIRES at 12.0, 25.0, 60.0, and 100.0 μm , respectively. The three dots refer to either data not found or saturated at that wavelength. The first row for each source refers to background-subtracted flux. The second row for each source with fluxes in parenthesis refers to non-background-subtracted flux (in many FORCAST 7.7 μm images we find that the estimated background has a slightly negative value, which results from a calibration offset problem; hence, background-subtracted values appear larger in this table; however, we still expect these background-subtracted values to be accurate). The third row for each source with square brackets refers to the associated error to the background-subtracted fluxes. †No Herschel-PACS 70 μm data is available and SOFIA-FORCAST 37 μm was used to find the optimal aperture (Section 3.1.1). For the radius column for each source, the first row refers to arcminutes and the second row to parsecs.

(This table is available in machine-readable form.)

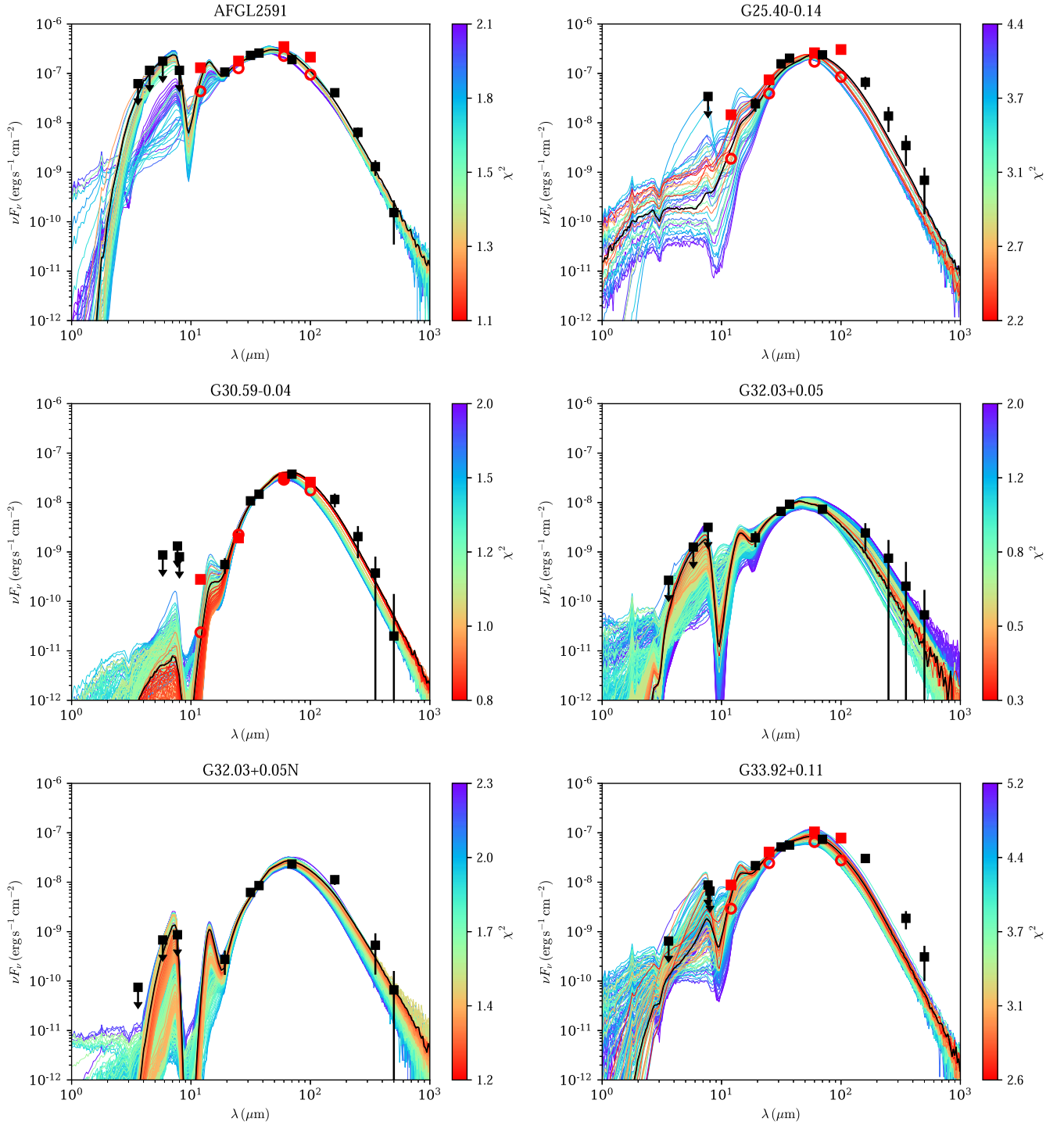


Figure 13. Protostellar SEDs with fluxes evaluated via the fixed aperture method and shown after background subtraction for each source noted on top of each plot. Flux values are those from Table 2 and are represented as black squares. Solid black squares are used in the model fitting, while red squares (i.e., IRAS fluxes) are not. Note that the data at $\lesssim 8 \mu\text{m}$ are treated as upper limits for SED model fitting (see the text). The best-fitting protostar model is shown with a black line, while all other good model fits (see the text) are shown with colored lines (red to blue with increasing χ^2). Red empty circles denote the geometric mean prediction for good models at IRAS wavelengths to test for source variability (see the text).

bolometric luminosity ($L_{\text{bol}} = 2.5^{+12.5}_{-2.0} \times 10^3 L_{\odot}$) in the SOMA IV sample. Longer-wavelength data would obviously be helpful here to break some of these degeneracies.

IRAS 00420+5530: Note that also for this source, which also lacks Spitzer and Herschel data, there are only three effective data points constraining the models. The values of χ^2 are small, i.e., about 0.33, for the best-fit case. When considering the good models, they indicate $3^{+3}_{-2} M_{\odot}$ protostars in Σ

cores $0.365^{+0.619}_{-0.230} \text{ g cm}^{-2}$ viewed at $49^{\circ} \pm 23^{\circ}$ and accreting at low rates $6.1^{+5.5}_{-2.9} \times 10^{-5} M_{\odot} \text{ yr}^{-1}$. This source is on the lower end of bolometric luminosities with $1.5^{+3.5}_{-1.0} \times 10^3 L_{\odot}$ framing it into the intermediate-mass protostars. Longer-wavelength data would obviously be helpful here to break some of these degeneracies.

IRAS 23385: The SED fitting for this source predicts $m_* = 5^{+10}_{-3} M_{\odot}$ forming from a core of $52^{+54}_{-26} M_{\odot}$ at relatively

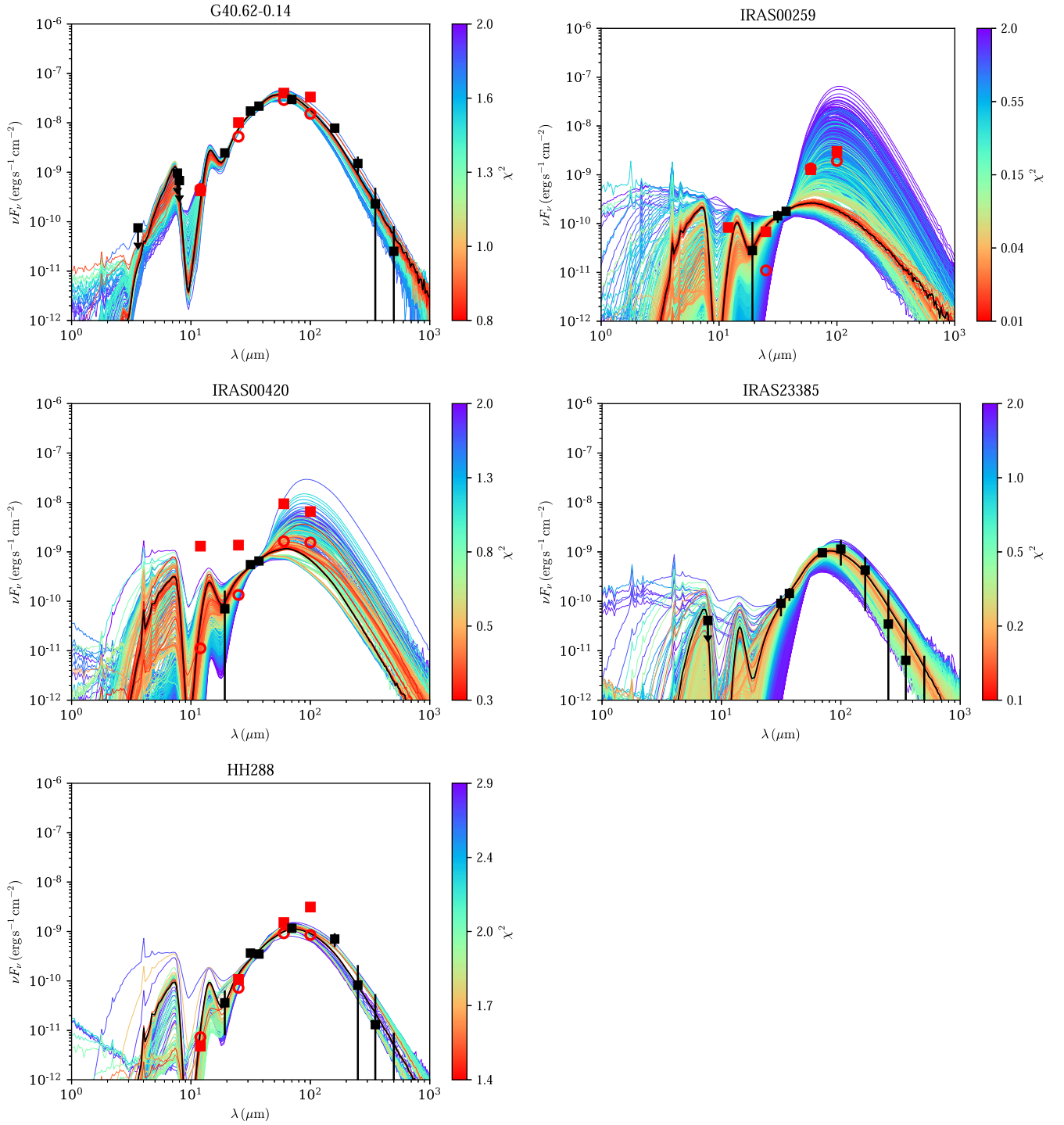


Figure 13. (Continued.)

low- Σ clump $0.517^{+1.067}_{-0.384} \text{ g cm}^{-2}$ and accreting material at a rate of $1.1^{+1.1}_{-0.5} \times 10^{-4} M_{\odot} \text{ yr}^{-1}$. Its luminosity is $L_{\text{bol}} = 5.6^{+27.4}_{-4.7} \times 10^3 L_{\odot}$ and it is on the edge of being considered a massive protostar given the current protostellar mass. However, it should be noted that good models cover a large range of parameter space, i.e., source properties are not well constrained by the current data.

HH 288: The SED fitting for this source predicts a current protostellar mass that is in the intermediate-mass regime with $m_* = 3^{+3}_{-1} M_{\odot}$, forming from a core of initial mass $18^{+9}_{-6} M_{\odot}$

within a clump of mass surface density of $0.449^{+1.046}_{-0.314} \text{ g cm}^{-2}$. This source is also accreting at low rates ($5.5^{+5.9}_{-2.8} \times 10^{-5} M_{\odot} \text{ yr}^{-1}$) and has the lowest bolometric luminosity ($1.1^{+1.7}_{-0.7} \times 10^3 L_{\odot}$) in the SOMA IV sample.

As has been noted in previous SOMA papers, MIR to FIR SED fitting can be subject to significant degeneracies. Follow-up analysis of source MIR and FIR images (e.g., Zhang et al. 2013b), centimeter continuum emission from ionized gas (e.g., Rosero et al. 2019a) and protostellar outflow properties are some of the methods that can be used to help break such degeneracies.

Table 3
Parameters of the Best Five Fitted Models and Average and Dispersion of Good Models

Source	χ^2	M_c (M_\odot)	Σ_{cl} (g cm^{-2})	R_{core} (pc)	m_* (M_\odot)	θ_{view} ($^\circ$)	A_V (mag)	M_{env} (M_\odot)	$\theta_{w,esc}$ (deg)	\dot{M}_{disk} (M_\odot/yr)	$L_{bol,iso}$ (L_\odot)	L_{bol} (L_\odot)
AFGL 2591	1.06	480	0.316	0.29	32	13	76	405.71	22	3.9×10^{-4}	1.3×10^6	2.0×10^5
$d = 3.3$ kpc	1.24	400	0.316	0.26	48	29	86	272.62	34	4.1×10^{-4}	1.5×10^6	4.1×10^5
$R_{ap} = 18''75$	1.25	400	0.316	0.26	32	13	69	317.05	25	3.6×10^{-4}	1.2×10^6	2.0×10^5
$R_{ap} = 0.30$ pc	1.41	400	0.316	0.26	64	39	91	222.98	42	4.3×10^{-4}	1.4×10^6	6.6×10^5
	1.52	160	3.160	0.05	24	22	90	114.57	23	1.4×10^{-3}	1.3×10^6	3.0×10^5
Average model	#74	313^{+159}_{-105}	$0.699^{+1.879}_{-0.509}$	$0.16^{+0.21}_{-0.09}$	51^{+23}_{-16}	38 ± 16	67 ± 42	178^{+110}_{-68}	37 ± 8	$6.9^{+9.3}_{-4.0} \times 10^{-4}$	$7.0^{+16.8}_{-4.9} \times 10^5$	$5.6^{+4.3}_{-2.4} \times 10^5$
G25.40-0.14	2.24	480	3.160	0.09	24	22	0	440.54	12	2.0×10^{-3}	2.9×10^5	2.9×10^5
$d = 5.7$ kpc	2.27	480	1.000	0.16	64	48	0	324.63	32	1.2×10^{-3}	2.8×10^5	8.4×10^5
$R_{ap} = 48''50$	2.28	400	3.160	0.08	24	22	1	361.65	13	1.9×10^{-3}	3.0×10^5	3.0×10^5
$R_{ap} = 1.34$ pc	2.44	480	1.000	0.16	48	34	7	366.96	25	1.1×10^{-3}	3.0×10^5	5.4×10^5
	2.92	320	3.160	0.07	24	29	0	276.82	15	1.8×10^{-3}	2.7×10^5	3.1×10^5
Average model	#40	436^{+70}_{-61}	$1.678^{+1.318}_{-0.738}$	$0.12^{+0.05}_{-0.03}$	42^{+30}_{-18}	44 ± 13	7 ± 17	324^{+67}_{-55}	24 ± 11	$1.5^{+0.4}_{-0.3} \times 10^{-3}$	$2.7^{+0.6}_{-0.5} \times 10^5$	$5.4^{+4.6}_{-2.5} \times 10^5$
G30.59-0.04	0.75	480	3.160	0.09	24	29	81	440.54	12	2.0×10^{-3}	2.7×10^5	2.9×10^5
$d = 11.8$ kpc	0.77	400	3.160	0.08	24	39	80	361.65	13	1.9×10^{-3}	2.6×10^5	3.0×10^5
$R_{ap} = 13''50$	0.99	320	3.160	0.07	24	71	57	276.82	15	1.8×10^{-3}	2.1×10^5	3.1×10^5
$R_{ap} = 0.77$ pc	1.07	480	1.000	0.16	24	34	3	433.43	15	8.2×10^{-4}	1.7×10^5	2.1×10^5
	1.08	480	1.000	0.16	32	39	36	414.30	19	9.3×10^{-4}	2.0×10^5	3.0×10^5
Average model	#180	409^{+96}_{-78}	$1.584^{+1.204}_{-0.684}$	$0.12^{+0.05}_{-0.04}$	31^{+13}_{-9}	63 ± 18	45 ± 32	338^{+91}_{-71}	19 ± 6	$1.2^{+0.5}_{-0.4} \times 10^{-3}$	$2.0^{+0.4}_{-0.4} \times 10^5$	$3.5^{+1.7}_{-1.1} \times 10^5$
G32.03+0.05	0.28	400	0.100	0.47	96	86	103	45.80	76	8.3×10^{-5}	3.9×10^4	1.2×10^6
$d = 5.5$ kpc	0.36	160	0.100	0.29	24	51	71	86.57	45	8.5×10^{-5}	2.8×10^4	7.8×10^4
$R_{ap} = 22''75$	0.56	240	0.100	0.36	12	29	21	210.90	19	8.5×10^{-5}	1.7×10^4	2.0×10^4
$R_{ap} = 0.61$ pc	0.56	160	0.100	0.29	16	62	21	115.88	32	8.1×10^{-5}	1.5×10^4	3.3×10^4
	0.57	200	0.100	0.33	12	62	1	174.14	20	8.0×10^{-5}	1.3×10^4	2.0×10^4
Average model	#398	148^{+139}_{-72}	$0.222^{+0.475}_{-0.151}$	$0.19^{+0.27}_{-0.11}$	20^{+15}_{-8}	62 ± 18	52 ± 60	73^{+128}_{-46}	39 ± 17	$1.4^{+1.3}_{-0.7} \times 10^{-4}$	$2.6^{+5.3}_{-1.7} \times 10^4$	$6.7^{+13.2}_{-4.4} \times 10^4$
G32.03+0.05N	1.17	480	0.100	0.51	32	29	251	390.89	26	1.6×10^{-4}	1.5×10^5	1.6×10^5
$d = 5.5$ kpc	1.30	400	0.100	0.47	32	34	230	304.06	29	1.5×10^{-4}	1.1×10^5	1.6×10^5
$R_{ap} = 13''50$	1.33	400	0.100	0.47	48	44	272	248.45	39	1.6×10^{-4}	1.8×10^5	3.6×10^5
$R_{ap} = 0.36$ pc	1.37	320	0.316	0.23	12	22	78	293.02	13	2.2×10^{-4}	3.6×10^4	4.0×10^4
	1.45	480	0.316	0.29	128	22	367	91.15	67	3.8×10^{-4}	4.9×10^6	2.0×10^6
Average model	#848	245^{+187}_{-106}	$0.465^{+1.063}_{-0.324}$	$0.17^{+0.22}_{-0.10}$	31^{+36}_{-17}	60 ± 20	174 ± 103	137^{+128}_{-66}	35 ± 16	$3.7^{+4.1}_{-1.9} \times 10^{-4}$	$9.4^{+28.6}_{-7.1} \times 10^4$	$2.1^{+5.2}_{-1.5} \times 10^5$
G33.92+0.11	2.60	200	3.160	0.06	24	29	46	155.51	20	1.5×10^{-3}	2.6×10^5	3.1×10^5
$d = 7.1$ kpc	2.62	240	3.160	0.06	32	29	92	175.32	23	1.9×10^{-3}	4.5×10^5	5.0×10^5
$R_{ap} = 25''25$	2.62	320	1.000	0.13	32	29	17	252.35	24	8.2×10^{-4}	2.0×10^5	2.7×10^5
$R_{ap} = 0.87$ pc	2.76	200	3.160	0.06	32	34	58	140.13	25	1.7×10^{-3}	2.8×10^5	4.6×10^5
	2.88	240	3.160	0.06	48	39	76	138.07	33	2.1×10^{-3}	3.6×10^5	7.5×10^5
Average model	#154	339^{+155}_{-106}	$0.934^{+1.639}_{-0.595}$	$0.14^{+0.14}_{-0.07}$	52^{+32}_{-20}	54 ± 17	21 ± 26	200^{+96}_{-65}	35 ± 11	$9.0^{+7.6}_{-4.1} \times 10^{-4}$	$2.0^{+0.7}_{-0.5} \times 10^5$	$6.3^{+5.2}_{-2.8} \times 10^5$
G40.62-0.14	0.83	80	0.316	0.12	16	51	89	41.63	42	1.5×10^{-4}	1.2×10^4	4.2×10^4
$d = 2.2$ kpc	0.90	100	0.316	0.13	24	68	85	35.52	54	1.5×10^{-4}	1.1×10^4	8.8×10^4
$R_{ap} = 13''50$	0.91	100	0.316	0.13	8	29	12	83.08	20	1.3×10^{-4}	7.5×10^3	1.0×10^4
$R_{ap} = 0.14$ pc	1.35	60	0.316	0.10	8	55	0	43.41	28	1.1×10^{-4}	5.8×10^3	1.2×10^4
	1.37	50	1.000	0.05	16	62	60	16.19	48	2.8×10^{-4}	9.2×10^3	6.7×10^4
Average model	#142	64^{+34}_{-22}	$0.615^{+1.011}_{-0.382}$	$0.08^{+0.07}_{-0.04}$	15^{+8}_{-5}	69 ± 14	59 ± 39	24^{+27}_{-13}	44 ± 11	$2.1^{+1.9}_{-1.0} \times 10^{-4}$	$9.2^{+3.5}_{-2.5} \times 10^3$	$4.9^{+7.0}_{-2.9} \times 10^4$

Table 3
(Continued)

Source	χ^2	M_c (M_\odot)	Σ_{cl} (g cm^{-2})	R_{core} (pc)	m_* (M_\odot)	θ_{view} ($^\circ$)	A_V (mag)	M_{env} (M_\odot)	$\theta_{w,esc}$ (deg)	\dot{M}_{disk} (M_\odot/yr)	$L_{bol,iso}$ (L_\odot)	L_{bol} (L_\odot)
IRAS 00259	0.01	30	0.316	0.07	12	39	169	0.76	81	2.2×10^{-5}	2.2×10^4	1.2×10^4
$d = 2.5$ kpc	0.02	20	0.100	0.10	1	29	49	17.28	20	1.3×10^{-5}	1.2×10^2	1.5×10^2
$R_{ap} = 7''00$	0.03	40	0.100	0.15	12	13	162	2.10	82	9.5×10^{-6}	2.1×10^4	1.1×10^4
$R_{ap} = 0.08$ pc	0.03	20	0.100	0.10	2	48	35	14.56	30	1.7×10^{-5}	1.1×10^2	1.9×10^2
	0.03	20	0.100	0.10	0	22	0	18.84	13	9.6×10^{-6}	8.6×10^1	9.0×10^1
Average model	#2427	45^{+57}_{-25}	$0.517^{+0.012}_{-0.342}$	$0.07^{+0.07}_{-0.03}$	3^{+6}_{-2}	55 ± 22	230 ± 206	25^{+65}_{-18}	27 ± 20	$8.6^{+15.0}_{-5.4} \times 10^{-5}$	$1.7^{+9.4}_{-1.5} \times 10^3$	$2.5^{+12.5}_{-2.0} \times 10^3$
IRAS 00420	0.33	10	3.160	0.01	4	51	160	1.65	56	1.9×10^{-4}	1.9×10^3	1.9×10^3
$d = 2.2$ kpc	0.33	10	3.160	0.01	0	13	170	9.05	14	1.1×10^{-4}	6.8×10^3	9.1×10^2
$R_{ap} = 7''00$	0.35	10	1.000	0.02	2	22	153	5.33	39	7.5×10^{-5}	3.2×10^3	7.6×10^2
$R_{ap} = 0.07$ pc	0.35	20	0.316	0.06	1	22	10	17.54	18	3.2×10^{-5}	3.3×10^2	3.9×10^2
	0.40	30	0.100	0.13	4	51	80	20.50	33	2.7×10^{-5}	4.1×10^2	7.7×10^2
Average model	#429	32^{+31}_{-16}	$0.365^{+0.619}_{-0.230}$	$0.07^{+0.07}_{-0.03}$	3^{+3}_{-2}	49 ± 23	103 ± 92	17^{+38}_{-12}	32 ± 18	$6.1^{+5.5}_{-2.9} \times 10^{-5}$	$1.2^{+3.2}_{-0.9} \times 10^3$	$1.5^{+3.5}_{-1.0} \times 10^3$
IRAS 23385	0.11	30	1.000	0.04	2	13	294	25.89	19	1.2×10^{-4}	1.3×10^4	1.7×10^3
$d = 4.9$ kpc	0.14	30	1.000	0.04	1	13	145	27.97	12	8.4×10^{-5}	5.1×10^3	1.0×10^3
$R_{ap} = 5''75$	0.15	40	1.000	0.05	4	22	297	31.54	23	1.7×10^{-4}	8.3×10^3	2.2×10^3
$R_{ap} = 0.14$ pc	0.18	20	3.160	0.02	4	13	347	11.60	34	3.1×10^{-4}	1.9×10^4	3.3×10^3
	0.20	40	1.000	0.05	1	13	95	38.55	10	9.1×10^{-5}	3.6×10^3	1.0×10^3
Average model	#1692	52^{+54}_{-26}	$0.517^{+1.067}_{-0.348}$	$0.07^{+0.10}_{-0.04}$	5^{+10}_{-3}	57 ± 22	265 ± 255	26^{+52}_{-17}	32 ± 20	$1.1^{+1.1}_{-0.5} \times 10^{-4}$	$3.5^{+16.9}_{-2.9} \times 10^3$	$5.6^{+27.4}_{-4.7} \times 10^3$
HH 288	1.44	10	1.000	0.02	2	39	183	5.33	39	7.5×10^{-5}	1.0×10^3	7.6×10^2
$d = 2.0$ kpc	1.53	20	0.316	0.06	2	29	149	15.05	27	4.2×10^{-5}	7.3×10^2	4.8×10^2
$R_{ap} = 7''50$	1.74	20	0.316	0.06	0	13	86	19.17	11	2.3×10^{-5}	8.3×10^2	2.0×10^2
$R_{ap} = 0.07$ pc	1.80	10	3.160	0.01	4	65	69	1.65	56	1.9×10^{-4}	2.4×10^2	1.9×10^3
	1.96	20	0.316	0.06	1	13	226	17.54	18	3.2×10^{-5}	2.7×10^3	3.9×10^2
Average model	#92	18^{+9}_{-6}	$0.449^{+1.046}_{-0.314}$	$0.05^{+0.06}_{-0.03}$	3^{+3}_{-1}	52 ± 23	148 ± 99	7^{+13}_{-5}	40 ± 15	$5.5^{+5.9}_{-2.8} \times 10^{-5}$	$6.6^{+14.6}_{-4.6} \times 10^2$	$1.1^{+1.7}_{-0.7} \times 10^3$

Note. For each source, the first five rows refer to the best five models taken from the 432 physical models, whereas the sixth row shows the average and dispersion of good model fits (see the text). The number next to the symbol # represents the number of models considered in the average of the good models. Upper and lower scripts in the row average models refer to the upper and lower errors.

(This table is available in machine-readable form.)

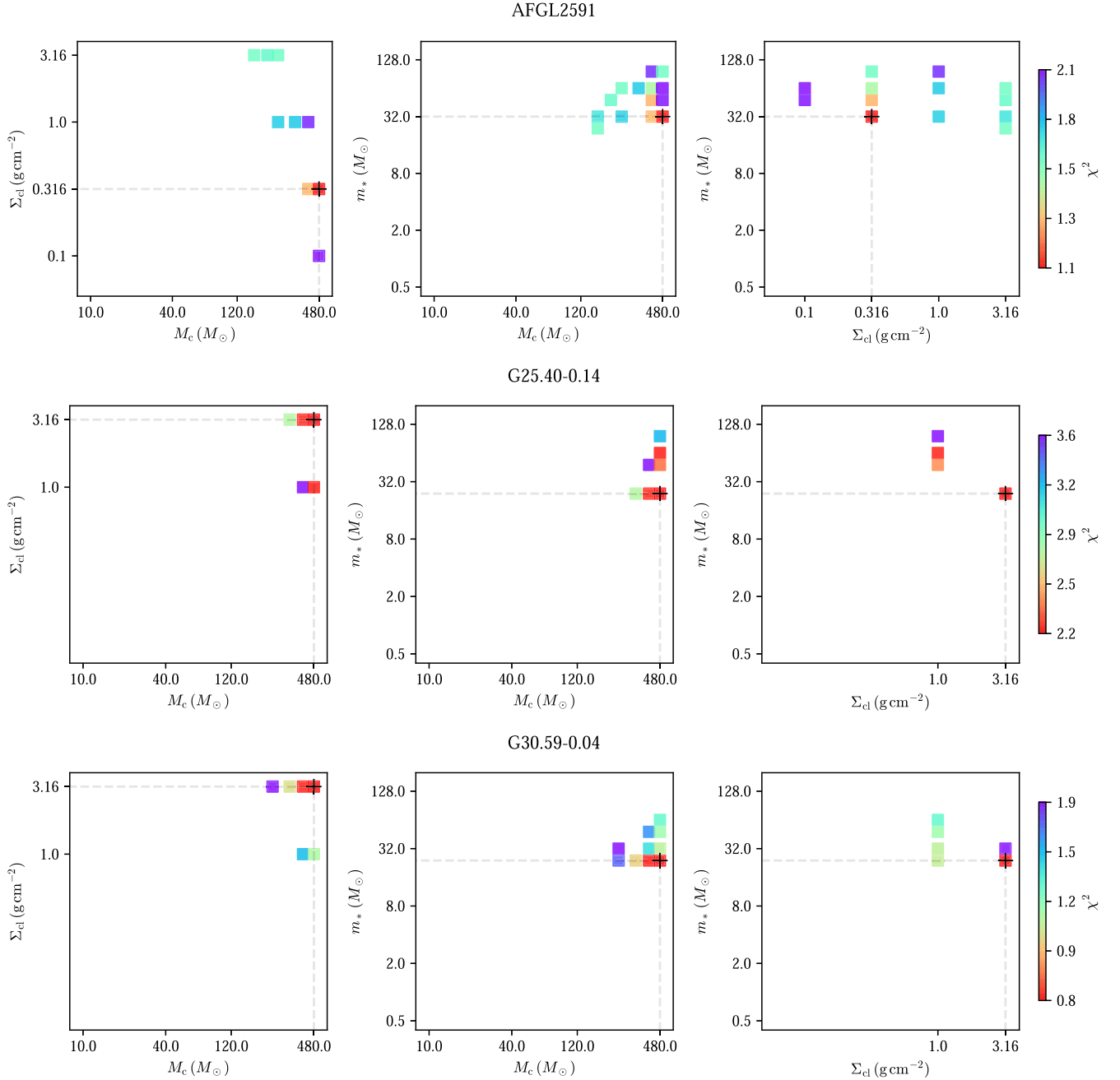


Figure 14. Diagrams of the χ^2 distribution in the $\Sigma_{\text{cl}}-M_c$ space (left column), m_*-M_c space (center column), and $m_*- \Sigma_{\text{cl}}$ space (right column) for each source noted on top of each plot. The black cross denotes the best model.

4.4. MIR to FIR Variability Constraints from IRAS

Given the imaging presented above, and especially based on the $70 \mu\text{m}$ images, AFGL 2591, G25.40-0.14, G30.59-0.04, G33.92+0.11, G40.62-0.14, and HH 288 appear to be single sources within large enough regions that can be reasonably well fit with IRAS Gaussian point spread function fitting. However, the following considerations still apply.

While G25.40-0.14 appears to be a single source at 12, 25, and $60 \mu\text{m}$ within the IRAS square areas for Gaussian fitting based on its $70 \mu\text{m}$ image, there is another source to its SE and at $100 \mu\text{m}$ the two sources merge and become unresolved; thus, in this case, we cannot derive a reliable measurement at $100 \mu\text{m}$.

For G30.59-0.04, we find that it is moderately contaminated by a source to its east, especially at $100 \mu\text{m}$, which skews the Gaussian fitting. Also, the P.A. of the beam provided by the HIRES beam sample map does not align with the extension of the source. Thus, here we set P.A. as a free parameter and only fix the lengths of the major and minor axes. In addition, the $12 \mu\text{m}$ emission of G30.59-0.04 has very poor S/N and makes it hard to define the source.

We did not derive a valid flux from the IRAS images for G32.03+0.05 due to the presence of multiple sources. Within the IRAS square area, there are at least two strong sources revealed at 37.1 and $70 \mu\text{m}$. In the IRAS 60 and $100 \mu\text{m}$ images, the main protostar lies at the lower edge of the emission, so

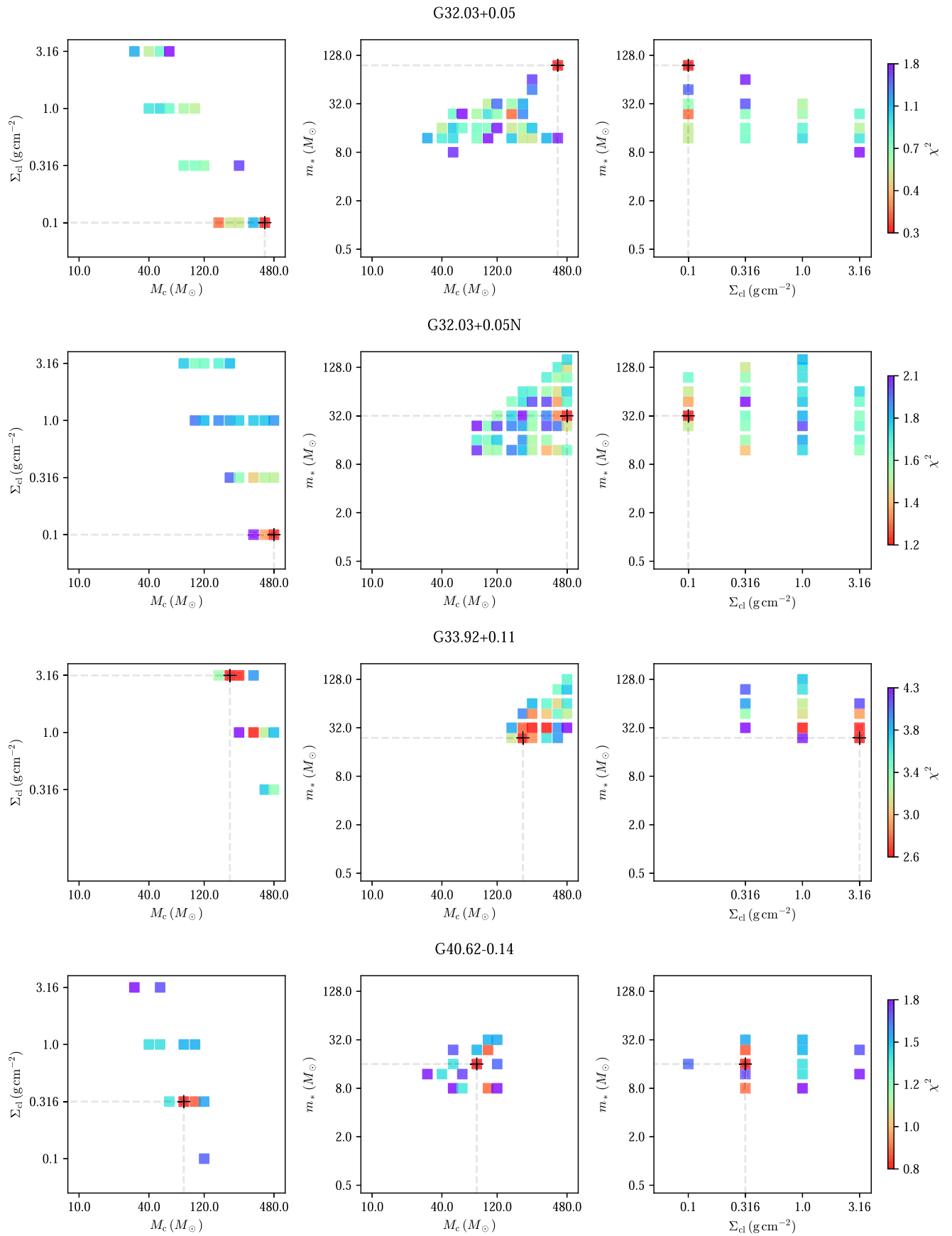
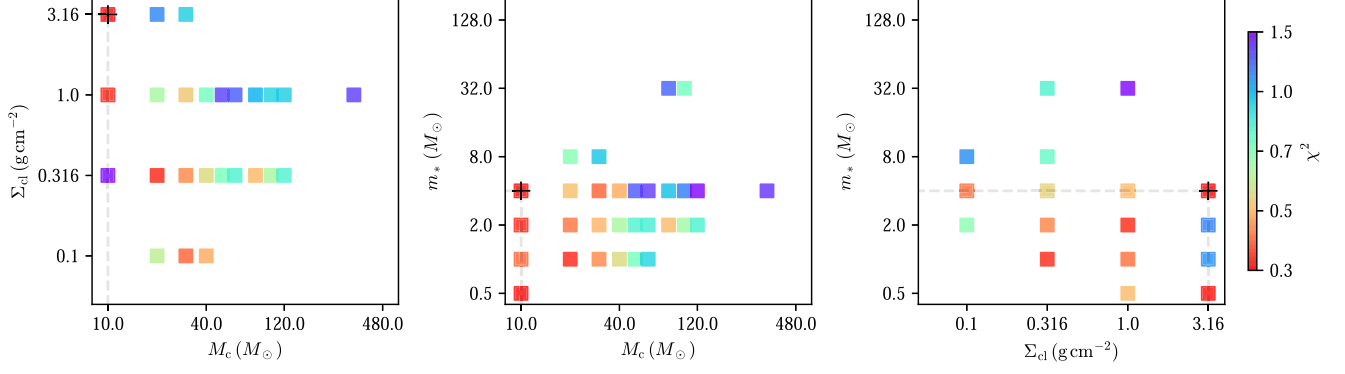
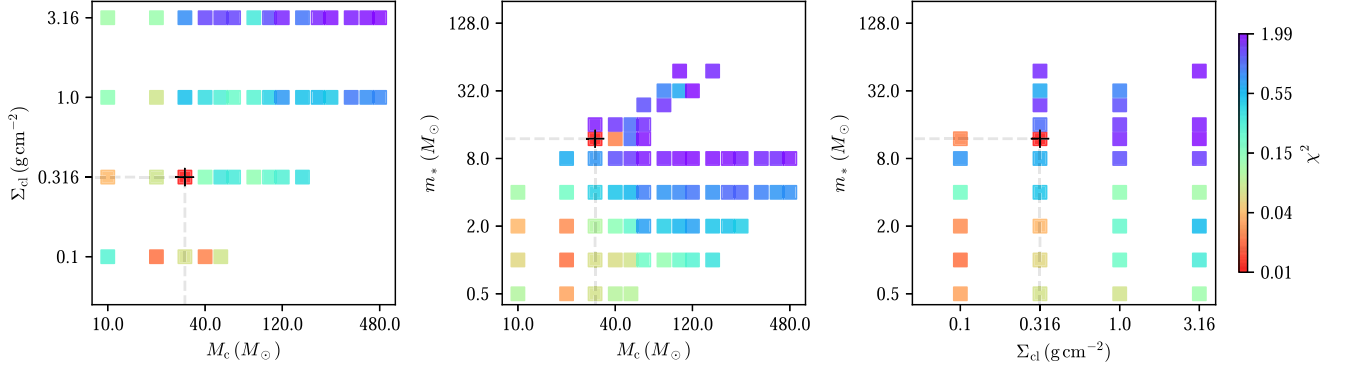


Figure 14. (Continued.)

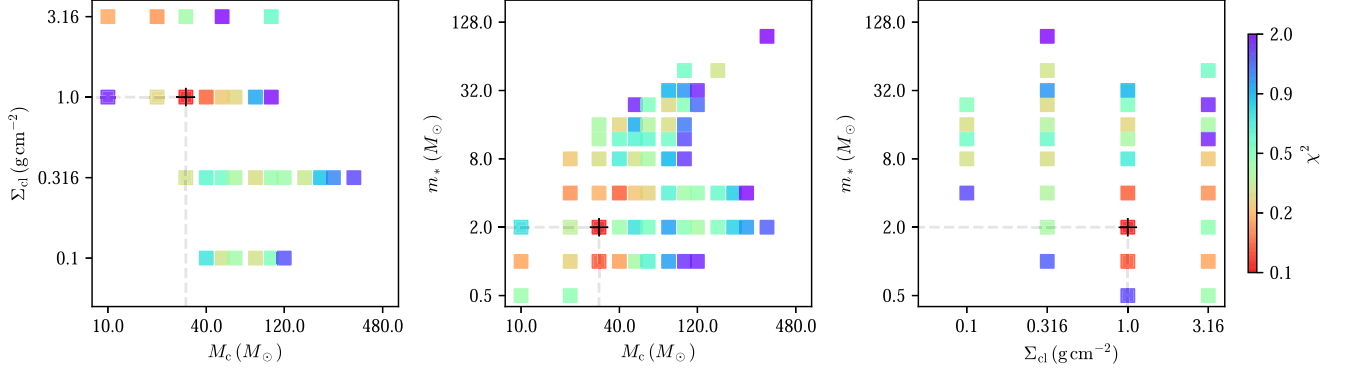
IRAS00420



IRAS00259



IRAS23385



HH288

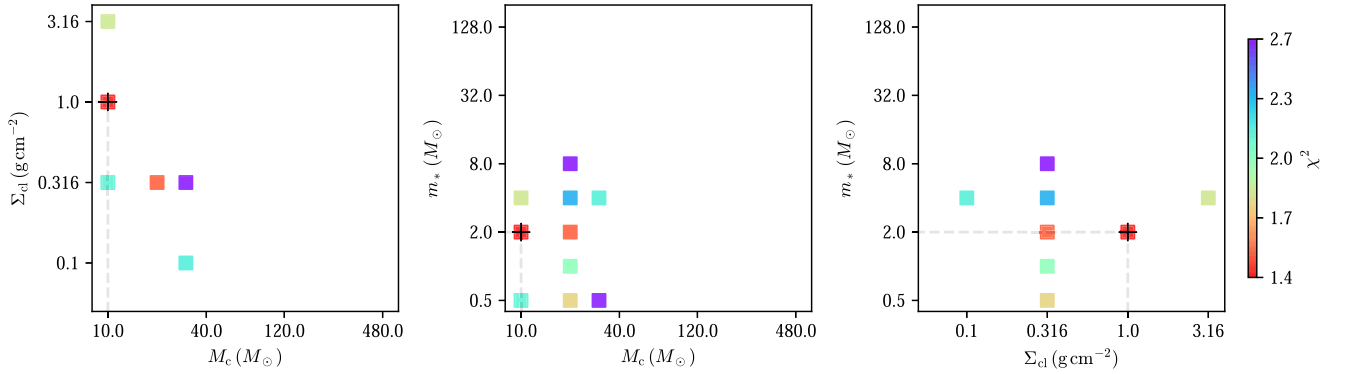


Figure 14. (Continued.)

clearly the 60 and 100 μm emission is dominated by other sources.

IRAS 00259+5625 and IRAS 00420+5530 do not have Herschel data. Their IRAS 12 and 25 μm emission have poor S/N and appear very extended. Their IRAS 60 and 100 μm emission exhibit a *tail* structure extending along the major axis, indicating impact by other sources within the beam.

IRAS 23385 has a companion located 95'' to the west, and has bright arc-shaped surrounding diffuse emission at 70 μm . The 60 μm IRAS image shows a tail to the west of the main source, which should be from this companion source. Thus a valid flux could not be retrieved for this source.

The S/N of the 12 μm emission of HH 288 is very poor, so the source cannot be well characterized at this wavelength.

With the above caveats noted, we plot our estimated IRAS-derived fluxes of the sources in Figure 13 (shown as red open squares). We note that because of the possibility of source contamination in the larger IRAS beam, these should generally be regarded as being upper limits on the source fluxes. Along with these data, we also show the expected fluxes in the IRAS bands from the average of the good models (shown as red open circles). We consider that a clear signature of variability would be when the model-fit SEDs, i.e., that are derived from the more recent SOFIA observations, and their prediction of IRAS fluxes exceeds the actual observed IRAS fluxes. We do not find any clear cases of this situation (i.e., red circles being higher than red squares) and so conclude there is no evidence for variability in this sample over the ~ 40 yr time baseline between the IRAS and SOFIA observations.

5. Discussion of Global SOMA Sample Results

Here, we discuss the overall results from the SOMA survey, i.e., the sources of Papers I–III, which have been reanalyzed with the methods of this paper, and the 11 new sources we have presented here in Paper IV. In total, this is a combined sample of 40 high- and intermediate-mass protostars that have been analyzed uniformly. In addition, we will also make a comparison to protostars that have been identified in IRDCs by Moser et al. (2020) and Liu et al. (2021): these SEDs were measured based on Spitzer and Herschel data and also fitted to the ZT-RT model grid.

5.1. The SOMA Sample Space and the Evolutionary Sequence of Massive Star Formation

Figure 15 shows the isotropic bolometric luminosity ($L_{\text{bol,iso}}$, top row) and true bolometric luminosity (L_{bol} , middle and bottom rows) versus envelope mass (M_{env}) of all the SOMA protostars. Note, these quantities are derived as averages of all good models that are fit to the SEDs. We see that the current sample of protostars presented in this paper span a range of luminosities from the upper end of the intermediate-mass sources presented in Paper III up to and beyond the highest end of the luminosity range probed previously in Paper II. Indeed, the most luminous source in terms of $L_{\text{bol,iso}}$ is AFGL 2591 with $7 \times 10^5 L_{\odot}$. However, in terms of the ratio of luminosity to mass, we do not perceive any significant difference in the relatively isolated protostars of SOMA IV compared to the other sources. While there is an apparent tight correlation between $L_{\text{bol,iso}}$ and M_{env} , this becomes weaker when considering L_{bol} and M_{env} . The theoretical protostellar evolutionary tracks (shown in the bottom row of Figure 15) cover a wide

range in this parameter space, i.e., going from low-luminosity cores with high envelope masses to high-luminosity protostars with only small amounts of residual envelope mass. Including the IRDC sources of Moser et al. (2020) and Liu et al. (2021) gives more extensive coverage of the low-luminosity, high-mass end of these tracks.

The lack of sources at the high-luminosity low-mass end of the evolutionary sequence may reflect choices made in the selection of SOMA sources. Such sources would tend to be near the end of their formation phase and, for the most massive protostars, would be producing ionizing gas, i.e., likely appearing as UC H II regions. Furthermore, the lifetime of sources in this phase may be relatively short, which would reduce the number of such systems that may be observed or selected to be analyzed. Finally, with a focus on MIR to FIR emission, i.e., selecting sources that are relatively bright in these wave bands, may mean that the later protostellar evolutionary stages, perhaps with most luminosity emerging in the ultraviolet, optical, or NIR, are underrepresented.

5.2. MIR-FIR SED Shape

As discussed in SOMA Papers I–III, the shape of the MIR to FIR SED is expected to correlate with intrinsic protostellar properties, such as viewing angle with respect to the outflow axis and evolutionary stage. Essentially, the protostars appear relatively brighter in the MIR if we look down their outflow cavities or if we see them at later stages when their envelopes are warmer and have less internal extinction.

To explore the potential diagnostic power of the shape of the MIR to FIR SED, Figure 16 shows the values of the 19–37 μm spectral index,

$$\alpha_{19-37} = \frac{\log_{10}(\nu_{37\mu\text{m}} F_{\nu_{37\mu\text{m}}}) - \log_{10}(\nu_{19\mu\text{m}} F_{\nu_{19\mu\text{m}}})}{\log_{10}(\lambda_{37\mu\text{m}}) - \log_{10}(\lambda_{19\mu\text{m}})}, \quad (1)$$

of all the SOMA protostars versus various inferred properties of the systems, i.e., luminosity, inclination of viewing angle, outflow cavity opening angle, and the ratio of inclination of viewing angle to outflow cavity opening angle, Σ_{cl} , and m_*/M_c . In this figure, the observed values of α_{19-37} of the SOMA protostars are shown with blue symbols, with the corresponding value of the protostellar property being the average of good models. For reference, we also show all the individual good models as light gray points for their unextincted spectral indices and as dark gray points after applying the best-fit extinction. Recall that it is the latter that is fit to the observed SEDs represented by the blue points.

Figure 16 shows that α_{19-37} has the strongest correlation with the ratio $\theta_{\text{view}}/\theta_{\text{w,esc}}$, but there are also related weaker correlations with θ_{view} and $\theta_{\text{w,esc}}$ individually, as well as with the evolutionary stage as parameterized via m_*/M_c . The data here allow one to gauge the uncertainty in estimating these intrinsic protostellar properties (as based on the average of good model fits to full SEDs), if only α_{19-37} is known. On the other hand, Figure 16 shows that there is limited apparent correlation of the value of α_{19-37} with $L_{\text{bol,iso}}$ or Σ_{cl} , i.e., these quantities are not well constrained by the MIR to FIR spectral slope.

Other important points that are illustrated in Figure 16 include the fact that the correction for foreground extinction can typically have a significant effect on α_{19-37} (e.g., compare the distribution of light and dark gray points). This means that

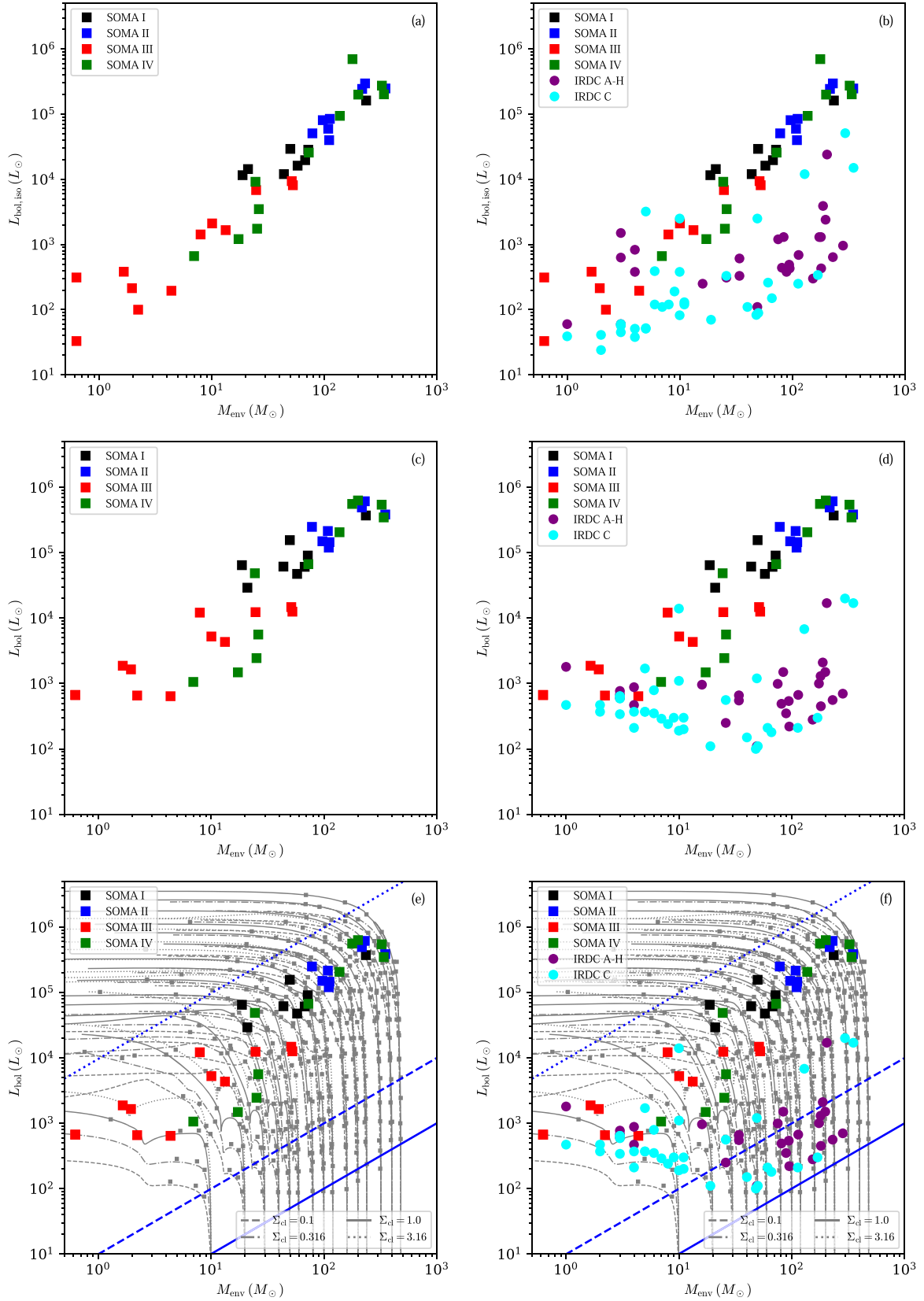


Figure 15. (a) Top left: isotropic bolometric luminosity ($L_{\text{bol,iso}}$) vs. mass of the envelope (M_{env}). Data from SOMA Papers I–IV are shown, as indicated. (b) Top right: as in (a), but now including protostars selected from IRDCs by Liu et al. (2020; IRDC A–H) and Moser et al. (2020; IRDC C). (c) Middle left: as in (a), but now for bolometric luminosity (L_{bol}) vs. M_{env} . (d) Middle right: as in (c), but now also including IRDC protostars. (e) Bottom left: as in (c), but now including the ZT18 protostellar evolutionary tracks (gray lines and squares) for different initial core masses and clump mass surface densities (see legend). The three blue lines indicate $L_{\text{bol}}/M_{\text{env}} = 1$ (solid line), 10 (dashed line), and $10^4 L_{\odot}/M_{\odot}$ (dotted line). (f) Bottom right: as in (f), but now also including IRDC protostars.

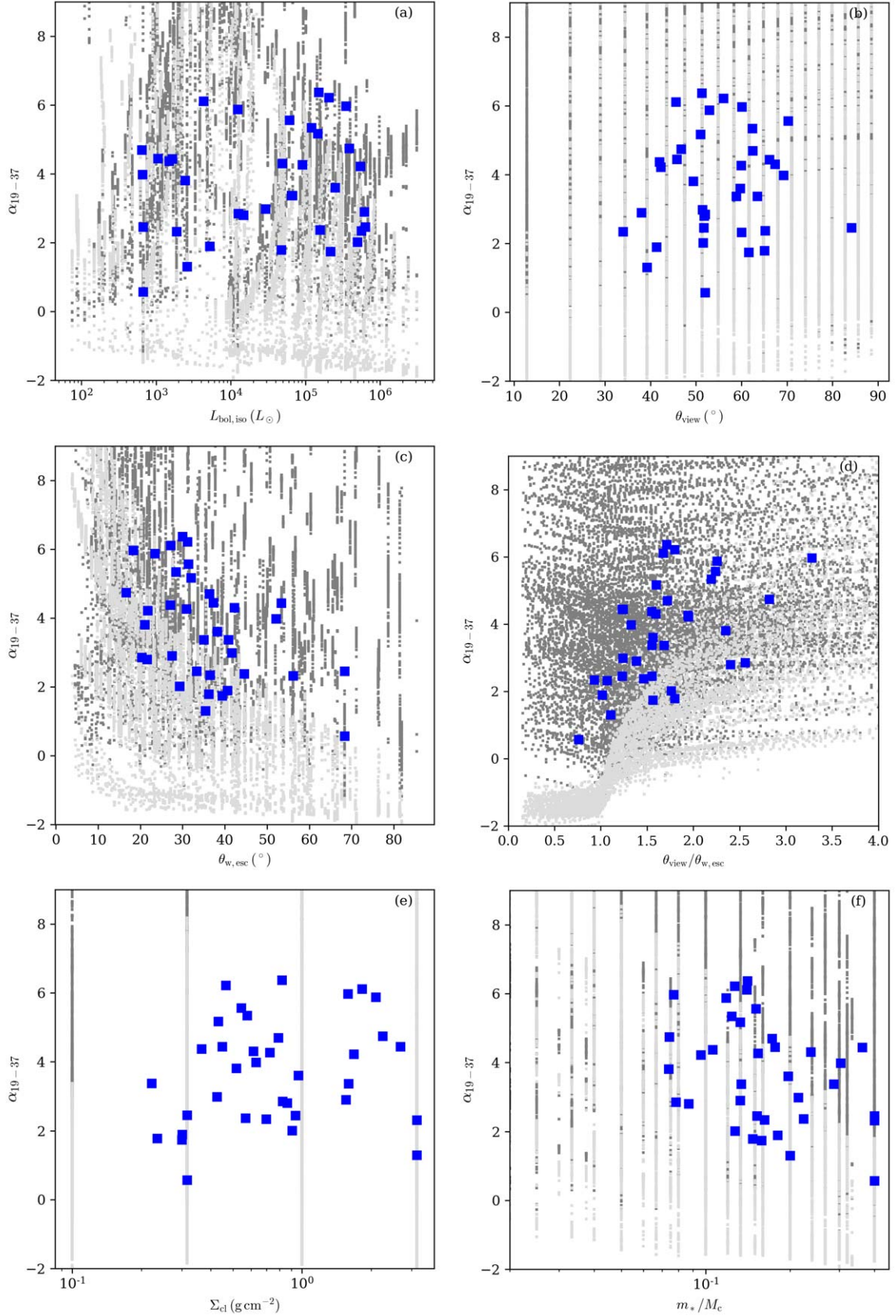


Figure 16. Spectral index, α_{19-37} between 19 and 37 μm (see the text) vs. the geometric mean isotropic luminosity $L_{\text{bol,iso}}$ ((a) top left), the arithmetic mean inclination of viewing angle θ_{view} ((b) top right), the arithmetic mean opening angle $\theta_{\text{w,esc}}$ ((c) middle left), the arithmetic mean $\theta_{\text{view}}/\theta_{\text{w,esc}}$ ((d) middle right), the geometric mean clump surface density Σ_{cl} ((e) bottom left), and the geometric mean m_*/M_{\odot} ((f) bottom right) returned by the good models. Small light gray points represent models without correction for foreground extinction whereas dark gray points include the correction for foreground extinction.

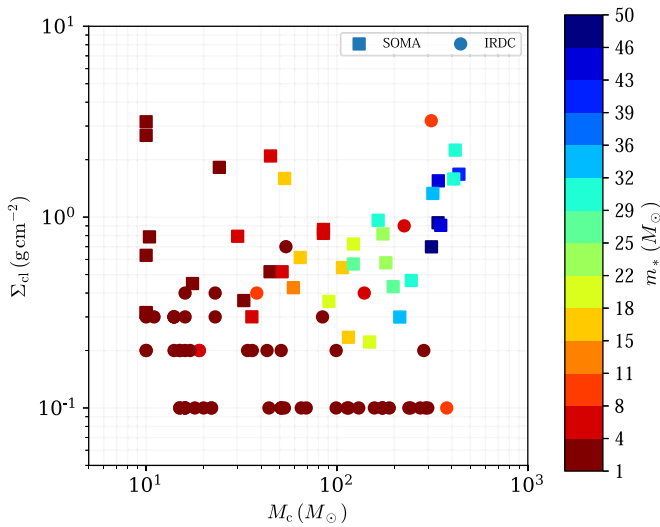


Figure 17. Mass surface density of the clump environment (Σ_{cl}) vs. initial mass of the core (M_c) for the full SOMA sample to date and the IRDC samples. Each data point is the average of good model fits. Each point is also color coded with the current mass of the protostar (m_*).

in the ideal case observed value of α_{19-37} should be corrected for this extinction, which would require additional information, e.g., using colors based on filters at shorter wavelengths, or via some independent method, e.g., based on the ratio of H_2 emission lines that may be detected in the outflow cavity (Fedriani et al. 2018, 2019, 2020; Costa Silva et al. 2022). Another important caveat to note is that there are degeneracies in protostellar model properties for a given SED or value of α_{19-37} , i.e., the dispersion in the light gray points is larger than that of the blue points. However, this is a problem that also affects protostellar properties derived from full SED fitting.

5.3. The Environmental Dependence of Massive Star Formation

Here, we examine if there are any dependencies of massive protostar properties on the mass surface density of the clump environment, Σ_{cl} , in which it is forming. Higher values of Σ_{cl} imply higher pressures in a self-gravitating clump, which then lead to higher densities of prestellar cores in the turbulent core model of McKee & Tan (2003). This in turn leads to higher accretion rates, shorter formation times, and more efficient formation from a core of a given mass under the action of internal feedback processes from the protostar (Tanaka et al. 2017). Furthermore, there have been proposed theoretical models that predict that the existence of massive prestellar cores requires certain conditions on Σ_{cl} . In particular, Krumholz & McKee (2008) suggested that to prevent fragmentation of a massive prestellar core one requires $\Sigma_{\text{cl}} \gtrsim 1 \text{ g cm}^{-2}$ and the presence of a surrounding cluster of lower-mass protostars, which then have high enough accretion rates and high enough accretion luminosities to provide sufficient heating of the massive core so that the Jeans mass is raised to high-mass scales. On the other hand, Butler & Tan (2012) have discussed how the presence of moderate strength ($\sim 0.1 \text{ mG}$) magnetic fields within massive prestellar cores can prevent their fragmentation in cold conditions. In this case, massive prestellar cores and massive star formation could occur in environments with $\Sigma_{\text{cl}} < 1 \text{ g cm}^{-2}$.

Recall that the three main physical parameters that are derived in our SED fitting are the initial mass of the core (M_c), mass surface density of the clump (Σ_{cl}), and current protostellar mass (m_*). We note that when considering these results, one should recall the caveats that these quantities are relatively indirect inferences from SED fitting, that there can be significant degeneracies (i.e., dispersion) in these properties among good-fitting SED models and that there could be systematic uncertainties, e.g., if the luminosity is overestimated because of the presence of multiple sources.

Figure 17 shows the distribution of the averaged good models (see Section 3.2.2) as M_c versus Σ_{cl} and color coded with m_* for the 40 sources analyzed so far in the SOMA survey. We find that the analyzed sample contains protostars ranging in current mass from ~ 2 to $\sim 50 M_\odot$ and spanning the full range in the ZT grid of M_c and Σ_{cl} (see Section 3.2.1). Both low- and high-mass protostars are found to be forming from cores with high initial masses (and thus also generally high current envelope masses). One also notices a tendency for the most massive protostars to have higher values of Σ_{cl} .

In Paper III, we explored the relationship between the mass surface density of the clump and the current mass of the protostar. In this earlier work, we found tentative evidence that the most massive protostars (i.e., $m_* \gtrsim 25 M_\odot$) in our sample require their cores to be in environments with $\Sigma_{\text{cl}} \gtrsim 1.0 \text{ g cm}^{-2}$. With the addition of SOMA IV sources and the updated methods presented here, e.g., of aperture definition, that have been applied to all the SOMA sample, we now reexamine this result.

Figure 18(a) shows the values of m_* versus Σ_{cl} for the SOMA survey sample to date. One can see how the most massive protostars, i.e., with $m_* > 25 M_\odot$, tend to be concentrated in the higher Σ_{cl} region of parameter space. However, in contrast to the results presented in SOMA III, there are now some examples of such stars with Σ_{cl} in the range of $0.3\text{--}1.0 \text{ g cm}^{-2}$. Furthermore, as also found in SOMA III, there are numerous examples of *high-mass* protostars, i.e., with $8 M_\odot < m_* < 25 M_\odot$, that have Σ_{cl} spanning the full explored range from $\sim 0.1\text{--}3 \text{ g cm}^{-2}$. Figure 18(b), which includes IRDC sources, also shows that lower-mass protostars, i.e., with $m_* < 8 M_\odot$, are also found across the full range of Σ_{cl} .

Figure 18(b) shows the fiducial condition on Σ_{cl} for massive star formation from Krumholz & McKee (2008, KM08; red solid line). The prediction is that massive protostars should only be found to the right of this line, i.e., which defines a minimum Σ_{cl} for high-mass star formation. We see that the SOMA results are inconsistent with this prediction, i.e., there are numerous massive protostars that appear to be forming in conditions with $\Sigma_{\text{cl}} \ll 1 \text{ g cm}^{-2}$. We conclude that prevention of fragmentation of massive cores by approximately milligauss-strength magnetic fields (e.g., Butler & Tan 2012) is more likely to be the condition needed for massive star formation. Indeed, such B -field strengths have been inferred to be present in some IRDCs (Pillai et al. 2015), including in a massive prestellar core (Beuther et al. 2018b), as well as in massive protostellar cores (Girart et al. 2009; Zhang et al. 2014a; Beltrán et al. 2019).

While the KM08 relation does not appear to give a good description of the conditions needed to form massive stars, as noted, the data in Figure 18 do suggest a trend that the most massive protostars tend to be in higher Σ_{cl} environments. The internal protostellar feedback model of Tanaka et al. (2017)

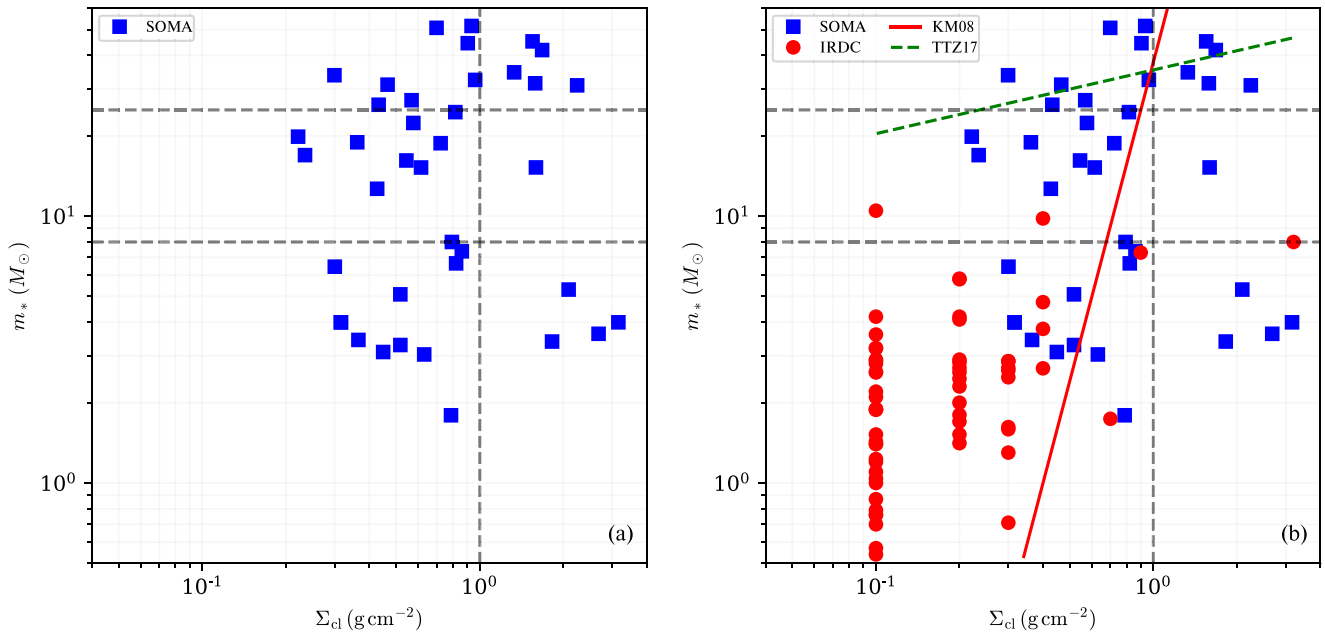


Figure 18. (a) Left panel: current protostellar mass (m_*) vs. clump environment mass surface density (Σ_{cl}) for the 40 SOMA sources of Papers I–IV. Lines indicating reference values of $m_* = 8$ and $25 M_\odot$ and $\Sigma_{\text{cl}} = 1 \text{ g cm}^{-2}$ (see the text) are highlighted. (b) Right panel: as in (a), but now including IRDC protostars (see the text). The red solid line shows the fiducial prediction of Krumholz & McKee (2008; assuming their parameter values of $\delta = 1$ and $T_b = 10 \text{ K}$) for the minimum Σ_{cl} needed to form a star of given mass m_* . The green-dashed line shows the results for the final stellar mass formed from $100 M_\odot$ prestellar cores as a function of Σ_{cl} (Tanaka et al. 2017).

provides one way to help explain this result. Figure 18(b) shows the results of an example set of models from Tanaka et al. (2017; green-dashed line), which show the final value of m_* that is expected to result from $M_c = 100 M_\odot$ prestellar cores under different Σ_{cl} conditions. As a result of internal feedback from the protostar on its infall envelope and disk, it is more difficult for the star to reach very high masses (i.e., $\gtrsim 20 M_\odot$) when Σ_{cl} is low (i.e., $\sim 0.1 \text{ g cm}^{-2}$). If the prestellar core mass function is universal under different Σ_{cl} conditions, e.g., with a maximum value of $\sim 200 M_\odot$, then the upper envelope of the SOMA sample in the m_* – Σ_{cl} plane could be explained.

Further tests of the internal feedback model are needed. For example, the main source of protostellar feedback is that due to disk-wind outflows. A prediction is that the outflow cavity opening angle is larger at later evolutionary stages. Such a prediction can be tested by measuring the cavity opening angles based on the NIR to MIR morphology of the sources, i.e., with the shorter wavelength emission tending to emerge only from the outflow cavity. Analysis of high-resolution NIR imaging data of the SOMA sources or high-resolution CO outflow data is needed to help measure outflow cavity geometries in the sources.

6. Conclusions

In the fourth paper of the SOMA series, we have analyzed 11 relatively isolated (as defined by SOFIA-FORCAST $37 \mu\text{m}$ morphology) massive protostars using observations from the MIR to FIR, including data from the Spitzer, SOFIA, and Herschel telescopes. We have introduced new methods via the python package *sedcreator*, which helps with the construction of SEDs. It has a number of tools that allows one to measure fluxes and fit them to the model grid of ZT18. It also includes a tool to select in an algorithmic way the aperture size, important for a systematic measurement of the fluxes and subsequent SED fitting. Together with the protostars studied in SOMA

Papers I–III, which we have also reanalyzed with the new methods, a total of 40 sources have been characterized in a uniform and systematic manner. Below, we summarize our main findings:

1. The 11 *isolated* protostars analyzed in this work span a wide range in bolometric luminosity, i.e., $\sim 10^2$ – $10^3 L_\odot$. Fitting the SEDs with the RT models, we obtain protostellar masses ranging from $m_* \sim 3$ – $50 M_\odot$, which are accreting at rates of $\dot{m}_{\text{disk}} \sim 10^{-5}$ – $10^{-3} M_\odot \text{ yr}^{-1}$ from cores with initial masses $M_c \sim 20$ – $430 M_\odot$ and in clump environments with mass surface densities ranging from $\Sigma_{\text{cl}} \sim 0.3$ – 1.7 g cm^{-2} .
2. We report the average results of all good fits to the SEDs and include information on the dispersion of the model parameters. This helps illustrate the range of degeneracies that are present in the SED-fitting method.
3. The relatively isolated nature of the sources we have considered here allows us to search for MIR to FIR variability over an approximately 40 yr time baseline by comparison with archival IRAS data. From this analysis, we do not find evidence of significant flux variability of the protostars.
4. The distribution of SOMA and IRDC sources in the L versus M_{env} plane shows that a large part of the theoretically expected evolutionary sequence is covered by these samples. However, these samples do not currently include sources at the very latest evolutionary stages, i.e., with relatively small envelope masses.
5. The distribution of SOMA and IRDC sources in the m_* versus Σ_{cl} plane places constraints on theoretical models for the conditions needed for massive star formation. The observed distribution is inconsistent with there being a sharp threshold minimum $\Sigma_{\text{cl}} \sim 1 \text{ g cm}^{-2}$ needed to form massive protostars as has been proposed by Krumholz & McKee (2008). However, the upper end of the

distribution appears to follow trends predicted by models of internal protostellar feedback that find higher star formation efficiency in higher Σ_{cl} conditions (Tanaka et al. 2017).

6. This sample of protostars, which appear relatively isolated in their MIR to FIR emission, is a further constraint on massive star formation theories. The images we present here can be used to test any predictions of such models, e.g., for $37\ \mu\text{m}$ flux profiles. We anticipate that models of massive star formation that involve the presence of a surrounding cluster of lower-mass protostars may struggle to reproduce the morphologies seen in this sample.
7. We released the open-source python package *sedcreator* to construct and fit SEDs. It includes several functions encapsulated into the two main classes *SedFluxer* and *SedFitter*, which allow the user to measure fluxes on an image and/or fit the given fluxes to the *ZT18* model grid based on the TCA models.

R.F. has received funding from the European Union’s Horizon 2020 research and innovation program under the Marie Skłodowska-Curie grant agreement No 101032092. J.C.T. acknowledges funding from NASA/USRA/SOFIA, from NSF grant AST1411527 and ERC project 788829 MSTAR. K.E.I.T. acknowledges the support by JSPS KAKENHI grant Nos. JP19K14760, JP19H05080, JP21H00058, and JP21H01145. Y.-L.Y acknowledges the support from the Virginia Initiative of Cosmic Origins Postdoctoral Fellowship. G.C. acknowledges funding from the Vetenskapsrådet-Swedish Research Council (project No. 2021-05589).

Appendix SOMA I–III Revisited

In order to achieve a systematic and uniform analysis with the methods developed in this paper, we reanalyzed all the protostars of SOMA Papers I–III with *sedcreator*, especially using the new automated algorithm to choose the aperture size. We then fit all the sources using the new methods detailed in the main text. In this appendix, we present the new fluxes, aperture sizes, and SED fit results. Tables A1 and A2 present the revisited fluxes and best models, respectively, for SOMA I–III sources.

A1. SOMA I New SED Fit

We revisited the measurement and error estimation for the SOMA I sources (De Buizer et al. 2017) as well as refit their SEDs. Figures A1 and A2 show the revisited results.

A2. SOMA II New SED Fit

We revisited the measurement and error estimation for the SOMA II sources (Liu et al. 2019b) as well as refit their SEDs. Figures A3 and A4 show the revisited results.

A3. SOMA III New SED Fit

We revisited the measurement and error estimation for the SOMA I sources (Liu et al. 2020) as well as refit their SEDs. Figures A5 and A6 show the revisited results.

Table A1
Integrated Flux Densities for Sources in SOMA I–III, as Indicated

Source	Radius (" / pc)	$F_{3.6}$ (Jy)	$F_{4.5}$ (Jy)	$F_{5.8}$ (Jy)	$F_{7.7}$ (Jy)	$F_{8.0}$ (Jy)	$F_{11.1}$ (Jy)	$F_{19.1}$ (Jy)	$F_{24.4}$ (Jy)	$F_{31.5}$ (Jy)	$F_{37.1}$ (Jy)	F_{70} (Jy)	F_{100} (Jy)	F_{160} (Jy)	F_{250} (Jy)	F_{350} (Jy)	F_{500} (Jy)
SOMA I																	
AFGL 4029	12.75	0.84	1.03	4.81	12.88	2.87	...	59.65	...	195.69	426.69	448.78	458.67	244.81	62.85	13.95	2.35
	0.12	(0.92)	(1.13)	(5.26)	(12.76)	(3.56)	...	(60.33)	...	(200.14)	(434.95)	(489.45)	(533.01)	(339.53)	(118.64)	(40.23)	(10.59)
		[0.15]	[0.21]	[1.08]	[3.71]	[1.26]	...	[22.91]	...	[66.65]	[148.73]	[97.66]	[98.67]	[100.85]	[56.49]	[26.35]	[8.25]
AFGL 437	29.5	1.88	2.03	9.81	28.47	14.36	...	266.45	...	718.34	865.59	1126.75	...	603.84	197.43	68.25	18.45
	0.29	(1.98)	(2.10)	(10.61)	(28.47)	(15.87)	...	(266.45)	...	(718.34)	(865.59)	(1172.12)	...	(731.68)	(275.82)	(109.82)	(35.41)
		[0.27]	[0.29]	[1.44]	[4.03]	[2.16]	...	[37.68]	...	[101.59]	[122.41]	[160.60]	...	[153.74]	[83.21]	[42.68]	[17.15]
IRAS 07299	7.5	1.33	2.39	3.11	3.42	2.97	...	73.75	...	443.77	678.91
	0.06	(1.41)	(2.51)	(3.28)	(3.30)	(3.17)	...	(73.99)	...	(455.63)	(701.20)
		[0.19]	[0.34]	[0.44]	[0.50]	[0.42]	...	[10.44]	...	[62.95]	[96.46]
G35.20-0.74	18.75	0.46	1.04	1.63	66.72	...	521.93	1109.92	2428.66	...	1899.93	656.47	212.66	41.06
	0.20	(0.52)	(1.12)	(1.86)	(66.69)	...	(522.93)	(1110.19)	(2554.82)	...	(2211.92)	(858.19)	(318.12)	(84.94)
		[0.07]	[0.15]	[0.23]	[9.44]	...	[73.82]	[157.02]	[344.32]	...	[411.75]	[222.06]	[109.67]	[44.26]
G45.47+0.05	15.0	0.07	0.20	0.10	...	−0.11	0.17	...	39.28	137.63	201.95	1107.81	...	867.49	250.83	74.47	10.81
	0.61	(0.13)	(0.28)	(0.64)	...	(1.41)	(0.17)	...	(33.17)	(137.63)	(201.95)	(1242.68)	...	(1124.52)	(378.40)	(130.56)	(32.27)
		[0.03]	[0.03]	[0.24]	...	[0.34]	[0.15]	...	[9.43]	[21.94]	[31.97]	[163.74]	...	[284.81]	[132.41]	[57.08]	[21.52]
IRAS 20126	12.75	...	1.52	1.95	...	1.40	0.44	...	188.55	438.36	730.87	1569.11	1420.53	704.73	170.33	36.53	4.82
	0.10	...	(1.58)	(2.28)	...	(2.07)	(−0.53)	...	(190.35)	(440.31)	(739.97)	(1637.86)	(1532.84)	(836.30)	(241.45)	(74.66)	(15.59)
		...	[0.22]	[0.28]	...	[0.22]	[0.29]	...	[26.68]	[62.01]	[103.39]	[223.21]	[230.15]	[165.06]	[75.09]	[38.47]	[10.79]
Cep A	36.25	...	12.59	...	8.62	9.10	...	155.32	...	2684.87	6076.62	15565.73	...	8371.25	...	837.96	229.84
	0.12	...	(13.06)	...	(8.62)	(11.04)	...	(155.32)	...	(2684.87)	(6076.62)	(16220.96)	...	(9388.70)	...	(1085.86)	(316.30)
		...	[2.17]	...	[1.80]	[1.45]	...	[27.90]	...	[385.09]	[864.25]	[2266.67]	...	[1561.01]	...	[274.77]	[92.36]
NGC 7538	13.75	0.80	2.21	7.83	63.05	5.38	...	167.88	...	586.60	803.64	1407.51	...	624.73	142.91	33.90	3.69
	0.18	(0.87)	(2.42)	(9.02)	(63.05)	(6.65)	...	(167.88)	...	(593.56)	(809.09)	(1495.68)	...	(804.30)	(245.16)	(79.40)	(19.80)
		[0.13]	[0.34]	[1.12]	[8.92]	[0.77]	...	[23.86]	...	[83.01]	[113.74]	[199.37]	...	[200.13]	[104.23]	[45.76]	[16.12]
SOMA II																	
G45.12+0.13	47.0	...	7.30	40.61	92.62	1086.23	...	3042.48	4101.66	6542.52	...	3840.57	...	415.35	118.64
	1.69	...	(7.79)	(44.50)	(92.62)	(1086.23)	...	(3042.48)	(4101.66)	(6857.41)	...	(4220.04)	...	(520.62)	(158.77)
		...	[1.11]	[5.99]	[16.42]	[174.86]	...	[476.23]	[635.76]	[959.77]	...	[662.57]	...	[120.55]	[43.50]
G309.92+0.48	17.75	2.17	...	16.68	39.50	23.00	...	365.21	...	1808.20	2466.17	3228.50	...	1669.32	...	130.49	23.16
	0.47	(2.27)	...	(17.70)	(40.85)	(25.20)	...	(367.78)	...	(1826.86)	(2491.95)	(3353.09)	...	(1896.87)	...	(188.72)	(45.29)
		[0.31]	...	[2.38]	[5.65]	[3.36]	...	[51.73]	...	[255.73]	[348.85]	[456.64]	...	[327.89]	...	[61.09]	[22.37]
G35.58-0.03	16.0	0.23	0.32	1.42	4.87	3.36	...	21.53	...	265.07	490.17	1421.82	...	822.12	222.42	59.59	7.20
	0.79	(0.36)	(0.44)	(2.21)	(4.89)	(5.83)	...	(23.27)	...	(266.56)	(499.77)	(1506.58)	...	(948.23)	(292.26)	(92.49)	(22.85)
		[0.05]	[0.05]	[0.29]	[1.00]	[0.47]	...	[3.32]	...	[37.78]	[69.77]	[202.44]	...	[171.53]	[76.60]	[33.96]	[15.68]
IRAS 16562	17.5	2.24	...	25.28	65.94	18.90	...	237.75	...	1829.72	2554.34
	0.14	(2.61)	...	(28.06)	(69.12)	(24.57)	...	(234.48)	...	(1856.85)	(2621.86)
		[0.34]	...	[3.70]	[9.84]	[3.34]	...	[34.17]	...	[260.96]	[364.44]

Table A1
(Continued)

Source	Radius (" / pc)	$F_{3.6}$ (Jy)	$F_{4.5}$ (Jy)	$F_{5.8}$ (Jy)	$F_{7.7}$ (Jy)	$F_{8.0}$ (Jy)	$F_{11.1}$ (Jy)	$F_{19.1}$ (Jy)	$F_{24.4}$ (Jy)	$F_{31.5}$ (Jy)	$F_{37.1}$ (Jy)	F_{70} (Jy)	F_{100} (Jy)	F_{160} (Jy)	F_{250} (Jy)	F_{350} (Jy)	F_{500} (Jy)
G305.20+0.21	11.25	20.06	241.88	...	593.61	763.37	974.01	...	497.13	...	32.96	9.96
	0.22	(21.01)	(241.87)	...	(614.25)	(797.89)	(1236.21)	...	(786.93)	...	(92.85)	(26.37)
		[4.48]	[44.24]	...	[96.84]	[119.98]	[254.26]	...	[298.21]	...	[60.07]	[16.47]
G305.20+0.21A	10.0	-0.15	2.33	...	92.97	154.87	944.78	...	814.09	...	54.49	5.30
	0.20	(-0.30)	(0.64)	...	(100.43)	(164.48)	(1177.90)	...	(1262.40)	...	(134.98)	(29.66)
		[0.80]	[4.81]	...	[23.71]	[44.48]	[176.96]	...	[462.85]	...	[80.86]	[24.38]
G49.27-0.34	24.75	0.10	0.76	2.05	4.43	2.82	...	66.94	85.05	439.91	...	801.94	361.11	143.94	33.51
	0.67	(0.24)	(0.91)	(3.33)	(4.43)	(2.82)	...	(66.94)	(85.05)	(547.65)	...	(1051.00)	(521.27)	(221.08)	(66.36)
		[0.02]	[0.11]	[0.32]	[1.34]	[0.68]	...	[9.69]	[12.17]	[62.75]	...	[273.66]	[168.11]	[79.77]	[33.19]
G339.88-1.26	20.25	4.94	33.32	...	692.22	1125.47	3085.45	...	2021.52
	0.21	(9.07)	(28.20)	...	(695.79)	(1145.93)	(3304.79)	...	(2261.84)
		[4.02]	[4.77]	...	[98.70]	[160.61]	[437.83]	...	[373.48]
SOMA III																	
S235	7.0	0.28	...	1.94	5.61	2.31	...	31.56	...	64.81	74.46
	0.06	(0.30)	...	(2.05)	(5.67)	(2.43)	...	(32.20)	...	(66.47)	(77.11)
		[0.04]	...	[0.27]	[0.80]	[0.33]	...	[4.46]	...	[9.20]	[10.57]
IRAS 22198	6.25	0.01	0.03	0.09	0.19	0.16	...	5.31	...	72.74	98.94	...	181.16	78.08	9.86	2.08	...
	0.02	(0.01)	(0.04)	(0.11)	(0.32)	(0.20)	...	(5.95)	...	(75.10)	(102.04)	...	(216.74)	(119.06)	(33.07)	(10.21)	...
		...	[0.01]	[0.01]	[0.09]	[0.02]	...	[0.76]	...	[10.30]	[14.26]	...	[43.84]	[42.45]	[23.25]	[8.14]	...
NGC 2071	11.5	5.60	88.20	...	328.38	407.11	809.02	931.50	590.37	...	45.11	5.07
	0.02	(5.60)	(88.20)	...	(335.19)	(408.69)	(854.79)	(1024.53)	(731.53)	...	(86.82)	(22.32)
		[0.81]	[12.63]	...	[47.73]	[59.44]	[126.76]	[161.27]	[164.00]	...	[42.19]	[17.27]
Cep E	8.5	0.02	0.07	0.12	0.18	0.23	...	1.76	...	17.00	24.25	70.42	...	63.62	16.13	2.92	0.18
	0.03	(0.02)	(0.07)	(0.14)	(0.03)	(0.27)	...	(1.89)	...	(17.77)	(24.86)	(73.77)	...	(72.78)	(24.58)	(8.07)	(1.90)
		...	[0.01]	[0.02]	[0.05]	[0.03]	...	[0.48]	...	[2.43]	[3.45]	[9.98]	...	[12.84]	[8.75]	[5.17]	[1.73]
L1206A	6.5	0.07	0.18	0.22	0.26	1.85	...	60.30	104.16
	0.02	(0.08)	(0.20)	(0.25)	(0.26)	(2.11)	...	(62.43)	(106.29)
		[0.01]	[0.03]	[0.04]	[0.09]	[0.40]	...	[8.54]	[14.82]
L1206B	8.0	0.28	0.39	2.07	1.86	4.35	...	5.19	6.35
	0.03	(0.30)	(0.41)	(2.13)	(1.88)	(4.05)	...	(3.87)	(5.11)
		[0.04]	[0.05]	[0.29]	[0.29]	[0.85]	...	[0.84]	[1.15]
IRAS 22172 _{mir1}	8.0	0.10	0.10	0.30	1.17	0.72	...	0.93	...	3.28	6.12
	0.09	(0.14)	(0.12)	(0.45)	(1.33)	(1.11)	...	(0.93)	...	(3.58)	(6.82)
		[0.10]	[0.16]	[0.40]	[0.57]	[0.42]	...	[1.70]	...	[3.01]	[3.49]
IRAS 22172 _{mir2}	26.75	0.62	0.74	2.73	5.41	5.51	...	7.20	...	22.92	25.13
	0.31	(0.68)	(0.79)	(3.05)	(5.41)	(6.26)	...	(7.20)	...	(22.92)	(25.13)
		[0.11]	[0.11]	[0.44]	[0.77]	[0.94]	...	[1.02]	...	[3.24]	[3.55]
IRAS 22172 _{mir3}	7.75	0.04	0.03	0.23	0.89	0.62	...	0.90	...	4.26	5.71
	0.09	(0.05)	(0.04)	(0.31)	(1.04)	(0.83)	...	(1.02)	...	(5.01)	(5.71)

Table A1
(Continued)

Source	Radius (''/pc)	$F_{3.6}$ (Jy)	$F_{4.5}$ (Jy)	$F_{5.8}$ (Jy)	$F_{7.7}$ (Jy)	$F_{8.0}$ (Jy)	$F_{11.1}$ (Jy)	$F_{19.1}$ (Jy)	$F_{24.4}$ (Jy)	$F_{31.5}$ (Jy)	$F_{37.1}$ (Jy)	F_{70} (Jy)	F_{100} (Jy)	F_{160} (Jy)	F_{250} (Jy)	F_{350} (Jy)	F_{500} (Jy)
		[0.04]	[0.07]	[0.21]	[0.29]	[0.37]	...	[1.11]	...	[1.77]	[2.17]
IRAS 21391 _{bima2}	7.0	0.01	0.06	0.11	0.24	0.13	...	0.50	...	6.65	11.03
	0.03	(0.02)	(0.08)	(0.15)	(0.34)	(0.19)	...	(0.53)	...	(6.78)	(11.52)
		[0.01]	[0.02]	[0.03]	[0.04]	[0.04]	...	[0.12]	...	[2.80]	[3.92]
IRAS 21391 _{bima3}	7.75	0.02	0.06	0.09	0.23	0.11	...	0.27	...	8.66	12.94
	0.03	(0.03)	(0.08)	(0.14)	(0.32)	(0.19)	...	(0.27)	...	(8.66)	(13.12)
		[0.01]	[0.03]	[0.04]	[0.10]	[0.06]	...	[0.28]	...	[2.58]	[4.21]
IRAS 21391 _{mir48}	7.75	0.05	0.08	0.14	0.23	0.22	...	0.93	...	3.39	4.70
	0.03	(0.05)	(0.09)	(0.17)	(0.29)	(0.26)	...	(0.93)	...	(3.14)	(4.04)
		[0.01]	[0.01]	[0.02]	[0.13]	[0.03]	...	[0.14]	...	[0.56]	[0.67]

Note. $F_{3.6}$, $F_{4.5}$, $F_{5.8}$, and $F_{8.0}$ refer to fluxes from Spitzer-IRAC at 3.6, 4.5, 5.8, and 8.0 μm , respectively. $F_{7.7}$, $F_{11.1}$, $F_{19.1}$, $F_{24.4}$, $F_{31.5}$, and $F_{37.1}$ refer to fluxes from SOFIA-FORCAST at 7.7, 11.1, 19.1, 24.4, 31.5, and 37.5 μm , respectively. F_{70} , F_{100} , F_{160} , F_{250} , F_{350} , and F_{500} refer to fluxes from Herschel-PACS/SPIRE at 70, 100, 160, 250, 350, and 500 μm , respectively. †No Herschel-PACS 70 μm data is available and SOFIA-FORCAST 37 μm was used to find the optimal aperture (Section 3.1.1).

(This table is available in machine-readable form.)

Table A2
Parameters of the Five Best-fitted Models and the Average and Dispersion of Good Models

Source	χ^2	M_c (M_\odot)	Σ_{cl} (g cm^{-2})	R_{core} (pc)	m_* (M_\odot)	θ_{view} ($^\circ$)	A_V (mag)	M_{env} (M_\odot)	$\theta_{w,esc}$ (deg)	\dot{M}_{disk} (M_\odot/yr)	$L_{bol,iso}$ (L_\odot)	L_{bol} (L_\odot)
SOMA I												
AFGL 4029	0.33	80	0.100	0.21	8	68	0	61.51	27	5.0×10^{-5}	5.3×10^3	9.7×10^3
$d = 2.0$ kpc	0.36	80	0.100	0.21	12	74	0	46.52	40	5.4×10^{-5}	4.9×10^3	1.6×10^4
$R_{ap} = 12''.75$	0.39	100	0.100	0.23	16	89	29	53.01	45	6.2×10^{-5}	7.1×10^3	3.0×10^4
$R_{ap} = 0.12$ pc	0.40	40	0.316	0.08	8	44	0	22.29	36	9.2×10^{-5}	5.0×10^3	1.2×10^4
	0.42	50	0.316	0.09	12	58	0	21.56	46	1.0×10^{-4}	4.8×10^3	2.4×10^4
Average model	#567	59^{+36}_{-23}	$0.427^{+1.019}_{-0.301}$	$0.09^{+0.10}_{-0.05}$	13^{+10}_{-6}	57 ± 22	103 ± 102	21^{+32}_{-13}	44 ± 14	$1.4^{+1.8}_{-0.8} \times 10^{-4}$	$1.4^{+5.0}_{-1.1} \times 10^4$	$2.9^{+6.3}_{-2.0} \times 10^4$
AFGL 437	1.10	160	0.100	0.29	16	68	0	115.88	32	8.1×10^{-5}	1.5×10^4	3.3×10^4
$d = 2.0$ kpc	1.43	30	3.160	0.02	12	51	0	7.47	43	5.5×10^{-4}	1.5×10^4	4.9×10^4
$R_{ap} = 29''.50$	1.84	50	3.160	0.03	24	65	27	5.46	56	6.8×10^{-4}	2.0×10^4	1.9×10^5
$R_{ap} = 0.29$ pc	1.97	200	0.100	0.33	12	39	0	174.14	20	8.0×10^{-5}	1.5×10^4	2.0×10^4
	1.97	160	0.100	0.29	24	86	26	86.57	45	8.5×10^{-5}	1.9×10^4	7.8×10^4
Average model	#27	115^{+99}_{-53}	$0.235^{+0.800}_{-0.181}$	$0.16^{+0.30}_{-0.11}$	17^{+6}_{-4}	67 ± 16	10 ± 12	58^{+130}_{-40}	37 ± 10	$1.3^{+1.8}_{-0.8} \times 10^{-4}$	$1.6^{+0.2}_{-0.2} \times 10^4$	$4.8^{+4.5}_{-2.3} \times 10^4$
IRAS 07299	0.26	40	1.000	0.05	12	51	37	15.56	42	2.5×10^{-4}	1.1×10^4	4.5×10^4
$d = 1.7$ kpc	0.31	80	0.316	0.12	16	68	14	41.63	42	1.5×10^{-4}	9.7×10^3	4.2×10^4
$R_{ap} = 7''.50$	0.33	50	1.000	0.05	16	65	7	16.19	48	2.8×10^{-4}	8.6×10^3	6.7×10^4
$R_{ap} = 0.06$ pc	0.33	30	3.160	0.02	12	58	39	7.47	43	5.5×10^{-4}	1.1×10^4	4.9×10^4
	0.44	80	1.000	0.07	24	77	3	25.07	52	3.5×10^{-4}	9.9×10^3	1.2×10^5
Average model	#106	53^{+24}_{-17}	$1.594^{+2.033}_{-0.894}$	$0.04^{+0.03}_{-0.02}$	15^{+7}_{-5}	66 ± 16	28 ± 30	19^{+17}_{-9}	42 ± 10	$4.2^{+3.2}_{-1.8} \times 10^{-4}$	$1.2^{+0.4}_{-0.3} \times 10^4$	$6.5^{+6.6}_{-3.3} \times 10^4$
G35.20-0.74	1.66	160	0.316	0.17	12	29	29	135.26	20	1.8×10^{-4}	2.8×10^4	3.8×10^4
$d = 2.2$ kpc	1.68	160	0.316	0.17	16	39	32	124.70	26	2.0×10^{-4}	2.8×10^4	5.0×10^4
$R_{ap} = 18''.75$	1.85	160	0.316	0.17	24	51	58	97.59	37	2.2×10^{-4}	3.1×10^4	9.9×10^4
$R_{ap} = 0.20$ pc	1.93	80	3.160	0.04	12	39	26	58.05	22	8.4×10^{-4}	2.8×10^4	5.0×10^4
	1.97	200	0.316	0.19	16	29	64	162.47	22	2.2×10^{-4}	3.7×10^4	5.3×10^4
Average model	#231	122^{+67}_{-43}	$0.723^{+1.215}_{-0.453}$	$0.10^{+0.10}_{-0.05}$	19^{+9}_{-6}	62 ± 17	35 ± 36	72^{+64}_{-34}	33 ± 11	$3.5^{+3.3}_{-1.7} \times 10^{-4}$	$2.8^{+1.0}_{-0.7} \times 10^4$	$9.1^{+9.9}_{-4.7} \times 10^4$
G45.47+0.05	0.96	320	3.160	0.07	24	22	178	276.82	15	1.8×10^{-3}	3.3×10^5	3.1×10^5
$d = 8.4$ kpc	0.97	240	3.160	0.06	24	29	156	194.50	18	1.6×10^{-3}	2.6×10^5	3.1×10^5
$R_{ap} = 15''.00$	1.04	240	3.160	0.06	32	34	182	175.32	23	1.9×10^{-3}	3.2×10^5	5.0×10^5
$R_{ap} = 0.61$ pc	1.05	400	1.000	0.15	24	22	98	347.96	16	7.7×10^{-4}	1.9×10^5	2.0×10^5
	1.07	320	3.160	0.07	16	22	3	293.14	12	1.4×10^{-3}	1.0×10^5	1.1×10^5
Average model	#330	318^{+126}_{-90}	$1.331^{+1.636}_{-0.734}$	$0.11^{+0.08}_{-0.05}$	35^{+18}_{-12}	61 ± 18	88 ± 47	235^{+100}_{-70}	25 ± 8	$1.0^{+0.6}_{-0.4} \times 10^{-3}$	$1.6^{+0.6}_{-0.4} \times 10^5$	$3.7^{+2.8}_{-1.6} \times 10^5$
IRAS 20126	0.83	80	0.316	0.12	16	86	16	41.63	42	1.5×10^{-4}	9.2×10^3	4.2×10^4
$d = 1.6$ kpc	1.81	120	0.316	0.14	24	83	63	57.10	47	1.8×10^{-4}	1.5×10^4	9.3×10^4
$R_{ap} = 12''.75$	1.83	40	3.160	0.03	16	55	130	10.27	44	6.8×10^{-4}	2.4×10^4	1.1×10^5
$R_{ap} = 0.10$ pc	2.11	40	3.160	0.03	12	44	115	17.69	35	6.5×10^{-4}	2.1×10^4	4.9×10^4
	2.17	100	0.316	0.13	16	58	55	61.06	36	1.6×10^{-4}	1.4×10^4	4.5×10^4
Average model	#17	91^{+31}_{-23}	$0.362^{+0.271}_{-0.155}$	$0.12^{+0.06}_{-0.04}$	19^{+4}_{-4}	77 ± 9	47 ± 30	44^{+22}_{-15}	44 ± 3	$1.7^{+0.8}_{-0.5} \times 10^{-4}$	$1.2^{+0.4}_{-0.3} \times 10^4$	$6.1^{+3.2}_{-2.1} \times 10^4$
Cep A	1.04	120	0.316	0.14	12	55	69	93.48	24	1.6×10^{-4}	2.0×10^4	3.6×10^4
$d = 0.7$ kpc	1.34	160	0.316	0.17	24	68	112	97.59	37	2.2×10^{-4}	2.8×10^4	9.9×10^4
$R_{ap} = 36''.25$	1.61	160	0.316	0.17	32	89	119	72.00	48	2.2×10^{-4}	2.5×10^4	1.7×10^5
$R_{ap} = 0.12$ pc	1.69	120	0.316	0.14	16	77	61	82.16	32	1.8×10^{-4}	1.7×10^4	4.6×10^4
	1.73	100	1.000	0.07	24	55	107	46.18	43	4.4×10^{-4}	2.5×10^4	1.3×10^5

Table A2
(Continued)

Source	χ^2	M_c (M_\odot)	Σ_{cl} (g cm^{-2})	R_{core} (pc)	m_* (M_\odot)	θ_{view} ($^\circ$)	A_V (mag)	M_{env} (M_\odot)	$\theta_{w,esc}$ (deg)	\dot{M}_{disk} (M_\odot/yr)	$L_{bol,iso}$ (L_\odot)	L_{bol} (L_\odot)
Average model	#106	107^{+45}_{-31}	$0.544^{+0.626}_{-0.291}$	$0.10^{+0.07}_{-0.04}$	16^{+6}_{-5}	71 ± 12	66 ± 31	67^{+37}_{-24}	32 ± 8	$2.6^{+1.7}_{-1.0} \times 10^{-4}$	$2.0^{+0.5}_{-0.4} \times 10^4$	$6.1^{+4.5}_{-2.6} \times 10^4$
NGC 7538	0.55	50	3.160	0.03	16	44	61	20.52	37	7.7×10^{-4}	4.7×10^4	1.1×10^5
$d = 2.6$ kpc	0.57	200	0.100	0.33	24	89	21	128.41	37	9.9×10^{-5}	2.7×10^4	8.1×10^4
$R_{ap} = 13''75$	0.60	60	3.160	0.03	12	34	25	37.85	27	7.6×10^{-4}	3.3×10^4	5.0×10^4
$R_{ap} = 0.18$ pc	0.78	50	3.160	0.03	12	39	0	27.72	30	7.1×10^{-4}	2.2×10^4	5.1×10^4
	0.92	200	0.100	0.33	32	89	35	101.23	48	9.9×10^{-5}	3.0×10^4	1.5×10^5
Average model	#55	122^{+90}_{-52}	$0.568^{+1.573}_{-0.417}$	$0.11^{+0.16}_{-0.06}$	27^{+14}_{-9}	67 ± 16	23 ± 19	50^{+50}_{-25}	46 ± 9	$3.0^{+3.7}_{-1.7} \times 10^{-4}$	$2.9^{+0.5}_{-0.5} \times 10^4$	$1.6^{+1.5}_{-0.8} \times 10^5$
SOMA II												
G45.12+0.13	15.29	240	3.160	0.06	32	29	0	175.32	23	1.9×10^{-3}	4.5×10^5	5.0×10^5
$d = 7.4$ kpc	15.30	480	1.000	0.16	96	48	0	237.78	43	1.3×10^{-3}	4.4×10^5	1.6×10^6
$R_{ap} = 47''00$	15.61	480	1.000	0.16	48	29	1	366.96	25	1.1×10^{-3}	4.5×10^5	5.4×10^5
$R_{ap} = 1.69$ pc	17.32	480	1.000	0.16	64	39	0	324.63	32	1.2×10^{-3}	3.6×10^5	8.4×10^5
	17.95	400	1.000	0.15	64	39	4	246.43	36	1.1×10^{-3}	4.2×10^5	8.2×10^5
Average model	#815	350^{+180}_{-105}	$0.906^{+1.724}_{-0.594}$	$0.14^{+0.14}_{-0.07}$	44^{+31}_{-18}	57 ± 21	23 ± 53	217^{+138}_{-84}	32 ± 13	$8.3^{+8.6}_{-4.2} \times 10^{-4}$	$2.4^{+4.5}_{-1.6} \times 10^5$	$4.9^{+5.1}_{-2.5} \times 10^5$
G309.92+0.48	1.66	480	1.000	0.16	96	51	20	237.78	43	1.3×10^{-3}	3.3×10^5	1.6×10^6
$d = 5.5$ kpc	1.70	240	3.160	0.06	32	39	6	175.32	23	1.9×10^{-3}	2.7×10^5	5.0×10^5
$R_{ap} = 17''75$	1.88	240	3.160	0.06	24	29	1	194.50	18	1.6×10^{-3}	2.6×10^5	3.1×10^5
$R_{ap} = 0.47$ pc	1.89	400	1.000	0.15	64	44	3	246.43	36	1.1×10^{-3}	2.7×10^5	8.2×10^5
	2.01	400	1.000	0.15	48	34	11	288.73	29	1.0×10^{-3}	3.0×10^5	5.3×10^5
Average model	#21	340^{+147}_{-102}	$1.550^{+1.798}_{-0.832}$	$0.11^{+0.08}_{-0.05}$	45^{+31}_{-18}	39 ± 9	14 ± 18	230^{+76}_{-57}	29 ± 9	$1.3^{+0.6}_{-0.4} \times 10^{-3}$	$3.0^{+0.7}_{-0.6} \times 10^5$	$6.1^{+4.7}_{-2.7} \times 10^5$
G35.58-0.03	0.82	480	3.160	0.09	24	29	11	440.54	12	2.0×10^{-3}	2.7×10^5	2.9×10^5
$d = 10.2$ kpc	1.04	400	3.160	0.08	24	39	8	361.65	13	1.9×10^{-3}	2.6×10^5	3.0×10^5
$R_{ap} = 16''00$	1.57	320	3.160	0.07	24	51	3	276.82	15	1.8×10^{-3}	2.3×10^5	3.1×10^5
$R_{ap} = 0.79$ pc	1.70	480	1.000	0.16	48	48	7	366.96	25	1.1×10^{-3}	2.4×10^5	5.4×10^5
	1.93	480	1.000	0.16	64	55	24	324.63	32	1.2×10^{-3}	2.6×10^5	8.4×10^5
Average model	#37	417^{+73}_{-62}	$2.245^{+1.581}_{-0.928}$	$0.10^{+0.04}_{-0.03}$	31^{+15}_{-10}	48 ± 12	10 ± 14	349^{+59}_{-50}	18 ± 7	$1.6^{+0.4}_{-0.3} \times 10^{-3}$	$2.5^{+0.2}_{-0.2} \times 10^5$	$3.9^{+1.9}_{-1.3} \times 10^5$
IRAS 16562	0.38	200	0.316	0.19	32	48	67	114.70	41	2.6×10^{-4}	5.5×10^4	1.8×10^5
$d = 1.7$ kpc	0.41	200	0.316	0.19	24	39	48	139.72	32	2.5×10^{-4}	4.8×10^4	1.0×10^5
$R_{ap} = 17''50$	0.45	100	3.160	0.04	16	29	119	68.61	23	1.1×10^{-3}	1.0×10^5	1.2×10^5
$R_{ap} = 0.14$ pc	0.46	120	1.000	0.08	16	29	90	88.34	25	4.5×10^{-4}	7.8×10^4	9.7×10^4
	0.47	240	0.316	0.20	48	58	86	104.17	50	2.9×10^{-4}	6.7×10^4	3.8×10^5
Average model	#279	164^{+92}_{-59}	$0.963^{+1.686}_{-0.613}$	$0.10^{+0.09}_{-0.05}$	32^{+24}_{-14}	63 ± 18	44 ± 39	78^{+50}_{-30}	40 ± 12	$5.6^{+6.1}_{-2.9} \times 10^{-4}$	$5.1^{+2.5}_{-1.7} \times 10^4$	$2.5^{+3.9}_{-1.5} \times 10^5$
G305.20+0.21	0.15	320	0.100	0.42	64	86	13	102.12	60	1.2×10^{-4}	6.2×10^4	6.0×10^5
$d = 4.1$ kpc	0.21	60	3.160	0.03	16	39	2	31.12	32	8.4×10^{-4}	5.8×10^4	1.1×10^5
$R_{ap} = 11''25$	0.47	160	3.160	0.05	64	68	0	22.88	61	1.3×10^{-3}	5.9×10^4	8.6×10^5
$R_{ap} = 0.22$ pc	0.48	100	3.160	0.04	32	48	48	36.92	42	1.2×10^{-3}	1.1×10^5	3.5×10^5
	0.53	80	3.160	0.04	24	44	45	35.12	37	1.1×10^{-3}	1.0×10^5	2.6×10^5
Average model	#106	213^{+142}_{-85}	$0.299^{+0.934}_{-0.227}$	$0.20^{+0.31}_{-0.12}$	34^{+16}_{-11}	64 ± 16	12 ± 15	108^{+124}_{-58}	41 ± 11	$2.5^{+3.7}_{-1.5} \times 10^{-4}$	$6.0^{+1.7}_{-1.3} \times 10^4$	$2.2^{+2.2}_{-1.1} \times 10^5$
G305.20+0.21A	0.20	320	0.316	0.23	12	22	98	293.02	13	2.2×10^{-4}	3.6×10^4	4.0×10^4
$d = 4.1$ kpc	0.21	320	0.316	0.23	16	13	237	283.06	16	2.5×10^{-4}	3.6×10^5	6.1×10^4
$R_{ap} = 10''00$	0.22	100	3.160	0.04	12	48	58	76.73	20	9.4×10^{-4}	2.9×10^4	5.2×10^4

Table A2
(Continued)

Source	χ^2	M_c (M_\odot)	Σ_{cl} (g cm^{-2})	R_{core} (pc)	m_* (M_\odot)	θ_{view} ($^\circ$)	A_V (mag)	M_{env} (M_\odot)	$\theta_{w,esc}$ (deg)	\dot{M}_{disk} (M_\odot/yr)	$L_{bol,iso}$ (L_\odot)	L_{bol} (L_\odot)
$R_{ap} = 0.20$ pc	0.22	120	3.160	0.05	12	29	120	98.54	18	9.6×10^{-4}	4.0×10^4	5.2×10^4
	0.23	240	0.316	0.20	12	68	80	216.44	15	2.0×10^{-4}	3.1×10^4	4.1×10^4
Average model	#1520	174^{+130}_{-74}	$0.817^{+1.364}_{-0.511}$	$0.11^{+0.11}_{-0.05}$	25^{+24}_{-12}	57 ± 22	168 ± 100	97^{+101}_{-50}	33 ± 15	$4.6^{+4.5}_{-2.3} \times 10^{-4}$	$8.1^{+25.2}_{-6.1} \times 10^4$	$1.5^{+3.2}_{-1.0} \times 10^5$
G49.270.34	1.73	480	0.100	0.51	24	22	222	417.72	21	1.4×10^{-4}	2.0×10^5	8.7×10^4
$d = 5.5$ kpc	1.90	400	0.100	0.47	24	29	192	331.01	24	1.3×10^{-4}	7.0×10^4	8.6×10^4
$R_{ap} = 24''.75$	1.94	320	0.100	0.42	32	29	257	228.39	34	1.3×10^{-4}	5.3×10^5	1.6×10^5
$R_{ap} = 0.67$ pc	1.96	80	3.160	0.04	16	29	237	50.01	27	9.5×10^{-4}	1.8×10^5	1.1×10^5
	1.96	240	0.316	0.20	16	22	173	205.72	20	2.3×10^{-4}	1.0×10^5	5.5×10^4
Average model	#972	197^{+167}_{-90}	$0.432^{+1.018}_{-0.303}$	$0.16^{+0.22}_{-0.09}$	26^{+24}_{-12}	56 ± 21	163 ± 94	112^{+126}_{-59}	35 ± 14	$3.0^{+3.3}_{-1.6} \times 10^{-4}$	$8.5^{+27.1}_{-6.4} \times 10^4$	$1.5^{+2.9}_{-1.0} \times 10^5$
G339.881.26	2.34	200	0.316	0.19	12	80	20	172.68	17	1.9×10^{-4}	2.8×10^4	4.0×10^4
$d = 2.1$ kpc	2.38	200	0.316	0.19	24	86	73	139.72	32	2.5×10^{-4}	3.7×10^4	1.0×10^5
$R_{ap} = 20''.25$	2.43	200	0.316	0.19	16	83	36	162.47	22	2.2×10^{-4}	3.0×10^4	5.3×10^4
$R_{ap} = 0.21$ pc	2.50	240	0.316	0.20	48	71	134	104.17	50	2.9×10^{-4}	5.5×10^4	3.8×10^5
	2.53	240	0.316	0.20	12	86	19	216.44	15	2.0×10^{-4}	3.1×10^4	4.1×10^4
Average model	#322	180^{+108}_{-68}	$0.576^{+0.764}_{-0.328}$	$0.13^{+0.11}_{-0.06}$	22^{+20}_{-11}	65 ± 16	74 ± 55	110^{+88}_{-49}	31 ± 14	$3.5^{+2.9}_{-1.6} \times 10^{-4}$	$4.0^{+1.9}_{-1.3} \times 10^4$	$1.2^{+2.4}_{-0.8} \times 10^5$
SOMA III												
S235	1.09	10	3.160	0.01	2	39	0	5.65	35	1.8×10^{-4}	1.4×10^3	2.6×10^3
$d = 1.8$ kpc	2.97	50	0.316	0.09	16	80	0	7.84	68	7.1×10^{-5}	1.4×10^3	3.1×10^4
$R_{ap} = 7''.00$	3.55	20	3.160	0.02	4	39	0	11.60	34	3.1×10^{-4}	1.6×10^3	3.3×10^3
$R_{ap} = 0.06$ pc	5.59	60	1.000	0.06	24	89	31	4.87	71	1.9×10^{-4}	2.1×10^3	9.3×10^4
	5.76	80	1.000	0.07	32	89	33	2.70	79	1.4×10^{-4}	1.6×10^3	1.6×10^5
Average model	#5	30^{+33}_{-16}	$0.794^{+2.008}_{-0.569}$	$0.05^{+0.08}_{-0.03}$	8^{+13}_{-5}	64 ± 20	2 ± 4	8^{+2}_{-2}	54 ± 16	$1.2^{+1.2}_{-0.6} \times 10^{-4}$	$1.4^{+0.1}_{-0.1} \times 10^3$	$1.2^{+3.2}_{-0.9} \times 10^4$
IRAS 22198	6.05	10	3.160	0.01	4	62	69	1.65	56	1.9×10^{-4}	2.9×10^2	1.9×10^3
$d = 0.8$ kpc	9.05	10	1.000	0.02	2	44	51	5.33	39	7.5×10^{-5}	2.6×10^2	7.6×10^2
$R_{ap} = 6''.25$	13.15	10	0.316	0.04	1	34	24	7.50	28	2.5×10^{-5}	1.4×10^2	2.6×10^2
$R_{ap} = 0.02$ pc	13.23	10	0.316	0.04	0	22	38	8.75	18	1.9×10^{-5}	1.7×10^2	1.9×10^2
	13.33	10	1.000	0.02	4	74	47	1.29	59	7.7×10^{-5}	1.3×10^2	1.1×10^3
Average model	#7	10^{+0}_{-0}	$2.681^{+1.461}_{-0.945}$	$0.01^{+0.00}_{-0.00}$	4^{+1}_{-1}	67 ± 13	41 ± 18	2^{+1}_{-1}	54 ± 6	$1.7^{+0.7}_{-0.5} \times 10^{-4}$	$2.1^{+0.5}_{-0.4} \times 10^2$	$1.6^{+0.7}_{-0.5} \times 10^3$
NGC 2071	2.71	10	3.160	0.01	4	62	0	1.65	56	1.9×10^{-4}	2.9×10^2	1.9×10^3
$d = 0.4$ kpc	8.62	10	1.000	0.02	2	44	0	5.33	39	7.5×10^{-5}	2.6×10^2	7.6×10^2
$R_{ap} = 11''.50$	13.50	10	1.000	0.02	4	65	0	1.29	59	7.7×10^{-5}	1.7×10^2	1.1×10^3
$R_{ap} = 0.02$ pc	17.96	10	0.316	0.04	0	22	0	8.75	18	1.9×10^{-5}	1.7×10^2	1.9×10^2
	19.31	10	1.000	0.02	1	29	26	7.78	25	6.0×10^{-5}	5.6×10^2	7.7×10^2
Average model	#2	10^{+0}_{-0}	$3.160^{+0.000}_{-0.000}$	$0.01^{+0.00}_{-0.00}$	4^{+0}_{-0}	60 ± 2	26 ± 26	2^{+0}_{-0}	56 ± 0	$1.9^{+0.0}_{-0.0} \times 10^{-4}$	$3.8^{+1.7}_{-1.2} \times 10^2$	$1.9^{+0.0}_{-0.0} \times 10^3$
Cep E	2.09	10	1.000	0.02	4	89	49	1.29	59	7.7×10^{-5}	1.1×10^2	1.1×10^3
$d = 0.7$ kpc	2.35	10	0.316	0.04	2	55	4	4.96	43	3.0×10^{-5}	7.2×10^1	2.8×10^2
$R_{ap} = 8''.50$	6.28	10	0.316	0.04	1	34	53	7.50	28	2.5×10^{-5}	1.4×10^2	2.6×10^2
$R_{ap} = 0.03$ pc	11.84	10	0.316	0.04	0	22	84	8.75	18	1.9×10^{-5}	1.7×10^2	1.9×10^2
	12.94	10	3.160	0.01	4	55	359	1.65	56	1.9×10^{-4}	1.5×10^3	1.9×10^3
Average model	#15	10^{+0}_{-0}	$0.631^{+0.501}_{-0.279}$	$0.03^{+0.01}_{-0.01}$	3^{+1}_{-1}	70 ± 11	47 ± 40	2^{+1}_{-1}	53 ± 8	$5.3^{+3.2}_{-2.0} \times 10^{-5}$	$10.0^{+4.1}_{-2.9} \times 10^1$	$6.6^{+6.7}_{-3.3} \times 10^2$
L1206A	0.75	40	1.000	0.05	4	39	0	31.54	23	1.7×10^{-4}	1.2×10^3	2.2×10^3

Table A2
(Continued)

Source	χ^2	M_c (M_\odot)	Σ_{cl} (g cm^{-2})	R_{core} (pc)	m_* (M_\odot)	θ_{view} ($^\circ$)	A_V (mag)	M_{env} (M_\odot)	$\theta_{w,esc}$ (deg)	\dot{M}_{disk} (M_\odot/yr)	$L_{bol,iso}$ (L_\odot)	L_{bol} (L_\odot)
$d = 0.8$ kpc	0.81	30	1.000	0.04	2	29	17	25.89	19	1.2×10^{-4}	1.2×10^3	1.7×10^3
$R_{ap} = 6''50$	0.93	40	1.000	0.05	2	22	67	35.79	16	1.3×10^{-4}	1.6×10^3	2.0×10^3
$R_{ap} = 0.02$ pc	1.01	30	1.000	0.04	4	44	4	21.60	28	1.5×10^{-4}	9.2×10^2	2.0×10^3
	1.03	20	3.160	0.02	2	29	212	15.99	22	2.4×10^{-4}	2.6×10^3	3.9×10^3
Average model	#46	24_{-5}^{+7}	$1.823_{-0.803}^{+1.436}$	$0.03_{-0.01}^{+0.01}$	3_{-2}^{+3}	49 ± 18	110 ± 84	13_{-7}^{+15}	30 ± 13	$2.0_{-0.6}^{+0.8} \times 10^{-4}$	$1.7_{-0.4}^{+0.6} \times 10^3$	$4.3_{-2.1}^{+4.0} \times 10^3$
L1206B	2.18	10	0.316	0.04	4	77	32	0.63	68	2.4×10^{-5}	4.9×10^1	6.7×10^2
$d = 0.8$ kpc	4.60	30	1.000	0.04	0	13	134	29.10	8	6.0×10^{-5}	1.0×10^3	4.2×10^2
$R_{ap} = 8''00$	5.67	10	0.316	0.04	2	44	186	4.96	43	3.0×10^{-5}	3.3×10^2	2.8×10^2
$R_{ap} = 0.03$ pc	6.18	20	1.000	0.03	0	13	237	19.18	10	5.4×10^{-5}	1.7×10^3	4.5×10^2
	6.39	10	0.316	0.04	1	29	246	7.50	28	2.5×10^{-5}	5.3×10^2	2.6×10^2
Average model	#20	10_{-0}^{+0}	$0.316_{-0.000}^{+0.000}$	$0.04_{-0.00}^{+0.00}$	4_{-0}^{+0}	57 ± 21	101 ± 57	1_{-0}^{+0}	68 ± 0	$2.4_{-0.0}^{+0.0} \times 10^{-5}$	$3.1_{-2.4}^{+11.4} \times 10^2$	$6.7_{-0.0}^{+0.0} \times 10^2$
IRAS 22172 _{mir1}	0.15	30	0.100	0.13	1	13	73	27.26	15	1.5×10^{-5}	8.7×10^2	1.7×10^2
$d = 2.4$ kpc	0.15	60	0.100	0.18	1	13	57	57.46	10	1.8×10^{-5}	6.1×10^2	2.0×10^2
$R_{ap} = 8''00$	0.15	40	0.100	0.15	1	13	63	38.03	12	1.6×10^{-5}	6.8×10^2	1.7×10^2
$R_{ap} = 0.09$ pc	0.16	30	0.100	0.13	2	22	67	24.61	23	2.0×10^{-5}	8.0×10^2	2.4×10^2
	0.16	20	0.100	0.10	4	48	47	9.85	43	2.1×10^{-5}	3.4×10^2	6.8×10^2
Average model	#6240	85_{-53}^{+140}	$0.822_{-0.546}^{+1.625}$	$0.07_{-0.03}^{+0.07}$	7_{-5}^{+20}	57 ± 21	425 ± 286	52_{-38}^{+133}	26 ± 18	$2.1_{-1.6}^{+6.1} \times 10^{-4}$	$8.1_{-7.5}^{+92.8} \times 10^3$	$1.3_{-1.2}^{+15.2} \times 10^4$
IRAS 22172 _{mir2}	0.57	20	0.316	0.06	8	77	11	1.63	66	4.4×10^{-5}	8.6×10^2	9.9×10^3
$d = 2.4$ kpc	0.65	100	0.316	0.13	32	86	27	4.49	81	5.0×10^{-5}	1.3×10^3	1.4×10^5
$R_{ap} = 26''75$	0.66	30	0.100	0.13	8	65	28	8.93	57	2.6×10^{-5}	1.2×10^3	6.3×10^3
$R_{ap} = 0.31$ pc	0.86	80	0.100	0.21	4	22	0	70.84	18	3.7×10^{-5}	9.0×10^2	8.5×10^2
	0.86	60	0.100	0.18	4	22	37	51.25	21	3.4×10^{-5}	2.1×10^3	8.9×10^2
Average model	#45	36_{-20}^{+45}	$0.300_{-0.197}^{+0.574}$	$0.08_{-0.04}^{+0.10}$	6_{-4}^{+10}	52 ± 30	49 ± 42	10_{-7}^{+23}	46 ± 22	$5.5_{-2.6}^{+4.9} \times 10^{-5}$	$2.1_{-1.3}^{+3.2} \times 10^3$	$5.2_{-4.4}^{+28.5} \times 10^3$
IRAS 221172 _{mir3}	0.18	10	1.000	0.02	4	62	31	1.29	59	7.7×10^{-5}	2.4×10^2	1.1×10^3
$d = 2.4$ kpc	0.19	40	0.100	0.15	2	22	48	35.65	19	2.2×10^{-5}	3.9×10^2	2.7×10^2
$R_{ap} = 7''75$	0.21	60	0.100	0.18	2	13	134	55.43	15	2.5×10^{-5}	1.7×10^3	3.5×10^2
$R_{ap} = 0.09$ pc	0.21	20	0.100	0.10	4	62	23	9.85	43	2.1×10^{-5}	2.3×10^2	6.8×10^2
	0.21	50	0.100	0.16	2	13	128	45.52	16	2.4×10^{-5}	1.6×10^3	3.1×10^2
Average model	#5778	85_{-53}^{+142}	$0.862_{-0.577}^{+1.744}$	$0.07_{-0.03}^{+0.06}$	7_{-5}^{+20}	57 ± 21	381 ± 313	51_{-37}^{+133}	27 ± 18	$2.3_{-1.7}^{+6.6} \times 10^{-4}$	$9.4_{-8.6}^{+102.5} \times 10^3$	$1.5_{-1.4}^{+16.8} \times 10^4$
IRAS 21391 _{bima2}	0.19	10	0.316	0.04	2	48	103	4.96	43	3.0×10^{-5}	9.0×10^1	2.8×10^2
$d = 0.8$ kpc	0.55	10	0.316	0.04	0	22	117	8.75	18	1.9×10^{-5}	1.7×10^2	1.9×10^2
$R_{ap} = 7''00$	0.55	10	1.000	0.02	4	62	204	1.29	59	7.7×10^{-5}	2.4×10^2	1.1×10^3
$R_{ap} = 0.03$ pc	0.58	10	0.316	0.04	1	34	102	7.50	28	2.5×10^{-5}	1.4×10^2	2.6×10^2
	0.62	10	3.160	0.01	4	86	101	1.65	56	1.9×10^{-4}	1.6×10^2	1.9×10^3
Average model	#121	10_{-2}^{+2}	$0.788_{-0.487}^{+1.275}$	$0.03_{-0.01}^{+0.02}$	2_{-1}^{+2}	66 ± 18	96 ± 97	4_{-2}^{+5}	39 ± 14	$5.7_{-3.5}^{+8.8} \times 10^{-5}$	$2.0_{-1.3}^{+3.6} \times 10^2$	$6.4_{-4.0}^{+10.4} \times 10^2$
IRAS 21391 _{bima3}	0.35	10	1.000	0.02	4	62	212	1.29	59	7.7×10^{-5}	2.4×10^2	1.1×10^3
$d = 0.8$ kpc	0.36	10	1.000	0.02	2	39	295	5.33	39	7.5×10^{-5}	1.0×10^3	7.6×10^2
$R_{ap} = 7''75$	0.48	10	0.316	0.04	2	51	69	4.96	43	3.0×10^{-5}	7.7×10^1	2.8×10^2
$R_{ap} = 0.03$ pc	0.49	10	0.316	0.04	0	22	120	8.75	18	1.9×10^{-5}	1.7×10^2	1.9×10^2
	0.51	10	0.316	0.04	1	34	106	7.50	28	2.5×10^{-5}	1.4×10^2	2.6×10^2
Average model	#1809	45_{-25}^{+57}	$2.091_{-0.980}^{+1.845}$	$0.03_{-0.01}^{+0.01}$	5_{-4}^{+13}	58 ± 21	489 ± 306	25_{-17}^{+51}	28 ± 16	$3.3_{-2.1}^{+5.9} \times 10^{-4}$	$6.8_{-6.0}^{+8.7} \times 10^3$	$1.2_{-1.1}^{+8.7} \times 10^4$

Table A2
(Continued)

Source	χ^2	M_c (M_\odot)	Σ_{cl} (g cm^{-2})	R_{core} (pc)	m_* (M_\odot)	θ_{view} ($^\circ$)	A_V (mag)	M_{env} (M_\odot)	$\theta_{w,esc}$ (deg)	\dot{M}_{disk} (M_\odot/yr)	$L_{bol,iso}$ (L_\odot)	L_{bol} (L_\odot)
IRAS 21391 _{mir48}	0.92	10	0.316	0.04	4	89	48	0.63	68	2.4×10^{-5}	2.9×10^1	6.7×10^2
$d = 0.8$ kpc	8.25	10	0.316	0.04	2	44	235	4.96	43	3.0×10^{-5}	3.3×10^2	2.8×10^2
$R_{ap} = 7''.75$	9.79	10	0.316	0.04	1	29	299	7.50	28	2.5×10^{-5}	5.3×10^2	2.6×10^2
$R_{ap} = 0.03$ pc	10.03	20	3.160	0.02	0	13	334	19.18	9	1.3×10^{-4}	2.8×10^3	8.6×10^2
	10.04	10	3.160	0.01	4	89	192	1.65	56	1.9×10^{-4}	1.6×10^2	1.9×10^3
Average model	#4	10_{-0}^{+0}	$0.316_{-0.000}^{+0.000}$	$0.04_{-0.00}^{+0.00}$	4_{-0}^{+0}	84 ± 3	60 ± 11	1_{-0}^{+0}	68 ± 0	$2.4_{-0.0}^{+0.0} \times 10^{-5}$	$3.3_{-0.5}^{+0.5} \times 10^1$	$6.7_{-0.0}^{+0.0} \times 10^2$

Note. For each source, the first five rows refer to the best five models taken from the 432 physical models, whereas the sixth row shows the average and dispersion of good model fits (see the text). The number next to the symbol # represents the number of models considered in the average of the good models. Upper and lower scripts in the row average models refer to the upper and lower errors.

(This table is available in machine-readable form.)

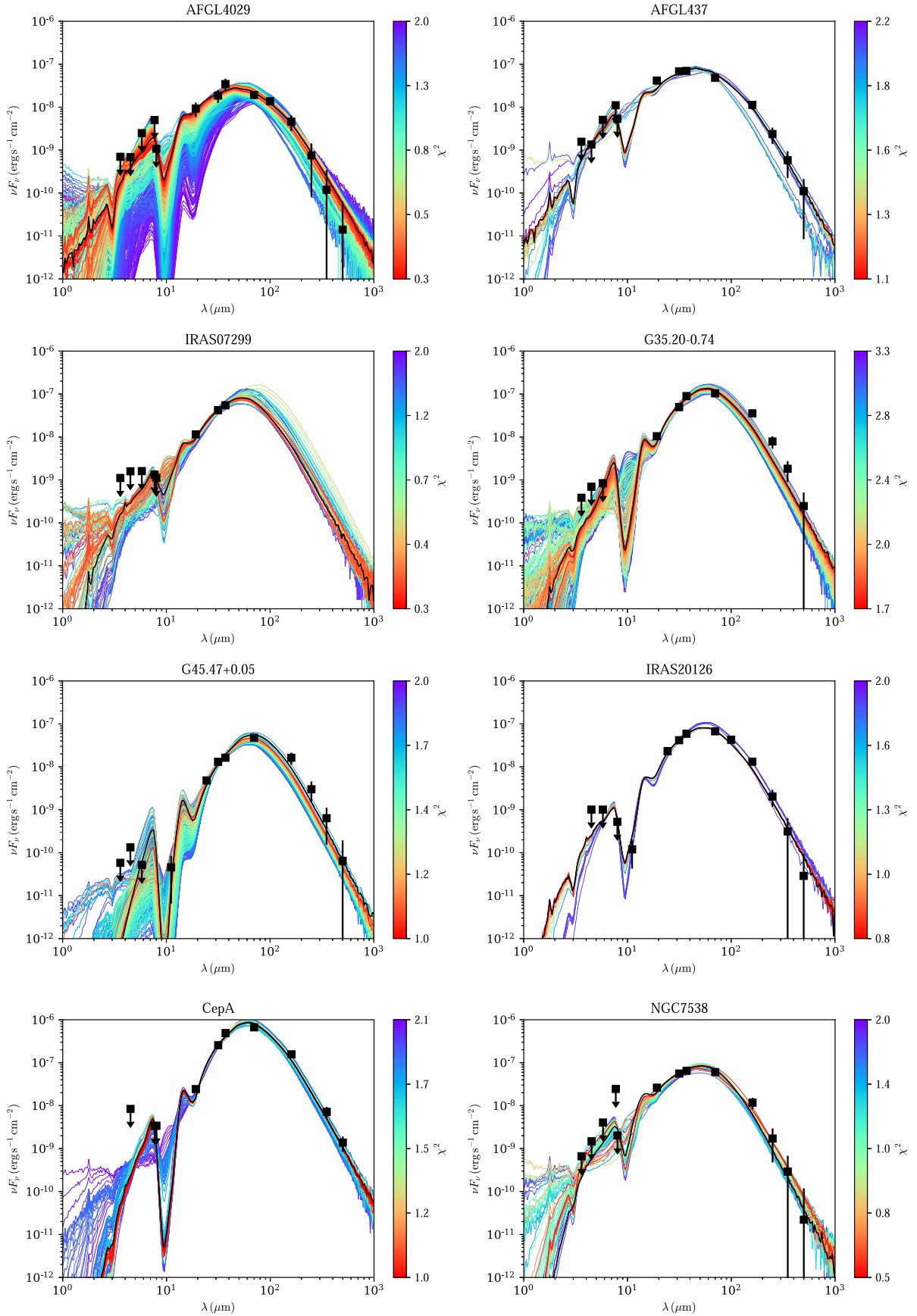


Figure A1. SOMA I sources reanalyzed with *sedcreator*. Protostar model fitting to the fixed aperture, background-subtracted SED data using the ZT model grid. For each source (noted on top of each plot), the best-fitting protostar model is shown with a black line, while all other good model fits (see the text) are shown with colored lines (red to blue with increasing χ^2). Flux values are those from Table A1. Note that the data at $\lesssim 8 \mu\text{m}$ are treated as upper limits (see the text). The resulting model parameters are listed in Table A2.

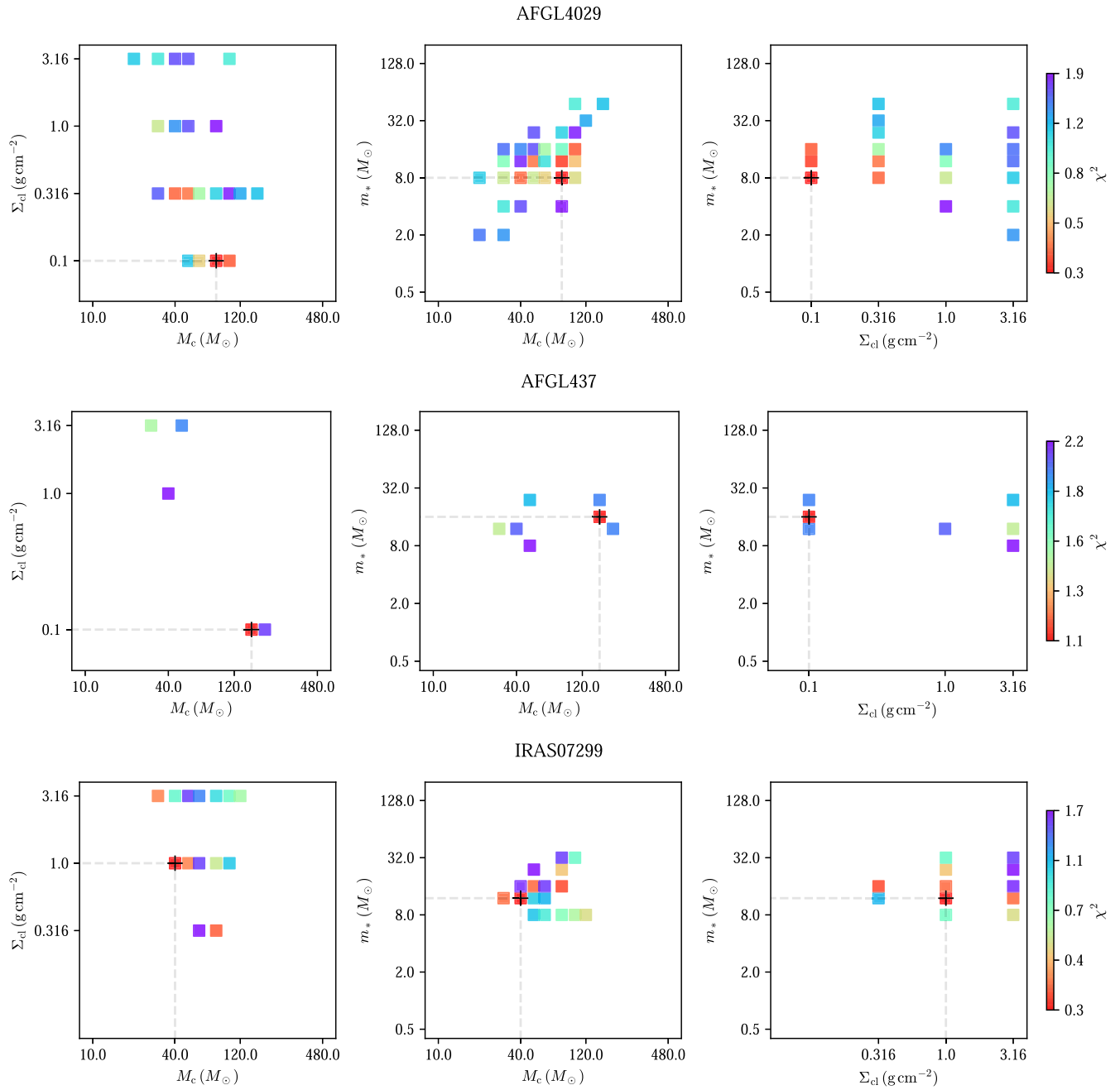
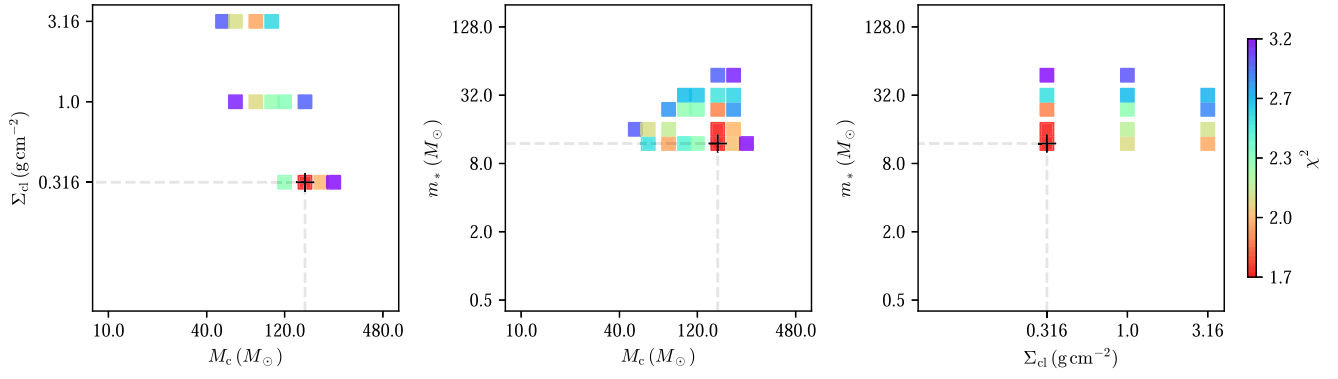
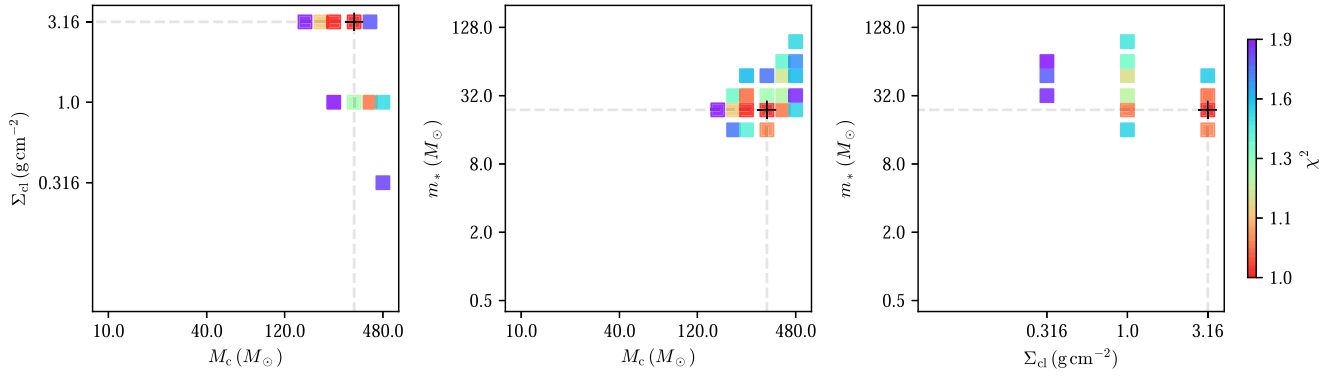


Figure A2. Diagrams of χ^2 distribution in $\Sigma_{\text{cl}} - M_c$ space (left column), $m_* - M_c$ space (center column), and $m_* - \Sigma_{\text{cl}}$ space (right column) for each source noted on top of each plot. The black cross represents the best model.

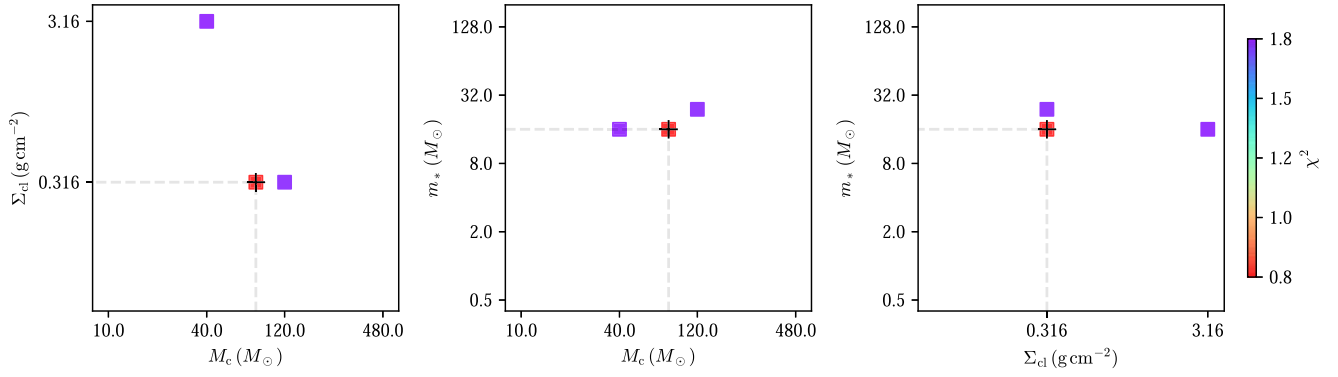
G35.20-0.74



G45.47+0.05



IRAS20126



CepA

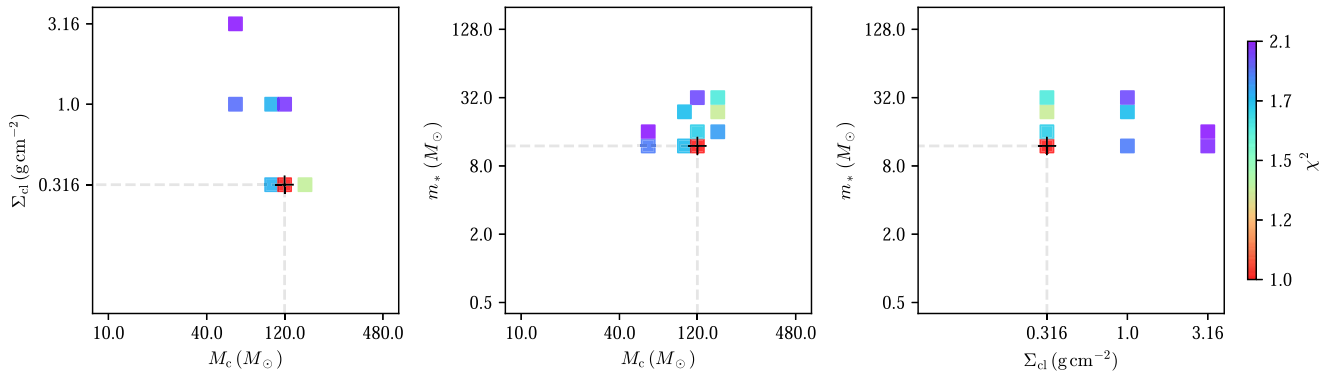


Figure A2. (Continued.)

NGC7538

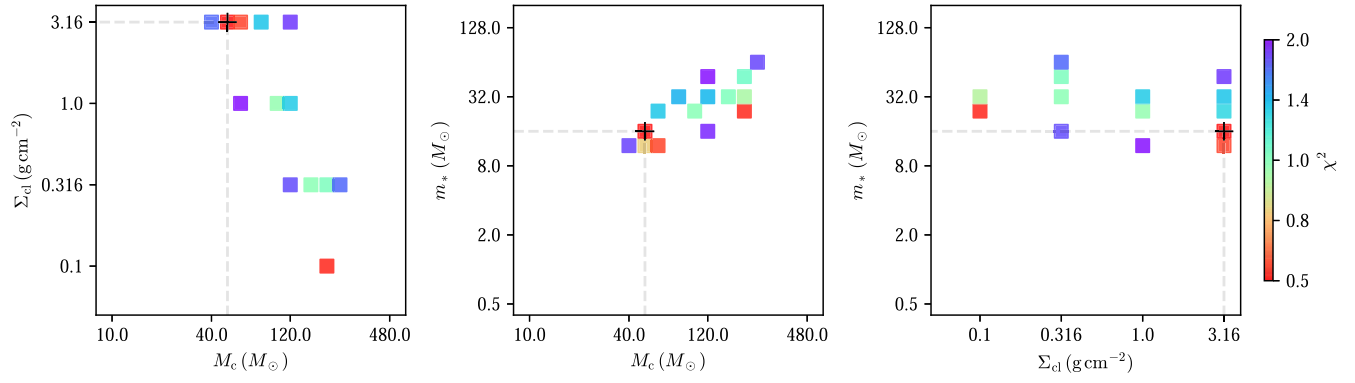


Figure A2. (Continued.)

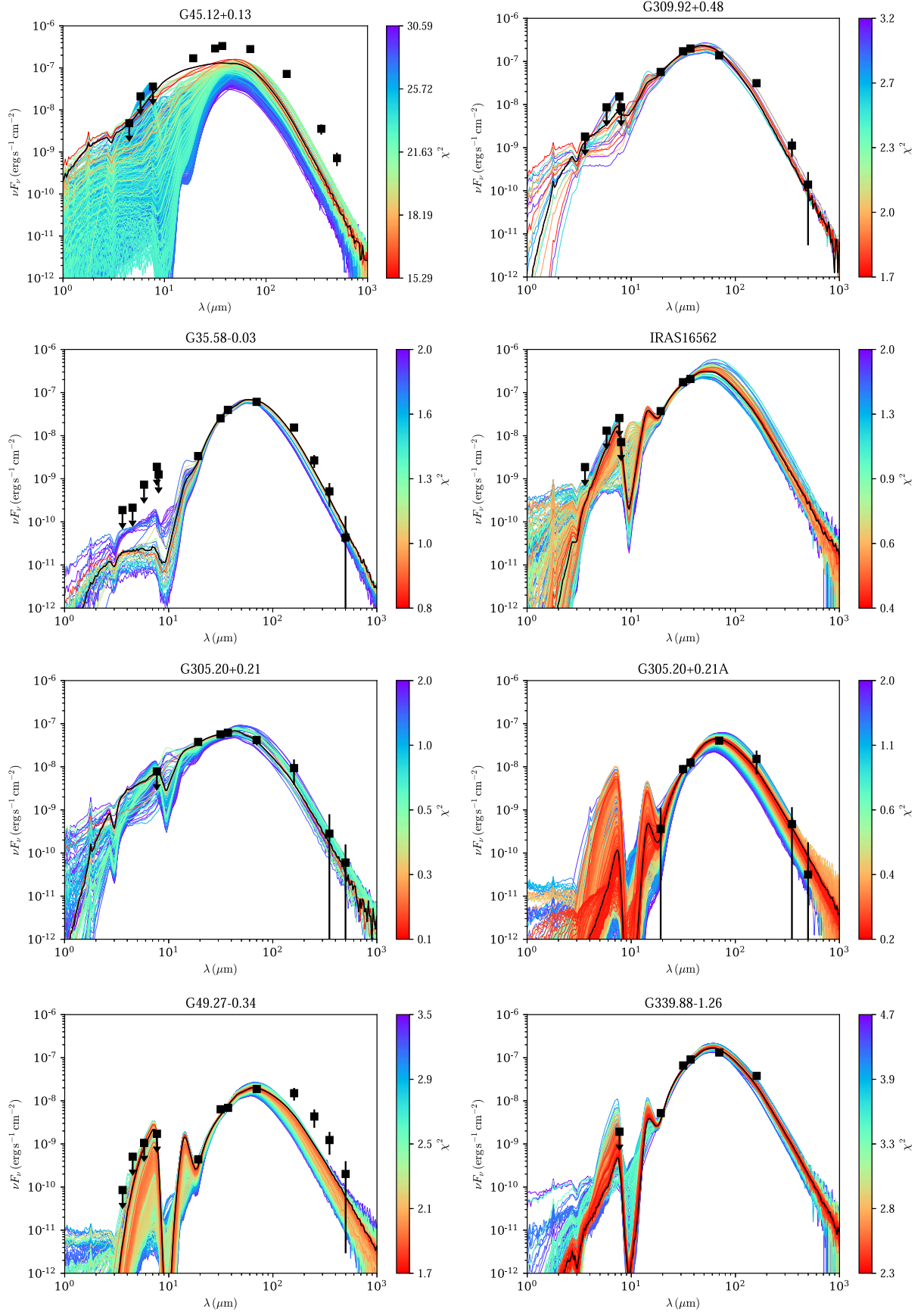


Figure A3. SOMA II sources reanalyzed with *sedcreator*. Protostar model fitting to the fixed aperture, background-subtracted SED data using the ZT model grid. For each source (noted on top of each plot), the best-fitting protostar model is shown with a black line, while all other good model fits (see the text) are shown with colored lines (red to blue with increasing χ^2). Flux values are those from Table A1. Note that the data at $\lesssim 8 \mu\text{m}$ are treated as upper limits (see the text). The resulting model parameters are listed in Table A2.

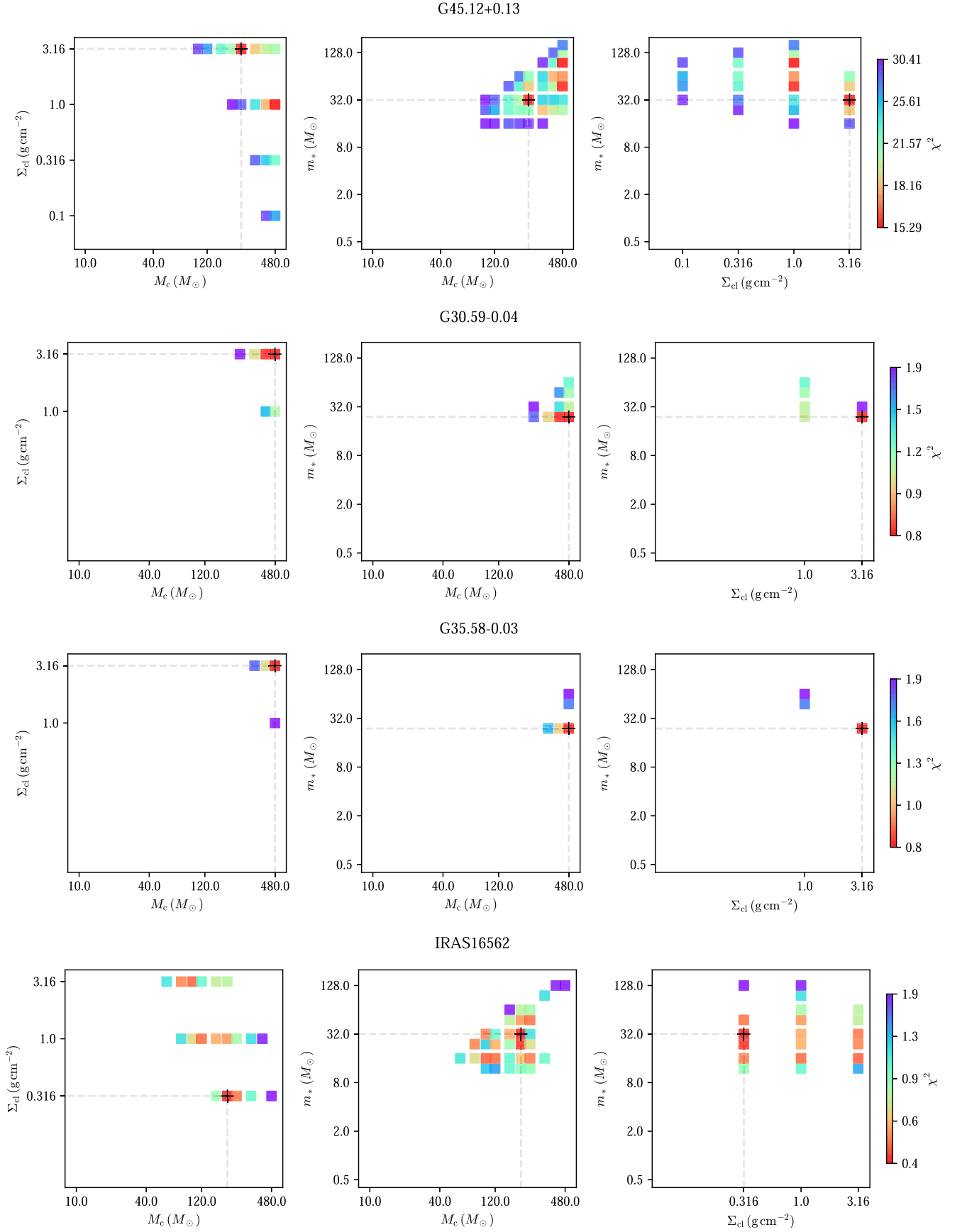
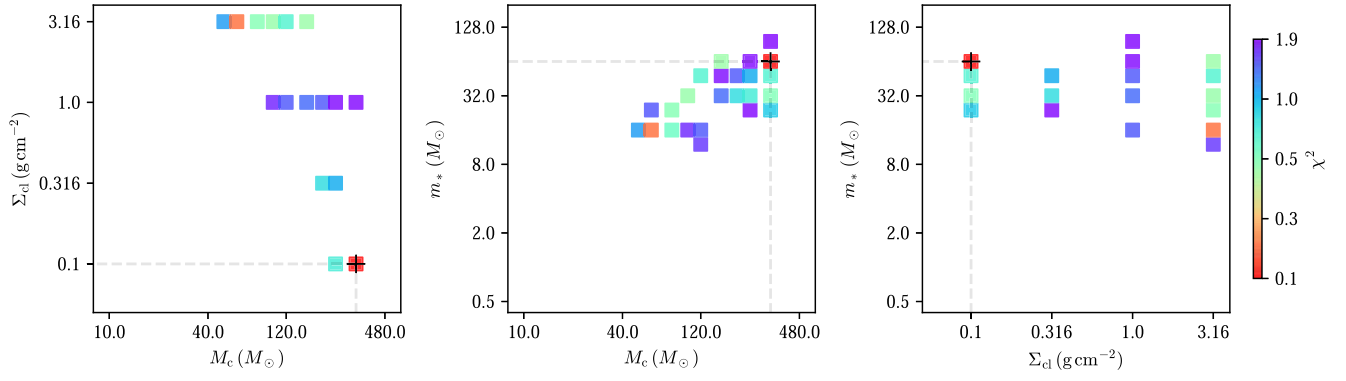
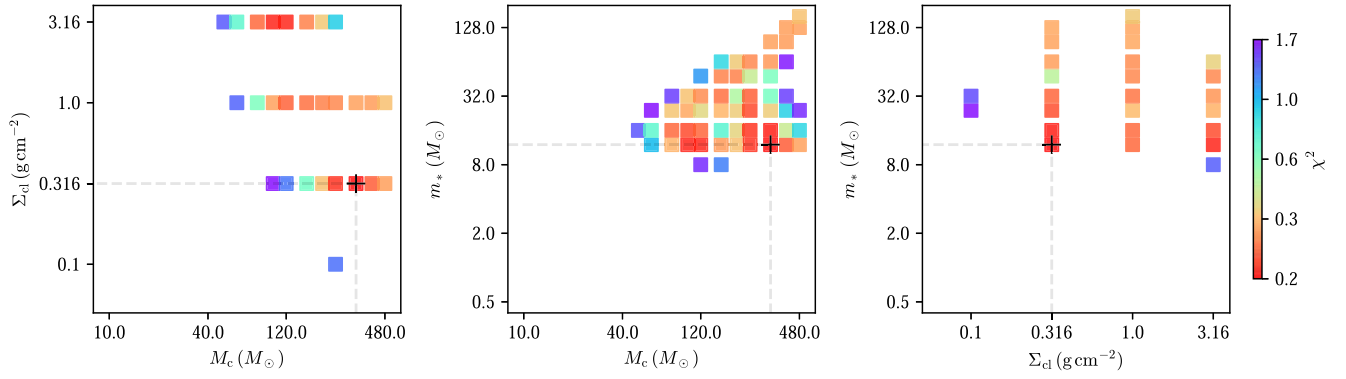


Figure A4. Diagrams of the χ^2 distribution in the $\Sigma_{\text{cl}}-M_c$ space (left column), m_*-M_c space (center column), and $m_*- \Sigma_{\text{cl}}$ space (right column) for each source noted on top of each plot. The black cross is the best model.

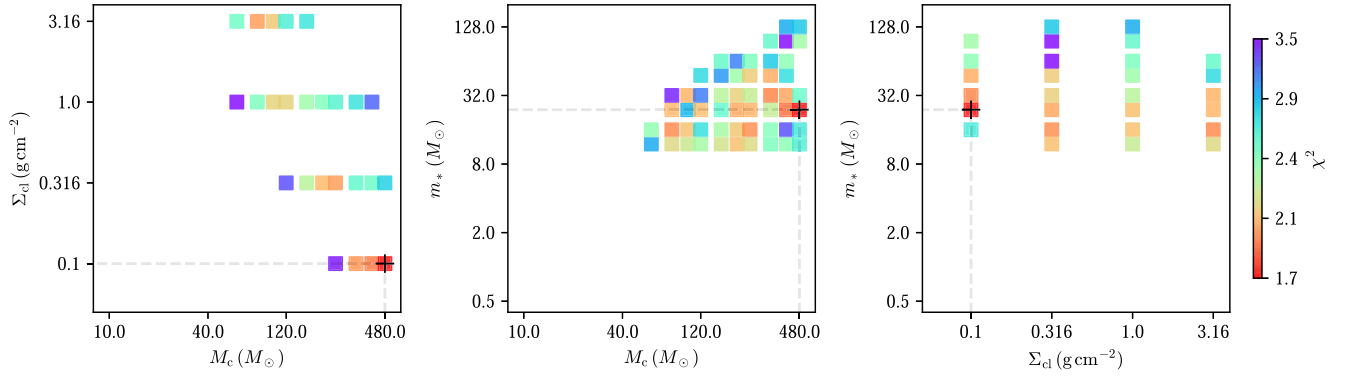
G305.20+0.21



G305.20+0.21A



G49.27-0.34



G339.88-1.26

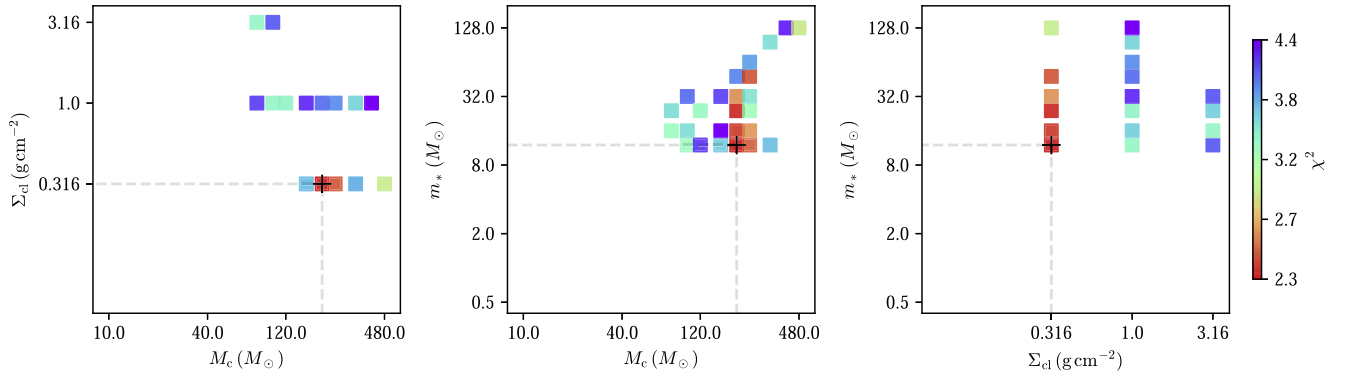


Figure A4. (Continued.)

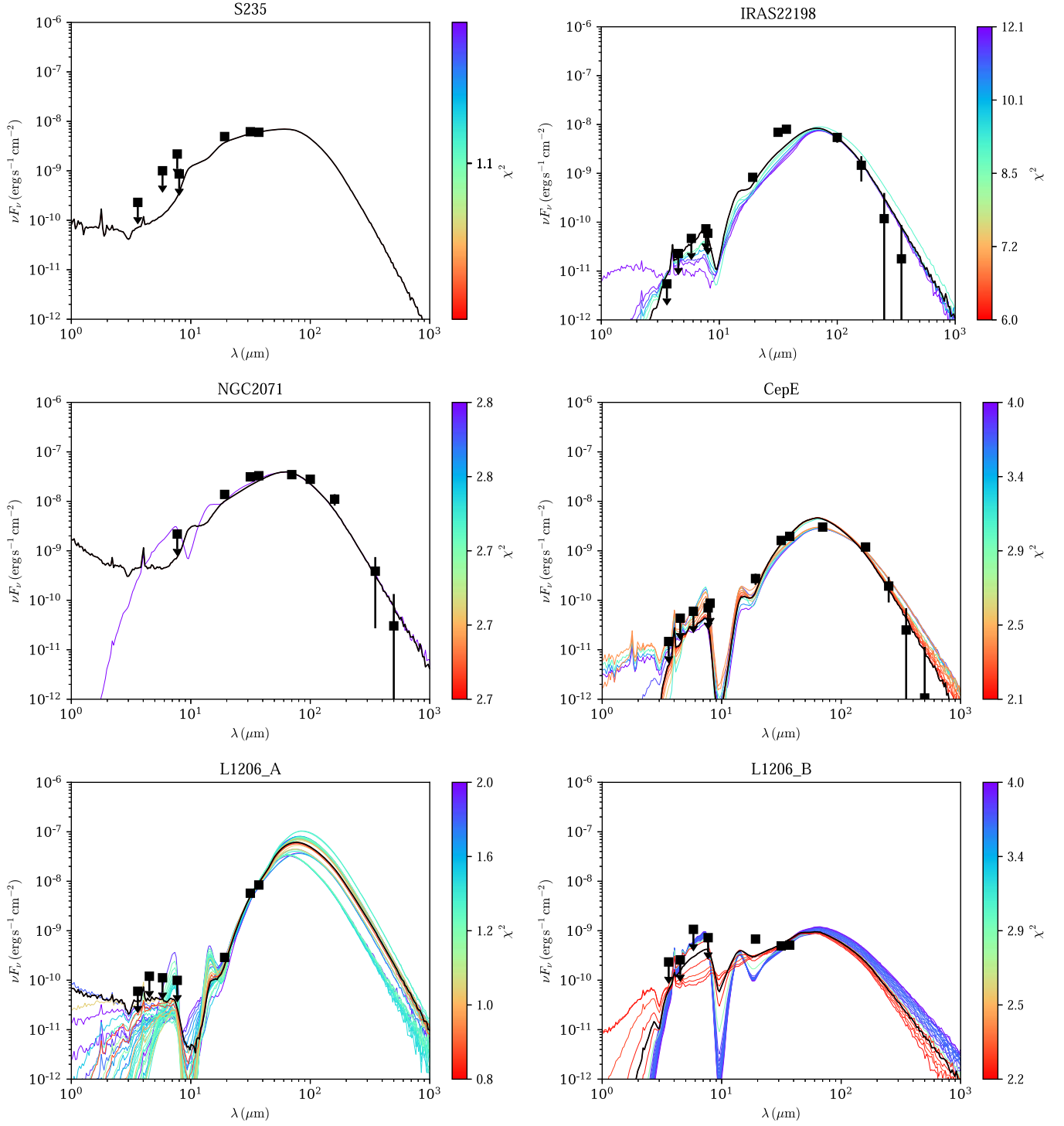


Figure A5. SOMA III sources reanalyzed with sedcreator. Protostar model fitting to the fixed aperture, background-subtracted SED data using the ZT model grid. For each source (noted on top of each plot), the best-fitting protostar model is shown with a black line, while all other good model fits (see the text) are shown with colored lines (red to blue with increasing χ^2). Flux values are those from Table A1. Note that the data at $\lesssim 8 \mu\text{m}$ are treated as upper limits (see the text). The resulting model parameters are listed in Table A2.

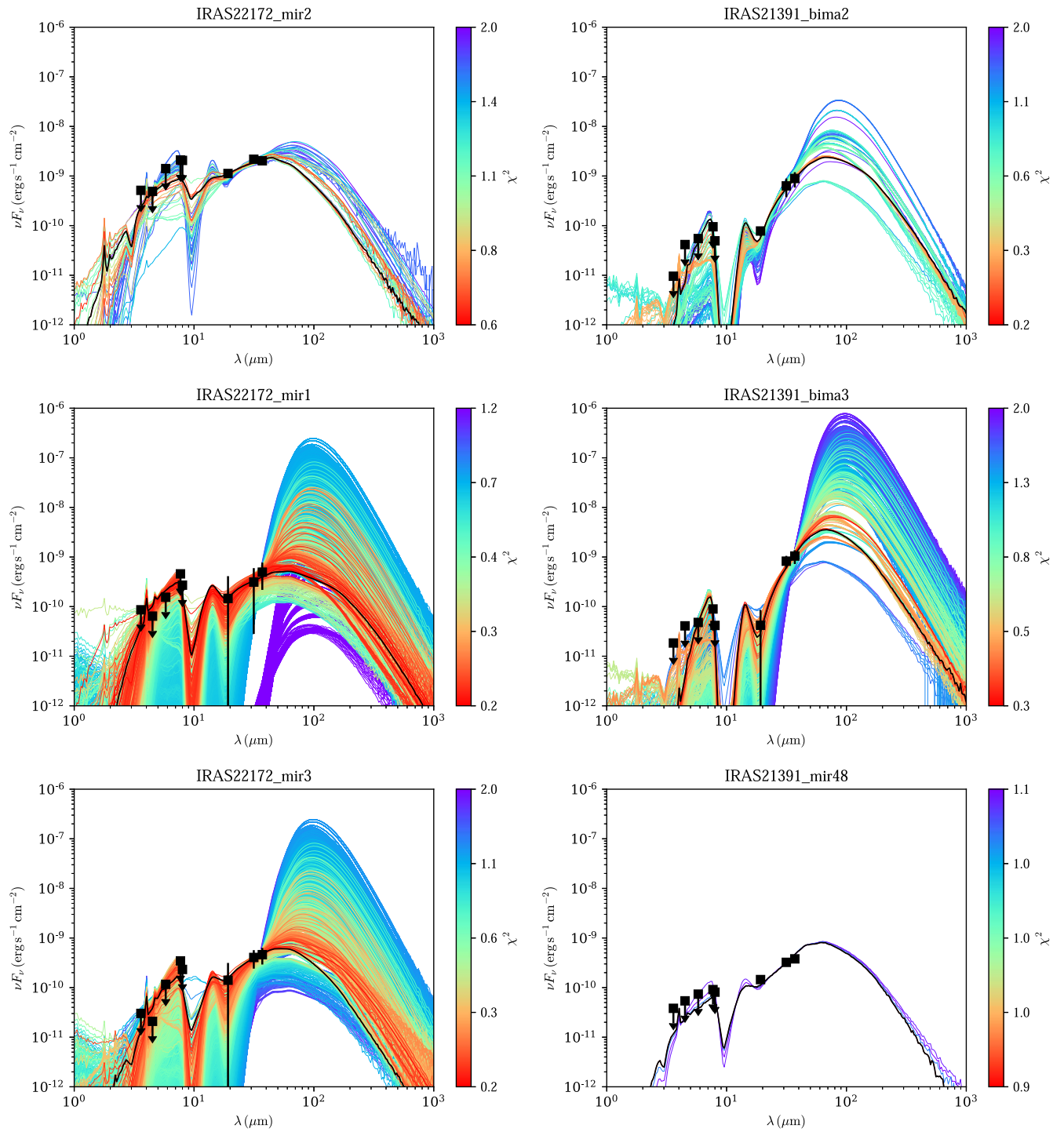


Figure A5. (Continued.)

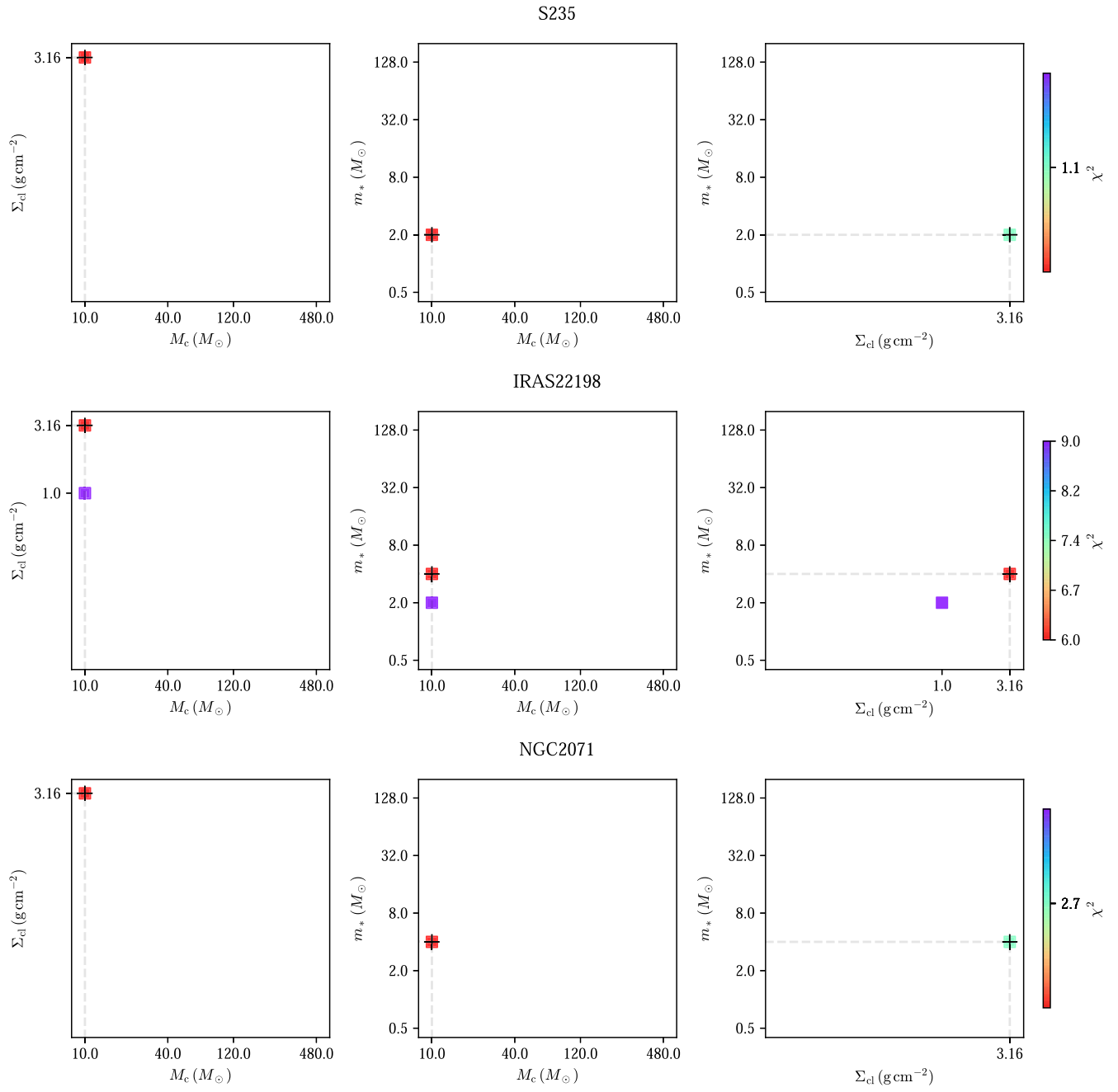


Figure A6. Diagrams of χ^2 distribution in $\Sigma_{\text{cl}}-M_c$ space (left column), m_*-M_c space (center columns), and $m_*- \Sigma_{\text{cl}}$ space (right column) for each source noted on top of each plot. The black cross represents the best model.

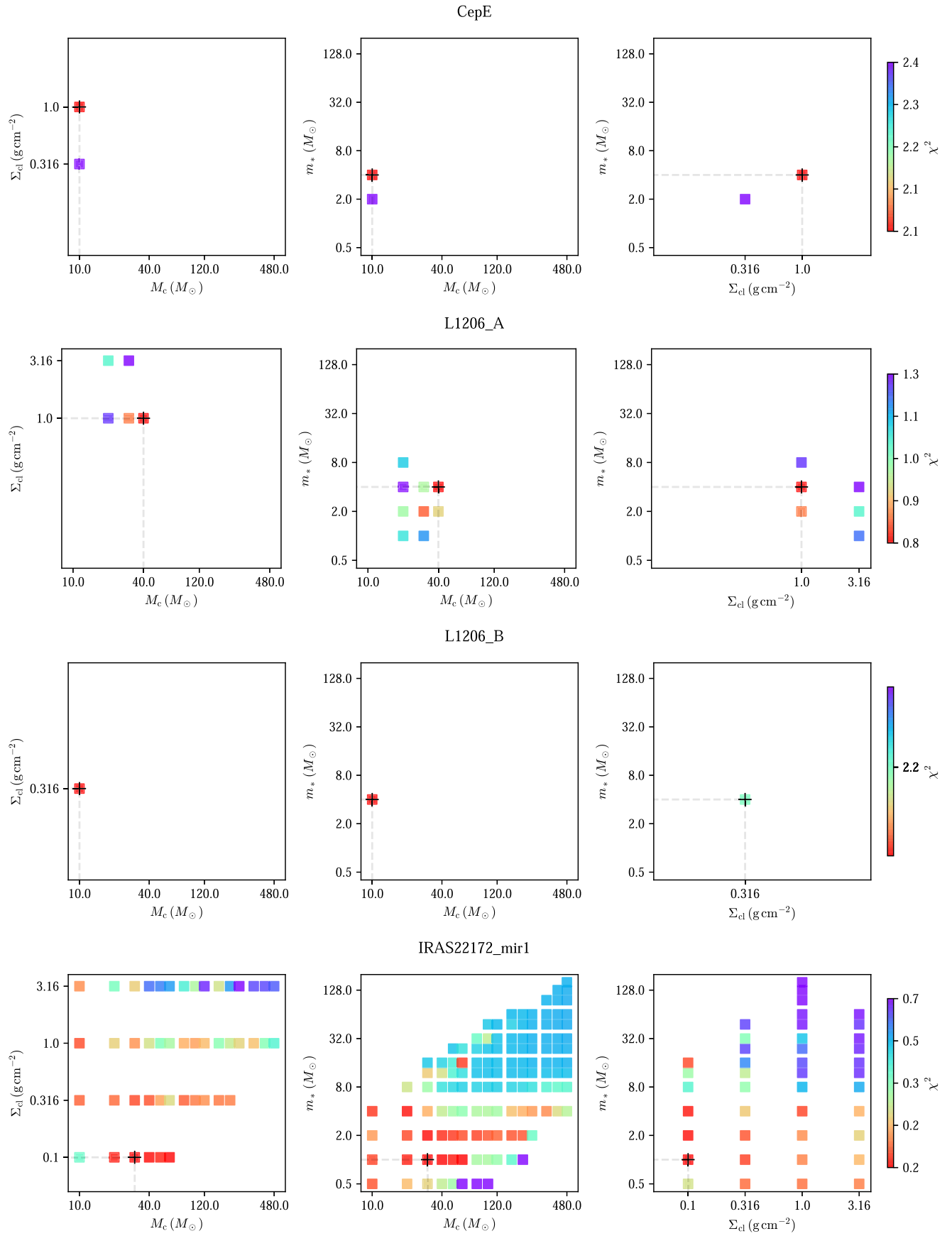
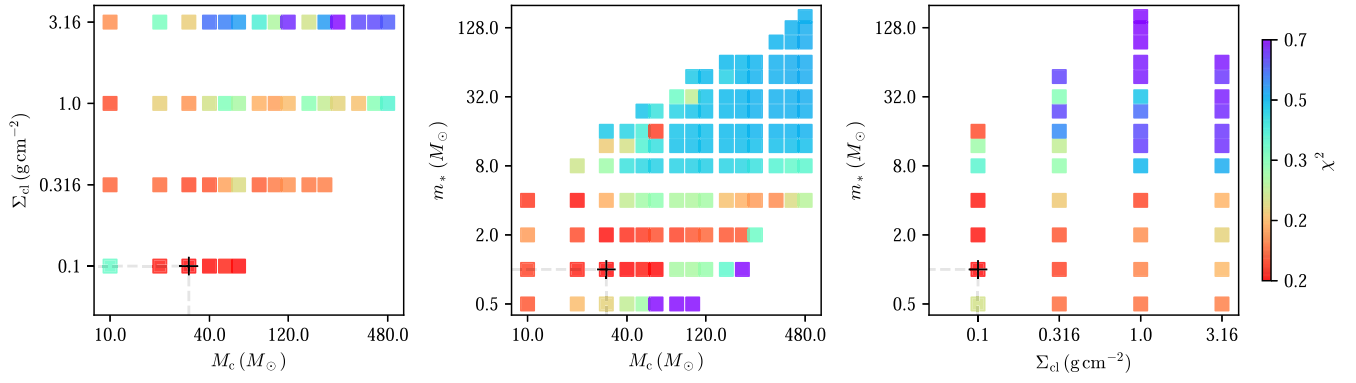
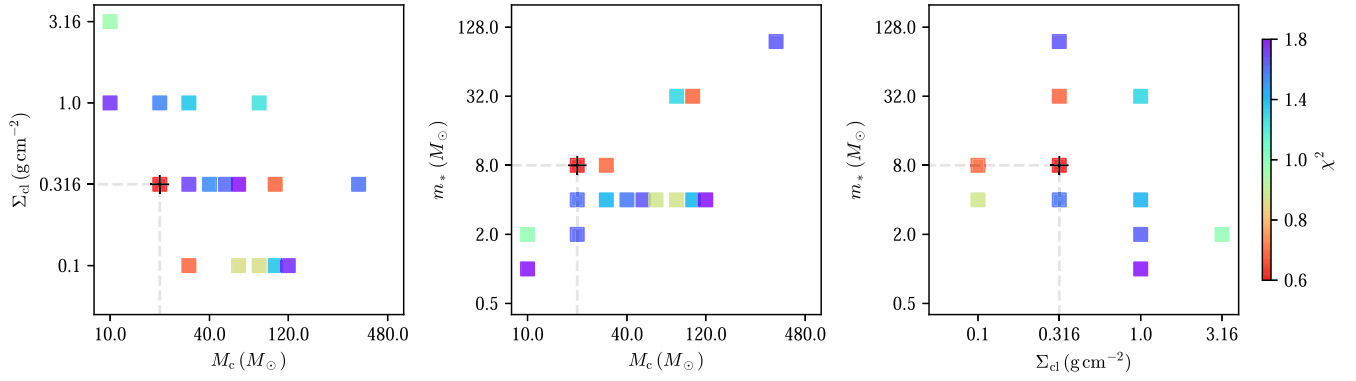


Figure A6. (Continued.)

IRAS22172_mir1



IRAS22172_mir2



IRAS22172_mir3

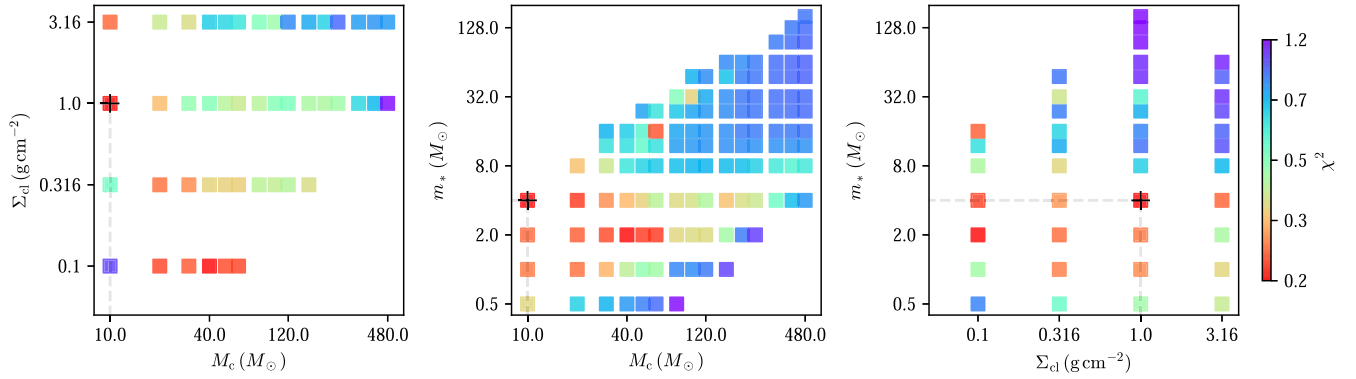
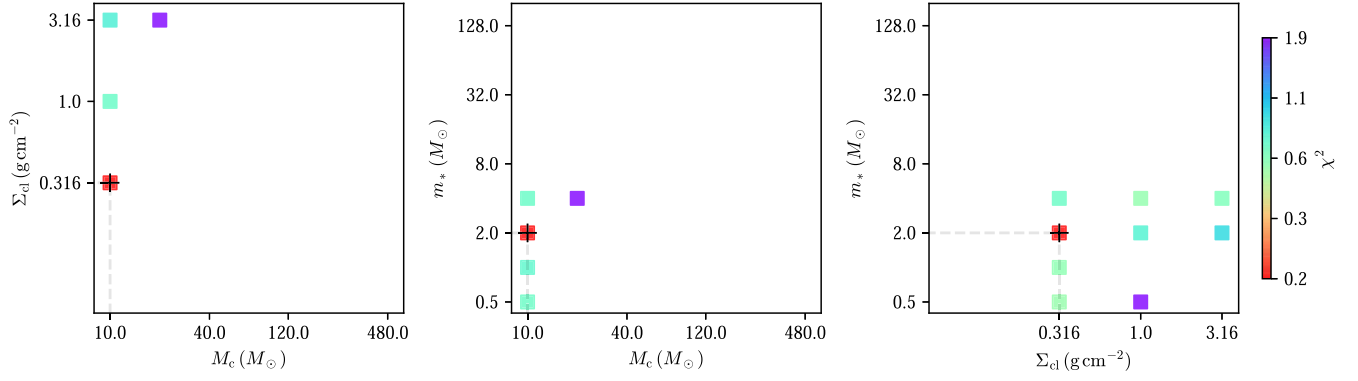
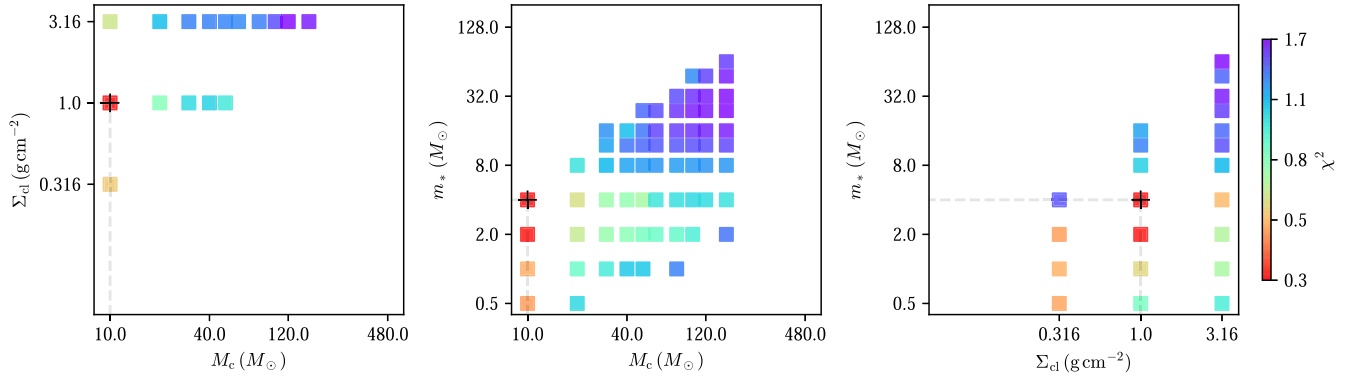


Figure A6. (Continued.)

IRAS21391_bima2



IRAS21391_bima3



IRAS21391_mir48

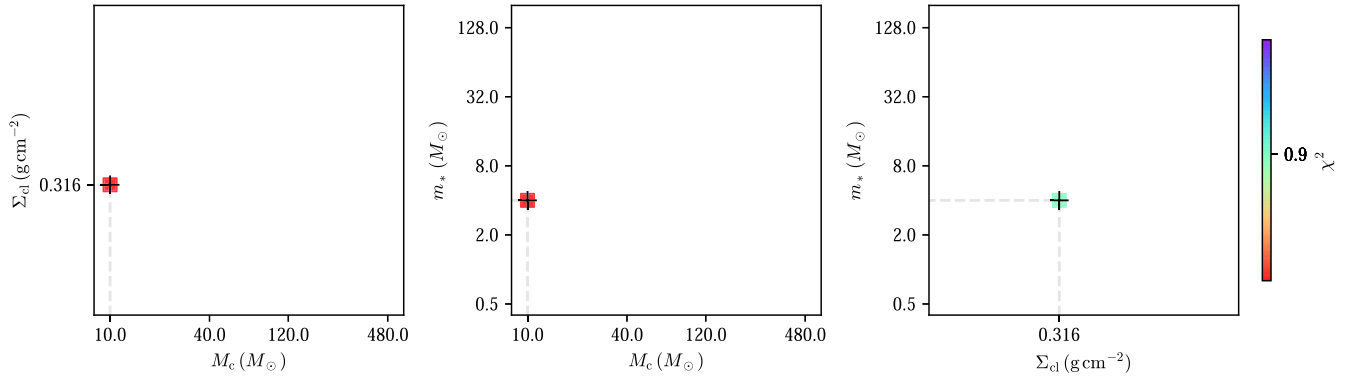






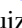










Figure A6. (Continued.)

ORCID iDs

Rubén Fedriani  <https://orcid.org/0000-0003-4040-4934>
 Jonathan C. Tan  <https://orcid.org/0000-0002-3389-9142>
 Zoie Telkamp  <https://orcid.org/0000-0001-6465-9590>
 Yichen Zhang  <https://orcid.org/0000-0001-7511-0034>
 Yao-Lun Yang  <https://orcid.org/0000-0001-8227-2816>
 Mengyao Liu  <https://orcid.org/0000-0001-6159-2394>
 James M. De Buizer  <https://orcid.org/0000-0001-7378-4430>
 Chi-Yan Law  <https://orcid.org/0000-0003-1964-970X>
 Maria T. Beltrán  <https://orcid.org/0000-0003-3315-5626>
 Viviana Rosero  <https://orcid.org/0000-0001-8596-1756>
 Kei E. I. Tanaka  <https://orcid.org/0000-0002-6907-0926>
 Giuliana Cosentino  <https://orcid.org/0000-0001-5551-9502>
 Prasanta Gorai  <https://orcid.org/0000-0003-1602-6849>
 Juan Farias  <https://orcid.org/0000-0002-5851-2602>
 Jan E. Staff  <https://orcid.org/0000-0001-9040-8525>

References

- Ai, M., Zhu, M., Xiao, L., & Su, H.-Q. 2013, *RAA*, **13**, 935
- Anderson, L. D., Bania, T. M., Balser, D. S., & Rood, R. T. 2012, *ApJ*, **754**, 62
- Astropy Collaboration, Price-Whelan, A. M., Sipőcz, B. M., et al. 2018, *AJ*, **156**, 123
- Astropy Collaboration, Robitaille, T. P., Tollerud, E. J., et al. 2013, *A&A*, **558**, A33
- Bally, J., & Lada, C. J. 1983, *ApJ*, **265**, 824
- Battersby, C., Ginsburg, A., Bally, J., et al. 2014, *ApJ*, **787**, 113
- Beaumont, C. N., & Williams, J. P. 2010, *ApJ*, **709**, 791
- Becker, R. H., White, R. L., Helfand, D. J., & Zoonematkermani, S. 1994, *ApJS*, **91**, 347
- Beltrán, M. T., Padovani, M., Girart, J. M., et al. 2019, *A&A*, **630**, A54
- Beuther, H., Mottram, J. C., Ahmadi, A., et al. 2018a, *A&A*, **617**, A100
- Beuther, H., Schilke, P., Sridharan, T. K., et al. 2002a, *A&A*, **383**, 892
- Beuther, H., Soler, J. D., Vlemmings, W., et al. 2018b, *A&A*, **614**, A64
- Beuther, H., Walsh, A., Schilke, P., et al. 2002b, *A&A*, **390**, 289
- Bonnell, I. A., Bate, M. R., & Zinnecker, H. 1998, *MNRAS*, **298**, 93
- Bradley, L., Sipőcz, B., Robitaille, T., et al. 2020, *astropy/photutils*: v1.0.0, v1.0.0, Zenodo, doi:10.5281/zenodo.4044744
- Brand, J., & Blitz, L. 1993, *A&A*, **275**, 67
- Butler, M. J., & Tan, J. C. 2012, *ApJ*, **754**, 5
- Caratti o Garatti, A., Stecklum, B., Garcia, R., et al. 2017, *NatPh*, **13**, 276
- Cesaroni, R., Beuther, H., Ahmadi, A., et al. 2019, *A&A*, **627**, A68
- Chen, Z., Sun, W., Chini, R., et al. 2021, *ApJ*, **922**, 90
- Churchwell, E., Povich, M. S., Allen, D., et al. 2006, *ApJ*, **649**, 759
- Clemens, D. P. 1985, *ApJ*, **295**, 422
- Clemens, D. P., & Barvainis, R. 1988, *ApJS*, **68**, 257
- Codella, C., & Bachiller, R. 1999, *A&A*, **350**, 659
- Costa Silva, A. R., Fedriani, R., Tan, J. C., et al. 2022, *A&A*, **659**, A23
- De Buizer, J. M., Liu, M., Tan, J. C., et al. 2017, *ApJ*, **843**, 33
- De Buizer, J. M., Radomski, J. T., Telesco, C. M., & Piña, R. K. 2005, *ApJS*, **156**, 179
- Deharveng, L., Schuller, F., Anderson, L. D., et al. 2010, *A&A*, **523**, A6
- Dent, W. R. F., Matthews, H. E., & Ward-Thompson, D. 1998, *MNRAS*, **301**, 1049
- Dewangan, L. K., Luna, A., Ojha, D. K., et al. 2015, *ApJ*, **811**, 79
- Fazio, G. G., Hora, J. L., Allen, L. E., et al. 2004, *ApJS*, **154**, 10
- Fedriani, R., Caratti o Garatti, A., Coffey, D., et al. 2018, *A&A*, **616**, A126
- Fedriani, R., Caratti o Garatti, A., Purser, S. J. D., et al. 2019, *NatCo*, **10**, 3630
- Fedriani, R., Caratti o Garatti, A., Koutoulaki, M., et al. 2020, *A&A*, **633**, A128
- Fish, V. L., Reid, M. J., Wilner, D. J., & Churchwell, E. 2003, *ApJ*, **587**, 701
- Fontani, F., Cesaroni, R., Testi, L., et al. 2004, *A&A*, **414**, 299
- Franco-Hernández, R., & Rodríguez, L. F. 2003, *RMxAA*, **39**, 107
- Fuente, A., Ceccarelli, C., Neri, R., et al. 2007, *A&A*, **468**, L37
- Garay, G., Rodríguez, L. F., Moran, J. M., & Churchwell, E. 1993, *ApJ*, **418**, 368
- Gieser, C., Semenov, D., Beuther, H., et al. 2019, *A&A*, **631**, A142
- Girart, J. M., Beltrán, M. T., Zhang, Q., Rao, R., & Estalella, R. 2009, *Sci*, **324**, 1408
- Giveon, U., Becker, R. H., Helfand, D. J., & White, R. L. 2005, *AJ*, **129**, 348
- Giveon, U., Becker, R. H., & White, R. L. 2008, *AJ*, **135**, 1697
- Griffin, M. J., Abergel, A., Abreu, A., et al. 2010, *A&A*, **518**, L3
- Grudić, M. Y., Guszejnov, D., Offner, S. S. R., et al. 2022, *MNRAS*, **512**, 216
- Gueth, F., Schilke, P., & McCaughrean, M. J. 2001, *A&A*, **375**, 1018
- Hasegawa, T. I., & Mitchell, G. F. 1995, *ApJ*, **451**, 225
- Herter, T. L., Adams, J. D., Gull, G. E., et al. 2018, *JAI*, **7**, 1840005
- Hill, T., Pinte, C., Minier, V., Burton, M. G., & Cunningham, M. R. 2009, *MNRAS*, **392**, 768
- Hoare, M. G., Purcell, C. R., Churchwell, E. B., et al. 2012, *PASP*, **124**, 939
- Hodapp, K.-W. 1994, *ApJS*, **94**, 615
- Hunter, T. R., Brogan, C. L., MacLeod, G., et al. 2017, *ApJL*, **837**, L29
- Indriolo, N., Neufeld, D. A., DeWitt, C. N., et al. 2015, *ApJL*, **802**, L14
- Johnston, K. G., Shepherd, D. S., Robitaille, T. P., & Wood, K. 2013, *A&A*, **551**, A43
- Krumholz, M. R., & McKee, C. F. 2008, *Natur*, **451**, 1082
- Kumar, M. S. N., Keto, E., & Clerkin, E. 2006, *A&A*, **449**, 1033
- Lada, C. J., Thronson, H. A. J., Smith, H. A., Schwartz, P. R., & Glaccum, W. 1984, *ApJ*, **286**, 302
- Launhardt, R., Evans, N. J. I., Wang, Y., et al. 1998, *ApJS*, **119**, 59
- Launhardt, R., & Henning, T. 1997, *A&A*, **326**, 329
- Launhardt, R., Ward-Thompson, D., & Henning, T. 1997, *MNRAS*, **288**, L45
- Law, C.-Y., Tan, J. C., Gorai, P., et al. 2022, *ApJ*, **939**, 120
- Lim, W., & De Buizer, J. M. 2019, *ApJ*, **873**, 51
- Liu, H. B., Chen, H.-R. V., Román-Zúñiga, C. G., et al. 2019a, *ApJ*, **871**, 185
- Liu, M., Tan, J. C., De Buizer, J. M., et al. 2019b, *ApJ*, **874**, 16
- Liu, H. B., Galván-Madrid, R., Jiménez-Serra, I., et al. 2015, *ApJ*, **804**, 37
- Liu, H. B., Jiménez-Serra, I., Ho, P. T. P., et al. 2012, *ApJ*, **756**, 10
- Liu, M., Tan, J. C., De Buizer, J. M., et al. 2020, *ApJ*, **904**, 75
- Liu, M., Tan, J. C., Marvil, J., et al. 2021, *ApJ*, **921**, 96
- López-Sepulcre, A., Cesaroni, R., & Walmsley, C. M. 2010, *A&A*, **517**, A66
- Lundquist, M. J., Kobulnicky, H. A., Alexander, M. J., Kerton, C. R., & Arvidsson, K. 2014, *ApJ*, **784**, 111
- McKee, C. F., & Tan, J. C. 2003, *ApJ*, **585**, 850
- Mège, P., Russeil, D., Zavagno, A., et al. 2021, *A&A*, **646**, A74
- Merrill, K. M., & Soifer, B. T. 1974, *ApJL*, **189**, L27
- Minh, Y. C., Liu, H. B., & Galván-Madrid, R. 2016, *ApJ*, **824**, 99
- Minh, Y. C., Liu, H. B., Galván-Madrid, R., et al. 2018, *ApJ*, **864**, 102
- Moellenbrock, G. A., Claussen, M. J., & Goss, W. M. 2009, *ApJ*, **694**, 192
- Molinari, S., Brand, J., Cesaroni, R., & Palla, F. 1996, *A&A*, **308**, 573
- Molinari, S., Brand, J., Cesaroni, R., Palla, F., & Palumbo, G. G. C. 1998a, *A&A*, **336**, 339
- Molinari, S., Faustini, F., Testi, L., et al. 2008a, *A&A*, **487**, 1119
- Molinari, S., Pezzuto, S., Cesaroni, R., et al. 2008b, *A&A*, **481**, 345
- Molinari, S., Testi, L., Brand, J., Cesaroni, R., & Palla, F. 1998b, *ApJL*, **505**, L39
- Molinari, S., Testi, L., Rodríguez, L. F., & Zhang, Q. 2002, *ApJ*, **570**, 758
- Moser, E., Liu, M., Tan, J. C., et al. 2020, *ApJ*, **897**, 136
- Neugebauer, G., Habing, H. J., van Duinen, R., et al. 1984, *ApJL*, **278**, L1
- Olguin, F. A., Hoare, M. G., Johnston, K. G., et al. 2020, *MNRAS*, **498**, 4721
- Pestalozzi, M. R., Minier, V., & Booth, R. S. 2005, *A&A*, **432**, 737
- Pillai, T., Kauffmann, J., Tan, J. C., et al. 2015, *ApJ*, **799**, 74
- Poetzel, R., Mundt, R., & Ray, T. P. 1992, *A&A*, **262**, 229
- Preibisch, T., Balega, Y. Y., Schertl, D., & Weigelt, G. 2003, *A&A*, **412**, 735
- Purcell, C. R., Balasubramanyam, R., Burton, M. G., et al. 2006, *MNRAS*, **367**, 553
- Rieke, G. H., Harper, D. A., Low, F. J., & Armstrong, K. R. 1973, *ApJL*, **183**, L67
- Rosero, V., Hofner, P., Claussen, M., et al. 2016, *ApJS*, **227**, 25
- Rosero, V., Tanaka, K. E. I., Tan, J. C., et al. 2019a, *ApJ*, **873**, 20
- Rosero, V., Hofner, P., Kurtz, S., et al. 2019b, *ApJ*, **880**, 99
- Rygl, K. L. J., Brunthaler, A., Sanna, A., et al. 2012, *A&A*, **539**, A79
- Sakai, N., Sato, M., Motogi, K., et al. 2014, *PASJ*, **66**, 3
- Sánchez-Monge, Á. 2011, PhD thesis, Univ. of Barcelona
- Sánchez-Monge, Á., Pandian, J. D., & Kurtz, S. 2011, *ApJL*, **739**, L9
- Simon, M., Righini-Cohen, G., Felli, M., & Fischer, J. 1981, *ApJ*, **245**, 552
- Simpson, J. P., Whitney, B. A., Hines, D. C., et al. 2013, *MNRAS*, **435**, 3419
- Solomon, P. M., Rivolo, A. R., Barrett, J., & Yahil, A. 1987, *ApJ*, **319**, 730
- Sridharan, T. K., Beuther, H., Schilke, P., Menten, K. M., & Wyrowski, F. 2002, *ApJ*, **566**, 931
- Stecklum, B., Wolf, V., Linz, H., et al. 2021, *A&A*, **646**, A161
- Tanaka, K. E. I., Tan, J. C., & Zhang, Y. 2017, *ApJ*, **835**, 32
- Taniguchi, K., Tanaka, K. E. I., Zhang, Y., et al. 2022, *ApJ*, **931**, 99
- Townner, A. P. M., Brogan, C. L., Hunter, T. R., Cyganowski, C. J., & Friesen, R. K. 2019, *ApJ*, **875**, 135
- Trinidad, M. A., Curiel, S., Cantó, J., et al. 2003, *ApJ*, **589**, 386
- Urquhart, J. S., König, C., Giannetti, A., et al. 2018, *MNRAS*, **473**, 1059

- van der Tak, F. F. S., Walmsley, C. M., Herpin, F., & Ceccarelli, C. 2006, *A&A*, **447**, 1011
- Wang, P., Li, Z.-Y., Abel, T., & Nakamura, F. 2010, *ApJ*, **709**, 27
- Watt, S., & Mundy, L. G. 1999, *ApJS*, **125**, 143
- Werner, M. W., Roellig, T. L., Low, F. J., et al. 2004, *ApJS*, **154**, 1
- White, R. L., Becker, R. H., & Helfand, D. J. 2005, *AJ*, **130**, 586
- Wolf-Chase, G., Arvidsson, K., & Smutko, M. 2017, *ApJ*, **844**, 38
- Wolf-Chase, G., Smutko, M., Sherman, R., Harper, D. A., & Medford, M. 2012, *ApJ*, **745**, 116
- Wouterloot, J. G. A., Brand, J., & Fiegle, K. 1993, *A&AS*, **98**, 589
- Wynn-Williams, C. G., Becklin, E. E., Forster, J. R., et al. 1977, *ApJL*, **211**, L89
- Yun, J. L., & Clemens, D. P. 1994, *ApJS*, **92**, 145
- Yun, J. L., & Clemens, D. P. 1995, *AJ*, **109**, 742
- Zhang, Q., Hunter, T. R., Brand, J., et al. 2005, *ApJ*, **625**, 864
- Zhang, Q., Qiu, K., Girart, J. M., et al. 2014a, *ApJ*, **792**, 116
- Zhang, Y., Tan, J. C., & Hosokawa, T. 2014b, *ApJ*, **788**, 166
- Zhang, Y. 2018, yczhang04/sedfit: sedfit, v1.0.1, Zenodo, doi:10.5281/zenodo.1134877
- Zhang, Y., & Tan, J. C. 2011, *ApJ*, **733**, 55
- Zhang, Y., & Tan, J. C. 2018, *ApJ*, **853**, 18
- Zhang, Y., Tan, J. C., & McKee, C. F. 2013a, *ApJ*, **766**, 86
- Zhang, Y., Tan, J. C., De Buizer, J. M., et al. 2013b, *ApJ*, **767**, 58
- Zhu, M., Davis, C. J., Wu, Y., et al. 2011, *ApJ*, **739**, 53